Title

Focused Helium Ion Beam Fabricated Superconducting Devices from Y Ba2Cu3O7−δ and Niobium Films

Author

Forman, Joseph A

Publication Date

2024

UNIVERSITY OF CALIFORNIA
RIVERSIDE

Focused Helium Ion Beam Fabricated Superconducting Devices from $YBa_2Cu_3O_{7-\delta}$ and Niobium Films

A Dissertation submitted in partial satisfaction
of the requirements for the degree of

Doctor of Philosophy

in

Materials Science and Engineering

by

Joseph Aaron Forman

March 2024

Dissertation Committee:

Professor Shane Cybart, Chairperson
Professor Alex Greaney
Professor Ran Cheng

The Dissertation of Joseph Aaron Forman is approved:

Committee Chairperson

University of California, Riverside

Acknowledgments

First and foremost I am grateful to my advisor Professor Shane Cybart who taught me much of what I know about superconducting device physics. Thank you for you guidance and advice in my experiments and for always being there to help me when I was stuck or did not know the right direction to take. Also I am grateful for our many spirited political conversations and the delicious libations from Scotland you have gifted me over the years.

I would not have been able to write this thesis and carry out my experiments without the tutelage of the students that came before me in the ONELab research group. I want to thank Dr. Han Cai for teaching me so many of the details of experimentation, fabrication, electrical characterization and most importantly patience. Without your guiding and teaching I would not have been able to carry on my experiments after you graduated. Thank you Dr. Jay Lefebvre and Dr. Yan-Ting Wang for the many enlightening conversations about superconductivity and many other areas of physics and for guiding me in the early years of my research.

Thank you Alec Brooks, Sreekar Vattipalli, Dr.Nirjhar Sarkar and Adhilsha Parachikunnumal for the time we spent together fixing equipment and runny countless electrical characterizations together. Special thanks to Alec for keeping me motivated to work on myself in and out of the lab.

Thank you Werner Baer for the countless hours you spent helping me to fix a d trouble shoot our helium ion microscope over the phone and in person.

Lastly, thank you to all the friends and family that provided me with encouragement and support over the last 4.5 years.

To my parents for all the love and support.

ABSTRACT OF THE DISSERTATION

Focused Helium Ion Beam Fabricated Superconducting Devices from $YBa_2Cu_3O_{7-\delta}$ and Niobium Films

by

Joseph Aaron Forman

Doctor of Philosophy, Graduate Program in Materials Science and Engineering
University of California, Riverside, March 2024
Professor Shane Cybart, Chairperson

In this thesis I describe the design and characteristics of a variety of superconducting devices fabricated using focused Helium ion beam. Early chapters are dedicated to summarizing the mechanics of superconductors and discussing the theoretical operating principles underlying Josephson junctions and superconducting quantum interference devices (SQUIDs). In this thesis the superconducting devices are made using $YBa_2Cu_3O_{7-\delta}$ (YBCO) and Niobium films.

Using a Helium ion microscope, I am able to modify the electronic structure of the superconducting material by directly writing induced disordered regions that define the structure and geometry of the devices. By carefully choosing the dose of ion irradiation I can accurately set the operating characteristic, critical current and normal state resistance, of the Josephson junctions as well as creating highly insulating regions allowing me to define device geometries at the nanometer scale.

Experiments using YBCO films outline the types of Josephson junctions I can make with this fabrication technique. YBCO Junctions are characterized over a wide range

of temperature. I characterize the critical current response in the presence of a magnetic field and demonstrate the AC Josephson effect through the emergence of Shapiro steps in the IV curve. Much of my work on YBCO is dedicated to the design and characterization of highly sensitive SQUID magnetometers. I successfully integrated the SQUID magnetometer on a commercial pulsed tube cooler equipped with a peizo-controlled stage probe head for magnetic materials analysis. This system has an operating temperature range between 1-50K. A similar lower noise iteration of this design was found to have a field noise of $540fT/\sqrt{Hz}$ and a flux noise of $2\mu\Phi_0/\sqrt{Hz}$ at 1Khz making it the lowest noise YBCO SQUID smaller than $500\mu m$ ever made.

I fabricated and characterized the first Josephson junctions on niobium films made with focused Helium ion beam. This technique can mill the Niobium with resolution as small as 40nm. Junction fabrication is analyzed at a wide range of doses, and I found Josephson effects in devices radiated from 50,000 to 15,000,000 ions/nm. Junctions were characterized at a wide range of temperatures showing the onset of hysteresis to the IV curve as temperature decreases. I also performed characterizations of the junctions in magnetic field and showed the formation of Shapiro steps to the IV curve when junctions are in the presence of microwave radiation. I fabricated arrays of Josephson junctions on niobium film and analyzed the optimal spacing for junctions in the arrays. I demonstrated the operation of arrays with up to 100 junctions in series and showed giant flat Shapiro steps at voltages of up to 1.32mV. I showed how these junction arrays can be scaled up and integrated in Josephson arbitrary waveform synthesizer or DC voltage standard devices. Lastly, I fabricated and characterized the first niobium SQUID made with focused helium ion beam induced disorder junctions.

Contents

List of Figures

Chapter 1

Introduction

The progress of the arts, science, and engineering is often discussed as series of as deep insights made by a select few however, this is seldom the whole truth. Collaboration and deep understanding of the layers of concepts that modern research stand on is integral in pushing the edges of any field of study. It is only through careful consideration of the fundamentals that a path can been seen while patience and practice can be the strongest tools to reach new heights. The father of modern science Isaac Newton expressed this sentiment aptly when he said "If I have seen further, it is by standing on the shoulders of giants". In this thesis I will discuss some of the projects I worked on to help advance the fabrication and capabilities of high transition temperature superconducting devices made from YBCO and Niobium.

Superconductors are materials that experience a phase change, a reordering of the electronic structure, that results in the Meissner effect and that demonstrate zero resistance to electrical conduction [1][2][3]. The phenomenon of superconductivity was first observed in the early 1910s for which H.K. Onnes was awarded a Nobel prize. Quantum theory is the most accurate and precise theory of the natural world and gives us a framework that enables the understanding of how atoms and molecules are constructed and interact. It also can be used to predict the properties of ordered solids [4]. Using only first principles, knowing placement and kind of atoms in a solid, quantum theory lets us predict the possible energy and momentum states of electrons and phonons. It took 60 years from the first observations of superconductivity for a coherent theory based solely on a first principles approach to be written down using the math and framework of quantum mechanics. This microscopic description of superconductivity is called BCS theory for its authors Bardeen, Cooper and Schrieffer who received the Nobel prize in in 1972 for its derivation [5]. Superconducting materials have garnered much excitement in the physics community over the last century for their expression of quantum phenomenon on a macro scale. These materials have changed our modern world and spurred a wide array of technologies with many applications garnered by their ability to generate large currents and magnetic fields [6]. Such devices that are used to make large magnetic fields are called passive devices. Conversely, the first active superconducting device theorized and fabricated is the Josephson Junction. Brian Josephson theorized and built this device and was subsequently awarded a Nobel prize in 1973 [7]. Much of the work in this thesis pertains to the construction and analysis of Josephson junction based devices.

Many elemental materials exhibit superconductivity. In this thesis I describe the fabrication of Niobium based devices which exhibit a transition to the superconducting state at 9.2 Kelvin [8]. A large portion of my work was done using the material denoted

YBCO. YBCO has a very complex crystal structure and is in a class of materials called perovskite cuprate superconductors. YBCO has its superconducting phase transition at 92 Kelvin, well above the temperature that liquid nitrogen boils [8]. The production of and devices fabricated with YBCO have seen many advances since its initial formulation in 1986 by Bednorz and Muller who were awarded a Nobel prize for its synthesis [9]. There are three main methods used to fabricate Josephson junctions: lithography, step edge and grain boundary. However, in recent years a technique of using a focused Helium ion beam to create Josephson junctions was established by Cybart et al. 2015 [10]. This is the method I used to create some novel superconducting devices.

The early chapters of this thesis will briefly describe the principles of superconductors and basic superconducting devices, Josephson junctions and superconducting quantum interference devices. I will next discuss my fabrication of such devices. Starting with our methods of lithography and giving detail to the use of focused ion beam technology in our nanoscale fabrication and junction development. I will also discuss the materials used in these devices, their attributes and why they were chosen. The later chapters will describe in detail the design of the devices I made as well as their characterizations. I will show their operating capabilities, what can be learned from them and the novelty they pose to this field.

Chapter 2

Theory of Superconductors

A material is in its superconducting state when it allows the flow of charge with no voltage as well as exhibiting the Meissner effect, where all magnetic fields are expelled and the material acts as a perfect diamagnet [12]. Experimentally this can be seen as a sharp inflection point in magnetic susceptibility, or heat capacity, and a drop to zero resistance. Both of these phenomena will occur at the same temperature: the transition temperature, T_C [8].

2.1 Superconducting Characteristics: λ, ζ, θ

There are two early phenomenological theories of superconductivity known as Ginzburg-Landau theory and London's theory. The London theory implements Maxwell's equations with the assertion of zero B field inside a superconductor and that charge can flow freely. An important finding from the London theory is a characteristic length intrinsic to each superconducting material known as the penetration depth, λ [11][12]. .

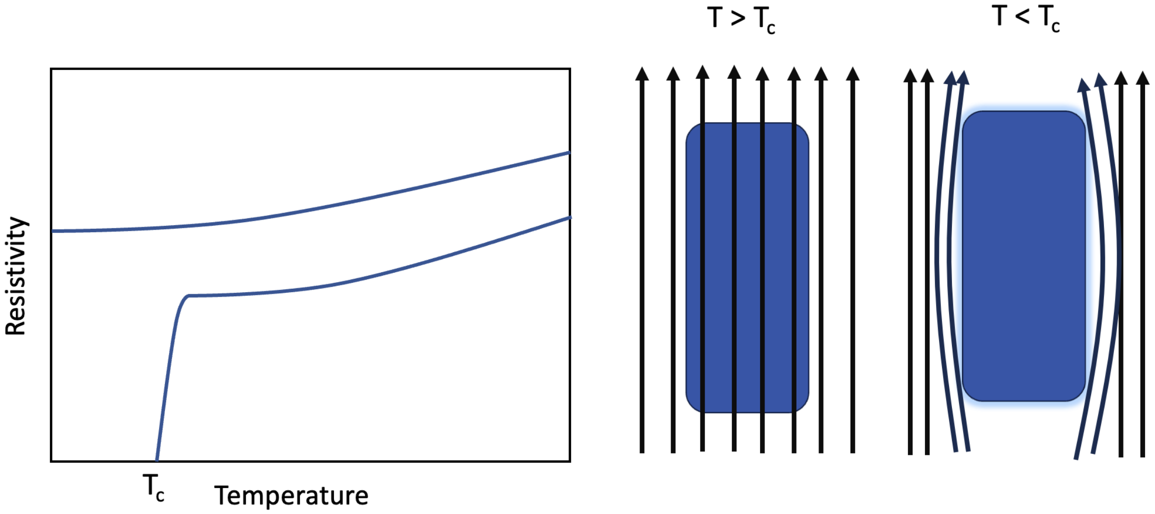

Figure 2.1: Characteristic drop in Resistance (left) and Meisner effect: induced diamagnetism (Right).

$$\lambda = (\frac{m}{\mu_0 n_s e^2})^{1/2} \tag{2.1}$$

In this equation m is the effective mass of the charge carriers and n_s is the charge carrier density. The london penetration gives the length at which a magnetic field can penetrate a superconductor.

Ginzburg-Landau theory presents the notion of a superconducting order parameter in its wave function, the phase θ , which varies in space[13].

$$\psi(r) = n_s \psi(r) e^{i\theta(r)} \tag{2.2}$$

Ginzburg-Landau theory derived another important characteristic intrinsic to each superconducting material: the coherence length ζ [34].

$$\zeta = \frac{2\hbar v_f}{\pi \Delta} \tag{2.3}$$

In this equation v_f is the fermi velocity and delta is the superconducting energy gap. The coherence length is related to the length between electrons in a cooper pair.

Superconducting materials are often put into two classes: type I and type II. For type I superconductors $\zeta > \lambda$, and for type II superconductors $\zeta < \lambda$. All 'high' temperature superconducting materials are type II [8].

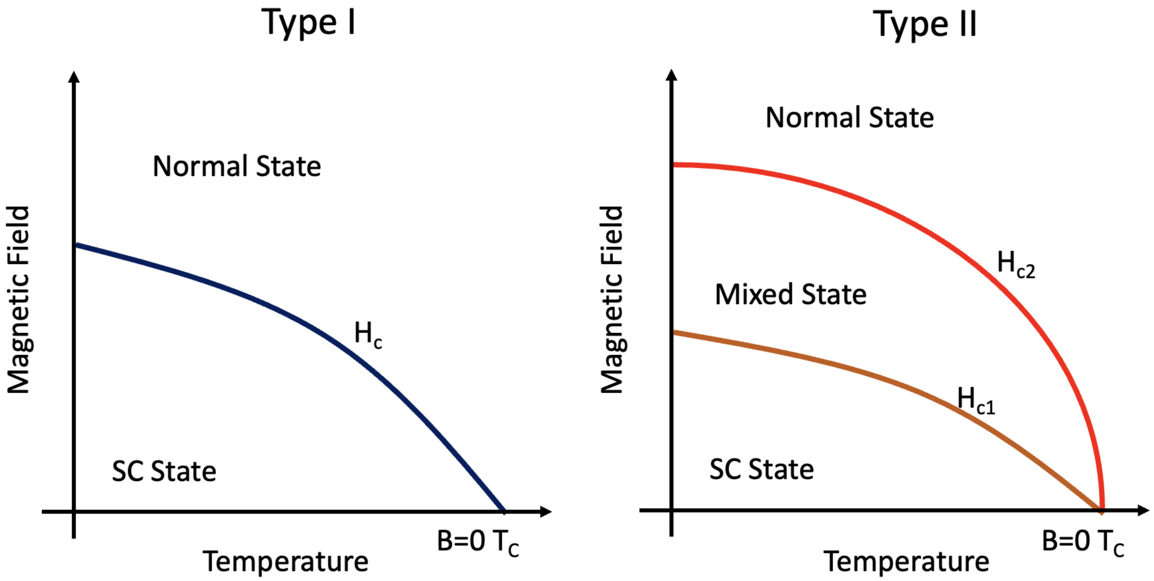

Figure 2.2: Type I vs Type II superconducting materials.

In the presence of a large enough magnetic field the superconducting state will break down, unbinding the cooper pairs in both type I and type II. The main practical difference between type I and type II superconductors is that type II materials, in the presence of a sufficiently high magnetic field, will form normal state regions where the magnetic field lines pass through along side superconducting regions. These normal state regions are called vortexes. The penetrating magnetic field generate a circulating shielding current surrounding them. [14].

2.2 Microscopic Theory

Superconductivity is the result of an electron - phonon interaction resulting in a weak attractive force between electrons allowing the formation of 'bound' pairs of electrons. Paired electrons are called cooper pairs for the scientist who theorized them. Each cooper pair has a charge of 2e. Only electrons from opposite points on the Fermi surface can form cooper pairs. This quantum theory of superconductivity is called BCS theory[5].

Electrons are fermions and thus have half integer spin. When two electrons form a cooper pair, their spins will add to a whole integer either $S = 0$ singlet state or $S = 1$ triplet state. This whole integer spin means that the cooper pair no longer obeys the Pauli exclusion principle and can be thought of as a Boson. The cooper pairs in superconducting materials act as a Bose-Einstein condensate. The way a cooper pair moves through the crystal lattice and its ability to occupy degenerate electronic states enables the perfect conductivity observed in superconductors [5][15].

As electrons form cooper pairs, they fall in energy to the fermi energy opening up a energy gap between the superconducting electrons and the lowest level quasi particle excitation.

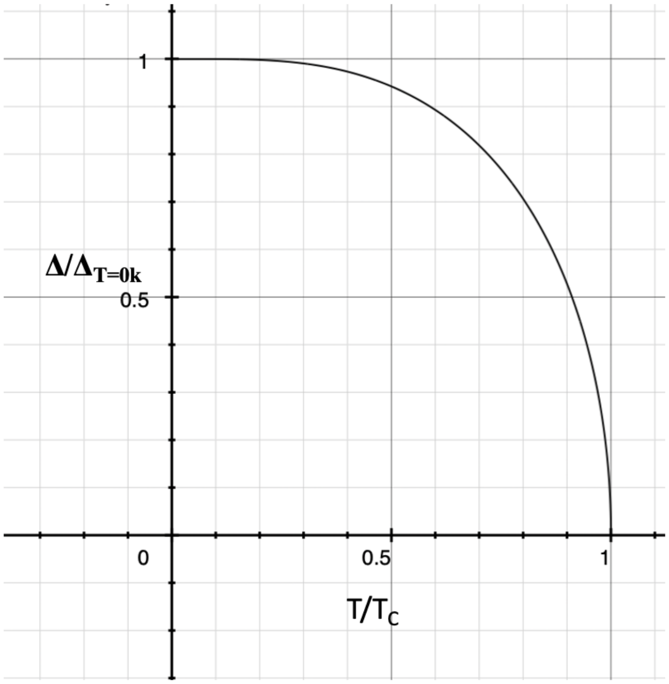

Figure 2.3: Superconducting energy gap vs Temperature

One prediction of BCS theory is the way the superconducting gap opens as temperature falls below T_C.

$$\Delta(T) \approx 1.76 K_B T_C tanh(1.74(\frac{T_C}{T} - 1)^{1/2}) \tag{2.4}$$

This equation is graphed in figure 2.3. One important thing to note from this graph is the rate at which the gap opens. We see at half of T_C the gap is nearly 90 percent open. The gap opens with the number or percent of charge carriers that have formed cooper pairs. This means that near T_C very few of the cooper pairs have formed and the superconducting state can be easily broken[14].

A material in the superconducting state can go back to its normal state if enough energy is put into the cooper pairs causing them to break. This energy can be in the form of heat but it can also be in the form of magnetic field or current density. There is a critical magnetic field usual denoted as H_C, as well as a critical current density J_C, at which the superconducting state will be broken.

Chapter 3

Josephson Junction

3.1 Introduction to Josephson Junctions

The Josephson junction is the key and most basic element in all active superconducting devices. A wide range of technologies have been developed utilizing their unique properties. Josephson junctions underpin the development of many magnetic sensing systems[16]. They are the basic component to the most sensitive magnetic sensor developed: the superconducting quantum interference device[17][18]. Magnetoencephalography and Magnetocardiography utilize arrays of Josephson junction based magnetic sensors to measure brain and heart activity respectively[19][20][21]. Magnetic imaging systems have been developed based on Josephson devices[22][23]. The burgeoning field of superconducting digital circuits relies on the qualities of Josephson junctions, providing the possibility of adiabatic reversible computing[24][25]. Josephson junctions are in their core quantum devices and their Hamiltonian produce a nonlinear energy potential allowing for the development of the artificial atoms used in many quantum computers [28]. Josephson junctions can couple to gigahertz radiation producing quantized vertical steps in their IV curve which enable them to be used as arbitrary waveform generators and in devices that standardize the Volt[26]. The many uses of Josephson junctions show the intrinsic connection they have in the presence of magnetic fields, in Giga-hertz radiation and how they are true macro scale quantum devices. To understand how Josephson junctions can have so many applications it is necessary to understand a derivation for the equations that govern them.

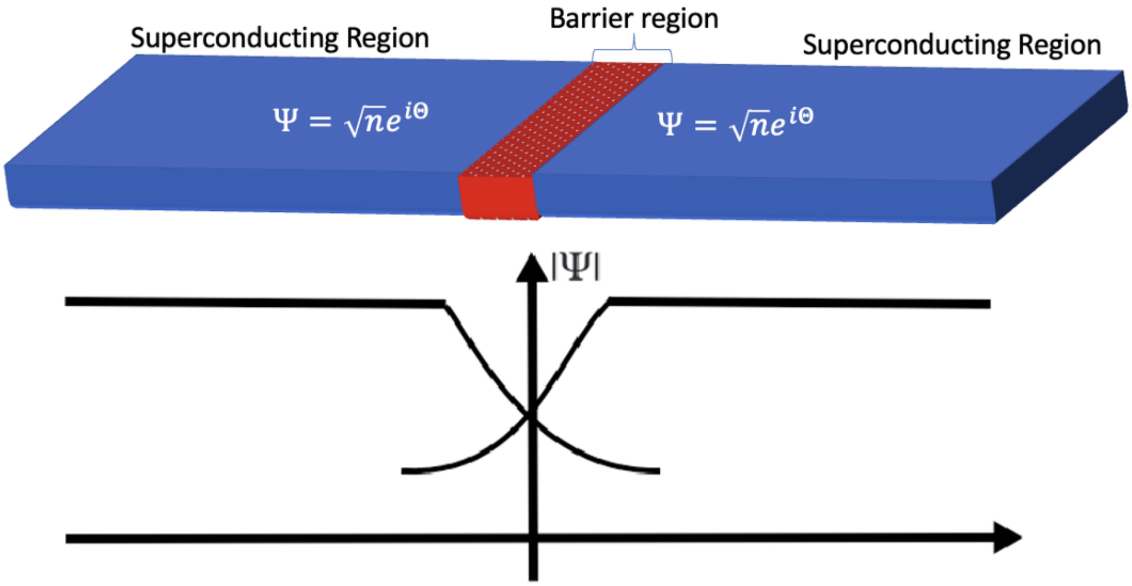

Figure 3.1: Josephson junction: superconducting regions separated by barrier region. The wave function on either side of the barrier decays and couples with the wave function on the the opposite side.

3.2 The First and Second Josephson Equations

The current passing through a Josephson junction is the result of the tunneling of cooper pairs from one region of superconducting material through an insulating region into another superconducting region. In the previous section it was shown that a region of superconducting material, can be described under one wave function: $\psi = \sqrt{n}e^{i\theta}$. Where $\sqrt{n}$ is the number of cooper pairs and θ is the order parameter unique to that region often refereed to as the phase. I will use Ψ_1 to represent the wave function to the left of the barrier and Ψ_2 to represent the wave function to the right of the barrier while θ_1 and θ_2 will do the same for the order parameter. These wave functions are governed by the follow Schrodinger relations:

$$i\hbar\frac{\partial\Psi_1}{\partial t} = U_1\Psi_1 + K\Psi_2 \tag{3.1}$$

$$i\hbar\frac{\partial\Psi_2}{\partial t} = U_2\Psi_2 + K\Psi_1 \tag{3.2}$$

Here U is the potential energy and K is the coupling constant between the two superconducting regions set by the width and height of the barrier. I substitute for Ψ_1 and Ψ_2 to get the form:

$$i\hbar\frac{\partial\Psi_1}{\partial t} = \left(\frac{-i\partial n}{2n\partial t} - \frac{\partial\Psi_1}{\partial t}\right)\sqrt{n}e^{i\theta_1} = U_1\Psi_1 e^{i\theta_1} + K\sqrt{n}\Psi_2 \tag{3.3}$$

$$i\hbar\frac{\partial\Psi_2}{\partial t} = \left(\frac{-i\partial n}{2n\partial t} - \frac{\partial\Psi_2}{\partial t}\right)\sqrt{n}e^{i\theta_1} = U_1\Psi_2 e^{i\theta_1} + K\sqrt{n}\Psi_1 \tag{3.4}$$

Taking only the real part of these equations, assuming zero applied voltage and simplifying we are left with:

$$\frac{\partial n}{\partial t} = (2Kn/\hbar)sin(\theta_1 - \theta_2) \tag{3.5}$$

It is important to see here that the flow of charge will be only a function of the difference in phase on either side of the barrier and no bias voltage is needed to create a current. I will now write the phase difference between superconducting regions, θ_1 - θ_2 as ϕ. The term (2Kn/$\hbar$) is known to be the maximum super current in this zero voltage state which I will write as I_c. Taking these substitutions I can write the first Josephson equation in the simplified form:

$$I = I_c sin(\phi) \tag{3.6}$$

This equation describes the current across a Josephson junction as a function of phase. Above I assumed there is zero potential difference across this device. Now taking the case where there is an applied voltage and accounting for the imaginary parts of the differential equation we can obtain the following:

$$\frac{\partial \Theta_1}{\partial t} = \frac{K}{\hbar}(\frac{n_2}{n_1})^{1/2}cos(\phi) + \frac{e(U_1 - U_2)}{2\hbar} \tag{3.7}$$

$$\frac{\partial \Theta_2}{\partial t} = \frac{K}{\hbar}(\frac{n_1}{n_2})^{1/2}cos(\phi) + \frac{e(U_2 - U_1)}{2\hbar} \tag{3.8}$$

After subtracting these two equations from one another we obtain the second Josephson equation:

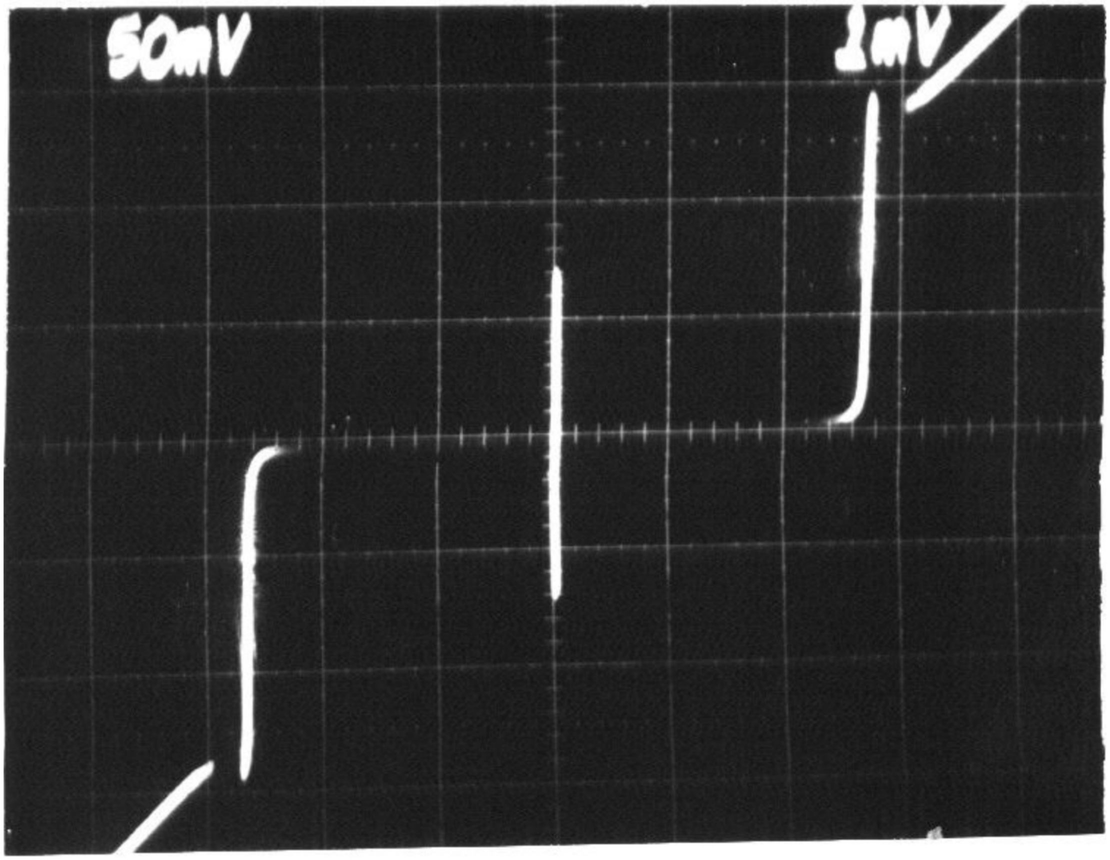

Figure 3.2: IV of a typical Josephson junction. In this figure, the Voltage is on the x axis and current is on the Y axis. This measurement is on a Nb - Al Oxide - Al - Nb hetero structure Josephson junction.

$$\frac{d\phi}{dt} = \frac{2eV}{\hbar} \tag{3.9}$$

An applied DC bias across the junction will produce a change to the phase difference evolving with time. This is the second Josephson equation.

I want to point out a few things in the IV curve above. Firstly the central line in the figure demonstrates a current with zero voltage. The peak of this central line is called the critical current, I_C. In this figure there is a discontinuity between the central line and the next vertical line to the right and the left. This is because the superconducting material used is niobium which has a superconducting gap. The slanted lines to the edges of the image show the material is now past the superconducting gap and there is enough voltage for normal state electrons to pass through the barrier. The slope of this line is called the normal state resistance, R_N.

3.2.1 Magnetic Field Effects

Let's consider a Josephson junction in the presence of a magnetic field perpendicular to the direction current flows. In this case, current travels in the X direction and the width of the Junction is along the Y while the height is along the Z. A magnetic field impingent upon the z axis of a Josephson junction will cause an oscillation in the phase of the material in the x direction. The phase oscillation has a period of to $2\pi n/\Phi_0$, where Φ_0 is the magnetic flux quanta: $\Phi_0 = 2.07 \times 10^{-15}$Wb [30]. The magnetic flux impingent upon a Josephson junction is equal to the magnitude of the magnetic field multiplied by the area of the junction in the x-y plane. For reference, one militesla through an area of approximately 2000 nm will equate to approximately one magnetic flux quanta.

Superconductors are perfectly diamagnetic[31]. This results in the field seeing the junction as a narrow slit while field lines that hit the superconductor nearby by take the shortest path around the superconductor or through the junction [29]. The magnetic field creates standing waves of current density inside the junction porportional to multiples of the magnetic flux quanta. This results in an oscillation to the maximum critical current of the junction with field. This relation is described mathematically in the equation bellow [27][33].

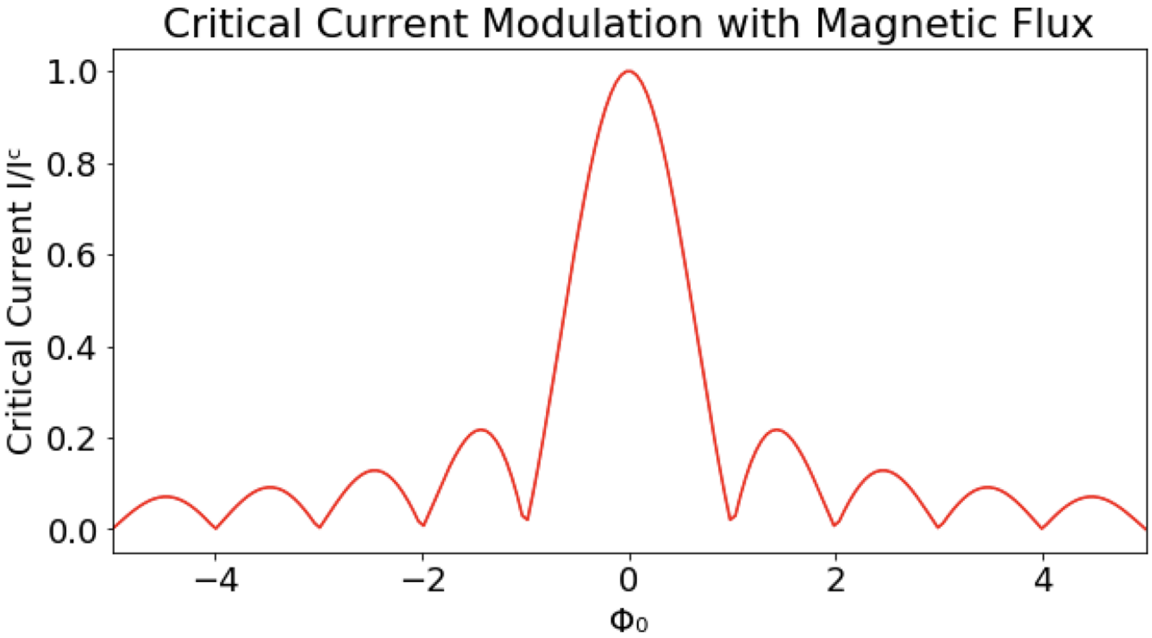

Figure 3.3: Fraunhofer pattern for a Josephson junction.

$$I_C(B) = \left| \frac{sin(\frac{\pi \Phi_B}{\Phi_0})}{\frac{\pi \Phi_B}{\Phi_0}} \right| \tag{3.10}$$

$$I_C(B) = \left| sin(\frac{\pi \Phi_B}{\Phi_0}) \right| \tag{3.11}$$

This relation is often called the Josephson fraunhoffer equation as it is physically and graphically analogous to Young's single slit diffraction pattern in optics.

3.2.2 AC Effects

Earlier I showed how a DC bias will produce a time oscillation to the phase difference across the junction. The changing phase difference across the junction produces an

AC current. Now I want to look at the case of a Josephson junction under both a DC and AC bias.

The coupling between the frequency generated by an applied voltage according to the second Josephson equation and an applied AC bias frequency will create a resonance at specific voltages. This results in steps of constant voltage on the IV curve, at quantized intervals, falling at specific voltages. The constant voltage regions occur at positions follow the formula: [35]:

$$V = \frac{nh\omega}{2e} \tag{3.12}$$

ω is the frequency of the AC bias and n $= \pm1, \pm2, \pm3...$

To analyze this situation quantitatively lets start with a equation for voltage with applied AC and DC bias:

$$V = V_0 + V_1 cos(\omega t) \tag{3.13}$$

Substituting this into the second Josephson equation and integrating we see the floowing:

$$\phi = \int \frac{2eV}{\hbar} dt = \frac{2e}{\hbar} \int V_0 + V_1 cos(\omega t) dt \tag{3.14}$$

$$= \phi_0 + \frac{2e}{\hbar} V_0 t + \frac{2e}{\hbar\omega} V_1 sin(\omega t) \tag{3.15}$$

Now I insert this equation for the phase difference with DC and AC bias into the first Josephson equation to consider this system in terms of a current relation:

$$I = I_c sin(\phi_0 + \frac{2e}{\hbar}V_0 t + \frac{2e}{\hbar\omega}V_1 sin(\omega t)) \tag{3.16}$$

If we expand this using a Bessel function of the first kind while adding a shunting current V/R to to account for quasi particle current we can get the form:

$$I = I_c \sum_{K=-\infty}^{\infty} (-1)^K J_K(\frac{2eV}{\hbar\omega}) sin(\phi_0 + \frac{2e}{\hbar}V_0 t + \frac{2e}{\hbar\omega}V_1 sin(\omega t)) + V/R \tag{3.17}$$

The current will go by the final term V/R unless $V = \frac{nh\omega}{2e}$. At these voltages the IV will have a 'vertical' super current that is dependent on the applied power of the AC bias.

This phenomenon was first observed by Sydney Shapiro in 1963 and the characteristic regions of the IV are called Shapiro steps for his discovery[32]. It is important to note that the location of the steps in these equations is only dependent on the applied frequency and some universal constants. This coupling of the junction to an applied AC bias enables Josephson junctions to be perfect frequency to voltage transducers.

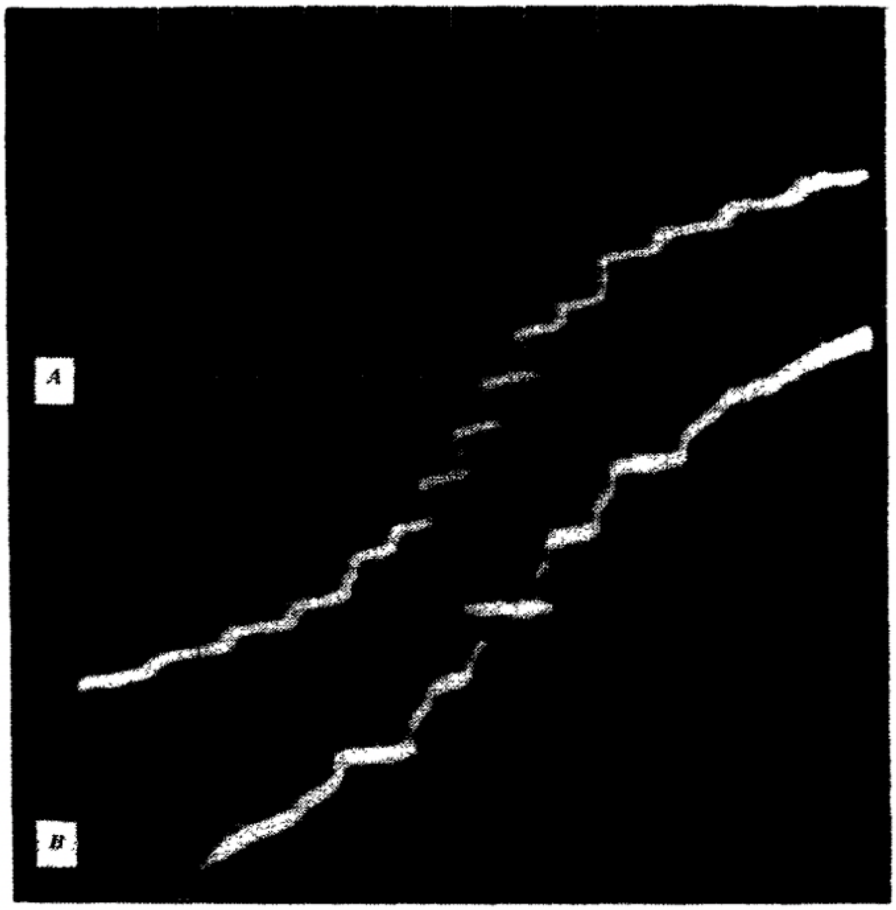

Figure 3.4: Shapiro 'Steps' in the V-I curve at characteristic voltages. In this graph, current is along the X axis and voltage is along the Y axis.

Chapter 4

Superconducting Quantum Interference Device Theory (SQUIDs)

Superconducting Quantum Interference Devices (SQUIDs) are the most sensitive magnetic field sensors and have many commercial and research based applications [36]. A SQUID consists of a loop of superconducting material interrupted by two Josephson junctions in parallel [8][37]. The critical current of a SQUID is the sum of the critical current of each junction $I_{C_{squid}} = I_{Cj1} + I_{Cj2}$. The R_N, normal state resistance of this device can be calculated with the equation: $\frac{1}{R_N} = \frac{1}{R_{j1}} + \frac{1}{R_{j2}}$, where R_{j1} and R_{j2} are normal state resistance of each junction. It is important to remember some facts about superconductors and magnetic fields when analyzing SQUIDs. First, superconductors are perfectly diamagnetic and will repel all external magnetic flux. Next is that Magnetic flux

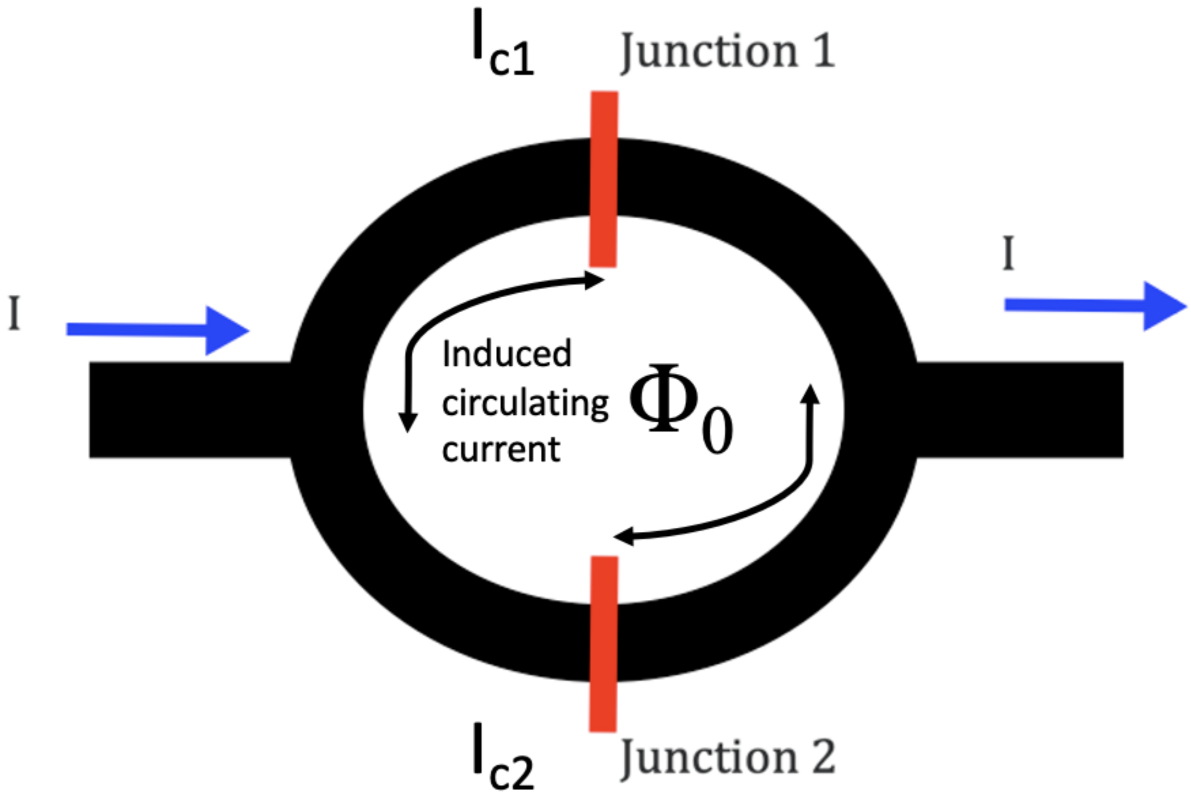

Figure 4.1: Drawing of a Superconducting Quantum Interference Device.

is quantized: any magnetic flux through a superconducting loop can only enter the loop in multiples of the magnetic flux quantum, Φ_0. Magnetic flux that enters the superconducting loop will drive a circulating surface current that balances the energy of the magnetic field. Lastly, the superconducting phase is unique at specific points and returns back to its value by multiples of 2πn around a loop of material[39].

Let's assume that both junctions have the same critical current and normal state resistance. If we drive this system with a current near its I_C each junction will also be driven near their critical current. In the presence of a magnetic field a circulating current will increase the current density through one of the junctions while decreasing total current density through the other. As field increases the circulating current will increase and push one junction past its I_C. That junction will slip into its normal state and the loop will accept a magnetic flux quanta. To balance the energy of the external field vus flux trapped in the loop, the direction of the circulating current will flip. This flip of induced circulating current direction will now drive the current density of the opposite junction up while lowering the current density of the former. This results in a system of oscillating current, and voltage, with applied field. This oscillation is periodic with the magnetic flux quantum[17].

In an earlier section we saw how a single junction produced a diffraction pattern of its critical current amplitude, in the presence of a magnetic field, similar to Young's single slit diffraction of light amplitudes. In this case of two junctions there is an interference of phase, across each junction, caused by the magnetic field induced circulating current. This phase interference is seen in a interference pattern of the critical current vs applied magnetic field, similar to Young's double slit pattern. This interference pattern can also be seen when we graph voltage vs magnetic field.

SQUIDs are inherently sensitive to magnetic fields. However, designing a SQUID with low enough intrinsic noise to signal ratio can be challenging as there are many variables that effect its noise level and sensitivity.

To measure the noise spectral density, or use a SQUID for magnetic sensing you must fist put it in its 'active' state by biasing the device at or slightly above I_C. As mentioned earlier an applied magnetic field will generate a voltage response making SQUIDs magnetic field to voltage transducers. Methods for measuring the change in voltage involve

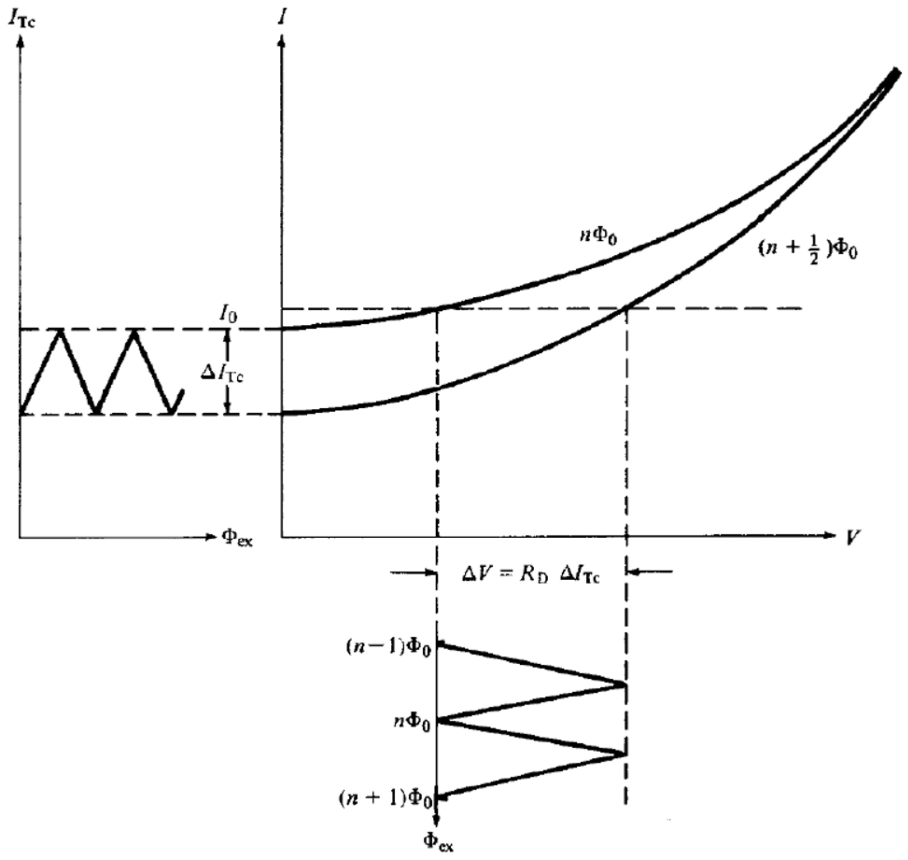

Figure 4.2: IV diagram for a SQUID in a magnetic field. The maximum value of voltage is at half integer multiples of the magnetic flux quantum while the maximum critical current of the SQUID is at whole integer values of magnetic flux. The SQUID IV is tracing between two minimum and maximum state IV curves[17].

tracking the voltage change along the more vertical portions of the transfer function, V-B curve, by inductively coupling a nearby external loop connected to feedback electronics.

The slope of the transfer function in the V-B curve plays a key role in the sensitive of the device. A higher slope means a small change to the magnetic field will cause a large change to the voltage across the SQUID. Creating a high slope and very linear transfer function can be achieved to maximizing ΔV which defines the height of the oscillations and minimizing ΔB the period of the oscillations.

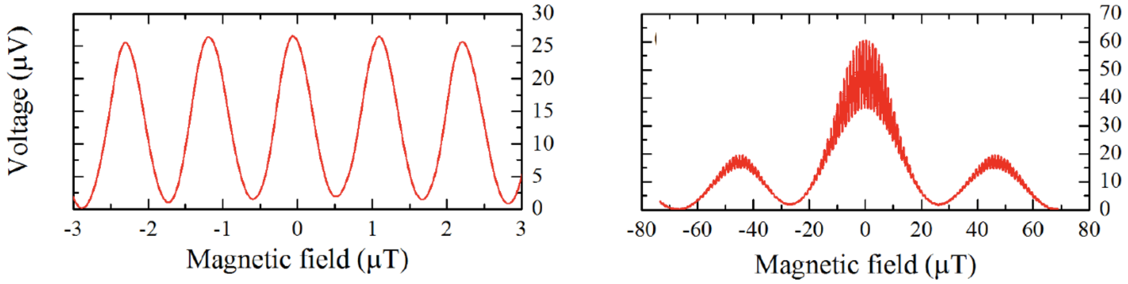

Figure 4.3: Voltage vs magnetic field figures: Double slit Fraunhoffer (Right) and zooming in on the interference pattern (left). [38]

ΔB will be set by the effective area of the SQUID. ΔV will be set by the $I_C R_N$ product and how efficiently it couples to external sources [40].

$$\Delta V = \frac{7}{\pi^2}\frac{I_C R_N}{1+\beta_L}\left(\frac{1-3.57\sqrt{K_b T L}}{\Phi_0}\right)$$

$$\Delta V \approx \frac{4 I_C R_N}{\pi \beta_L} - \frac{1}{\beta_L} \tag{4.2}$$

ΔV is maximized for valuse of β_L close to 1.

$$\beta_L = \frac{2 I_C L}{\Phi_0} \tag{4.3}$$

The inductance of a SQUID is the sum of 3 factors:

$$L_{TOTAL} = L_{SL} + L_K + L_J \tag{4.4}$$

Where L_{SL} is the geometric inductance of the material around the squid loop, L_K is the kinetic inductance and L_J is the inductance from the Josephson junctions.

Based on these equations ΔV can be maximized by: minimizing the total inductance, maximizing the R_N and keeping the I_C relatively low. For any SQUID the maximum $\Delta V \approx (2/3)I_C R_N$.

A final important relation in designing a SQUID is an approximation for the magnetic flux spectral noise density:

$$S_{\Phi_0}/2L \approx \frac{4K_bTL}{R} \tag{4.5}$$

S_{Φ_0} is the magnetic flux noise. Equation 4.4 shows that minimizing the inductance and maximizing the resistance of the device will lower the noise and allow for higher sensitivity to magnetic flux.

Chapter 5

Materials Discussion and Device Fabrication

5.1 $YBa_2Cu_3O_{7-\delta}$

YBCO is a high temperature superconducting material which gained much attention upon its discovery in the late 1980s. It is in a class of materials with a perovskite crystal structure and copper oxide chains of atoms in the a-b plane. The T_C of YBCO is 92K and it was one of the first materials discovered with a T_C above the temperature of liquid nitrogen, 77K [41].

Among the superconducting materials with a similar structure and T_C, YBCO became the most commonly used and studied for its relative ease in being grown as well as its hardness and strength making it easier to work with. YBCO is a ceramic material [42].

Figure 5.1 shows the crystal structure of YBCO. It is important to note the size the

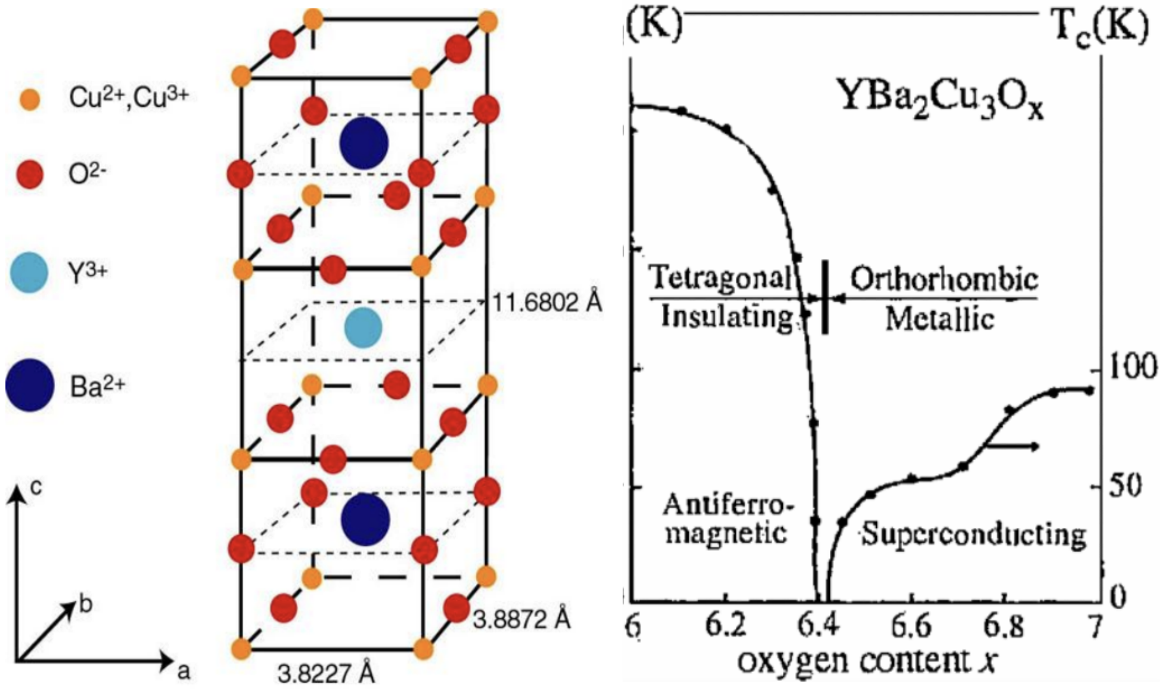

Figure 5.1: YBCO crystal structure and phase diagram for temperature and oxygen Stoichiometry. [43].

unit cell and the disparity in the lattice vectors. This material is highly Anisotripic and has vastly different electrical properties along the different lattice directions. For example, the superconducting critical current density along the a-b plane is 3 to 4 times the c direction. The much lower critical current density along the c axis makes it disadvantageous to design Josephson junctions with stacked herterojunctions. As a result, the majority of YBCO devices consist of junctions in the a-b plane[44].

The a and b lattice dimensions are very similar and changes to them can push the material between the tetragonal phase and orthorhombic phase. YBCO must be in the orthorhombic phase to be superconducting.

The $7-\delta$ in its chemical formula denotes an oxygen content between 6.0 and 7.0, where δ is a number between 0 and 1. We can see from the phase diagram how the oxygen content in YBCO plays a key role in its ability to and at what temperature it becomes superconducting. The oxygen content will also determine if the material is in its tetragonal or orthorhombic phase [45].

The electrical properties of YBCO can be vastly altered by defects that cause changes to its lattice constants or oxygen content. This sensitivity to disorder make it an ideal candidate for disorder induced device fabrication.

Another important phenomenon associated with YBCO is its energy gap. The energy gap of a superconductor is defined as the difference in energy between the highest superconducting state of the material and the lowest quasiparticle excitation. The energy gap of all BCS superconducting materials is well-defined, having no available states between superconducting and normal conducting states. Whereas materials like YBCO are considered gapless superconductors, such that when conductance is measured there are still states, though a drastic drop in them, between the superconducting states and the normal electronic states [46].

YBCO has a coherence length of $3-5nm$ depending on method of measurement and temperature [47]. The penetration depth of YBCO is on the order of several hundred nanometers [48]. YBCO is a type II superonductor. The superconducting gap at half the critical temperature is 30mV. The complexity of the unit cell as well as the stoichiometric sensitivity of the oxygen content make YBCO very sensitive to disorder.

YBCO has a relatively high room temperature resistivity of approximately $3\Omega\mu m$.

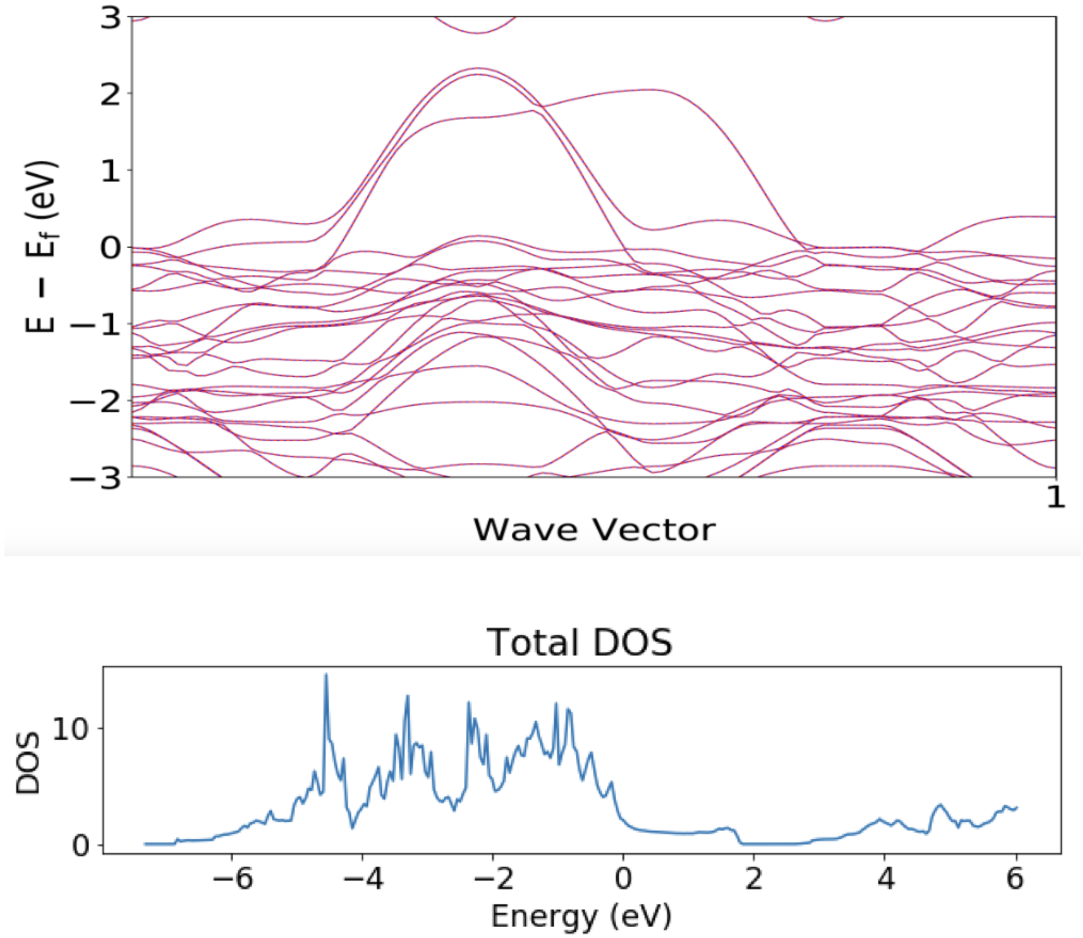

Figure 5.2: DFT calculation of the electronic band structure and Density of States of YBCO

I preformed calculations using differential functional theory, DFT, to further understand the electronic structure of YBCO. Figure 5.2 shows the electronic band structure and density of states of YBCO. We can see there are very few available states just above the fermi level.

5.2 Niobium

There are many elemental superconducting materials but the most widely used is Niobium. Niobium is one of the hardest metals and can be easily deposited as a thin film on a silicon substrate. Niobium has a T_C of 10.2K giving it the highest critical temperature of all the elemental superconductors [49][50]. The vast majority of superconducting electronics utilize niobium films because of its uniformity in structure resulting in low defect noise and its relatively high critical temperature.

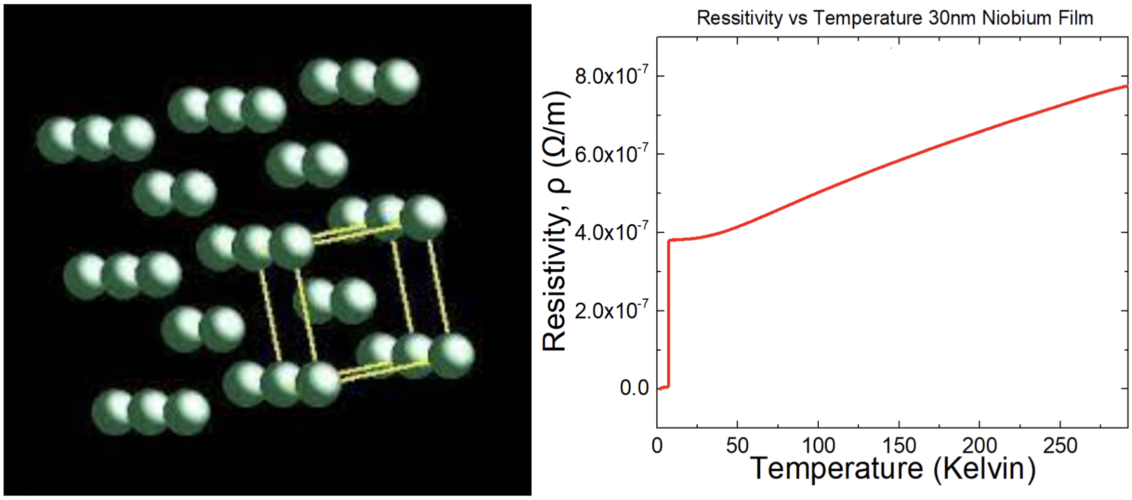

Figure 5.3: Left: Niobium (BCC) crystal structure. Right: sample RT graph of a 30nm Niobium film.

Niobium has a body centered cubic (BCC) crystal structure. Its lattice constant is $a = b = c = 3.3\mathring{A}$. Unlike YBCO, Niobium has a very closely packed, uniform and isotropic unit cell along with isotropic electrical properties.

Niobium has a coherence length of approximately 40nm and a penetration depth of approximately 40nm as well [4]. It is considered a type II superconductor.

The most common junctions in superconducting electronics are made using Niobium. A typical Niobium superconducting herterostructure type junction consist of a sandwich of materials: $Nb - Al - AlO_2 - Nb$. Here the aluminum layer acts as a growth layer for the few nanometer thick oxide layer which makes the insulating barrier of the Josephson junction. These type of Niobium junctions are typically $1\mu m^2$ to $5\mu m^2$ though some have recently been made as small as $0.5\mu m^2$ for use in superconducting digital circuits [51].

5.3 Fabrication

All the devices described in this thesis go through a similar fabrication process. We start with a wafer of the desired superconducting material. The wafer is diced into 0.5 cm squares. A pattern is designed on the computer with minimum dimensions of $0.7\mu m$. A photolithography laser writer system defines the pattern on a chip. Next, argon ion mill etch the features. Lastly the chip loaded into a helium ion microscope for nanometer resolution direct write of electrical components.

5.3.1 Lithography of Large scale Features

Both devices made from YBCO and Nb go through the similar lithography procedures. YBCO wafers are purchased from $CeracoGMBH$, and diced into 5cm squares. The wafers consist of a stack of a materials: sapphire or $LaAlO_3$ substrate, a CeO buffer layer, 30nm - 50nm thick YBCO layer and a 200nm thick gold capping layer. Niobium wafers Consist of a Si/SiO2 substrate and 30nm thick layer of Niobium.

Photoresist is spin coated at 5000 rmp leaving a $1.5\mu m$ thick layer. The chip is then loaded into a red laser photolithography system for the pattern to be defined. Chips are immediately developed revealing the desired geometry left behind photo in resist. Next we using Argon ion milling to etch the pattern using 500V acceleration of ions having an

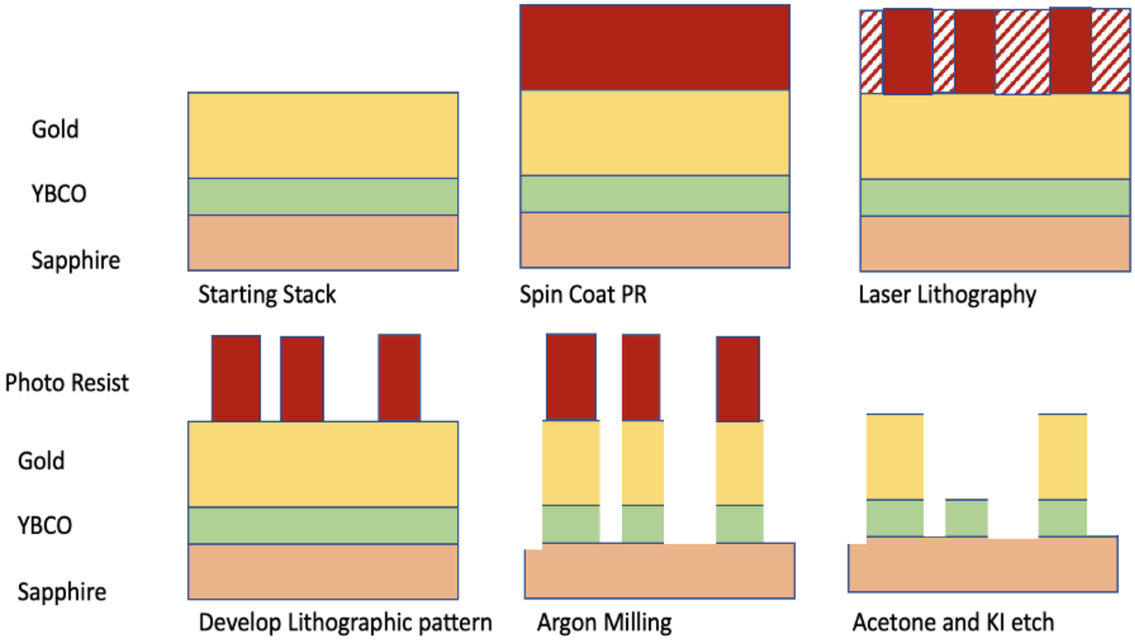

Figure 5.4: Steps of lithography progresses.

etch rate of around 0.25nm per second for YBCO or Nb but much faster for gold. We use 15 seconds on 45 seconds of shuttering throughout the milling process to avoid heating of the sample.

After milling, chips are thoroughly cleaned using solvents and ultrasonic vibration. To prepare the chips for the helium ion beam exposure we remove the gold capping layer in desired regions. We remove the gold through a second round of lithography and wet KI etch dissolving the gold while the ceramic YBCO unaffected.

5.3.2 Gas Field Helium Ion Microscopy

Gas field helium ion microscopy is a relatively new form ionized particle microscopy [52]. We use this tool to modify superconducting materials by bombarding them with high energy He^{+} ion to create disorder thereby changing their electrical properties [53][54].

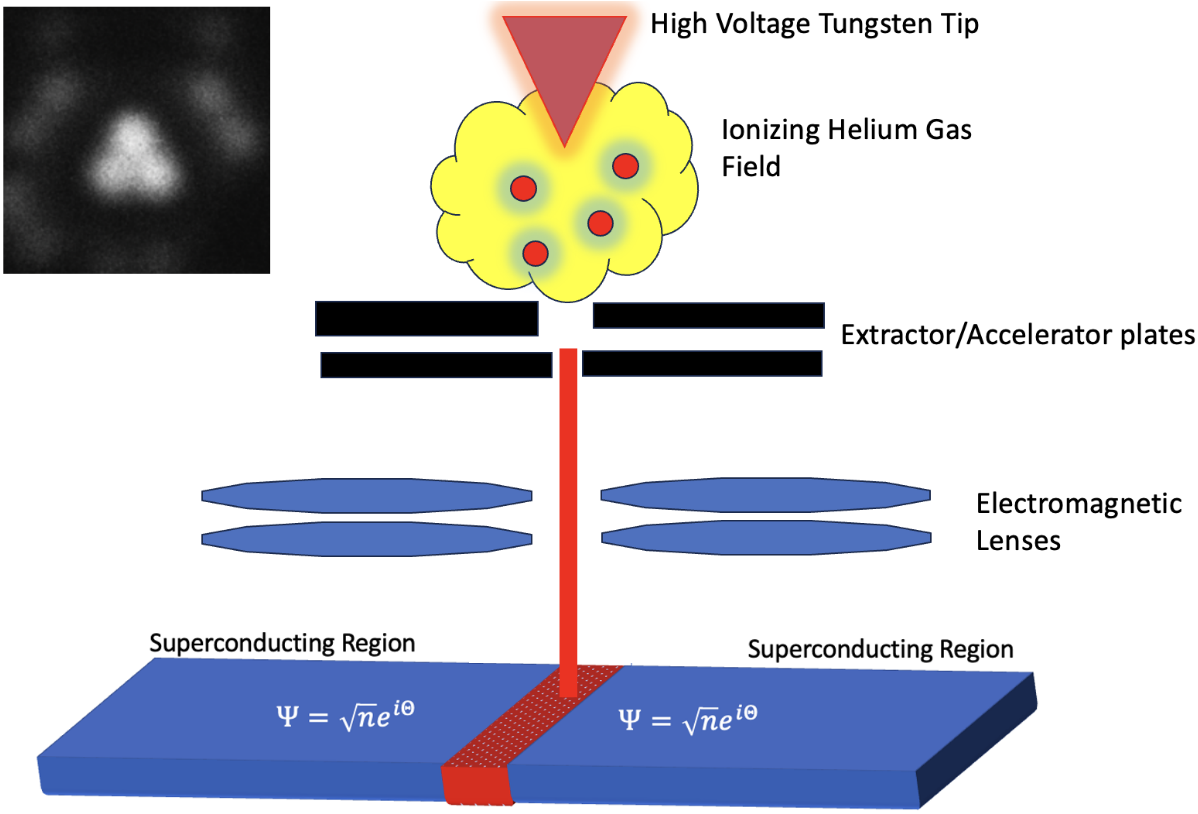

Figure 5.5: Schematic of HeIM microscope. The image in the top left is of a newly formed 3 atom tungsten tip.

First we sharpen a tungsten tip to a 3 atom point. High purity helium gas is introduced to the vacuum chamber surrounding the tungsten tip, raising the pressure from 3e-10 torr to 1e-6 torr. A high voltage is applied to the atomically sharp tungsten tip generating the massive electrical field needed to ionize the helium atoms. Helium atoms

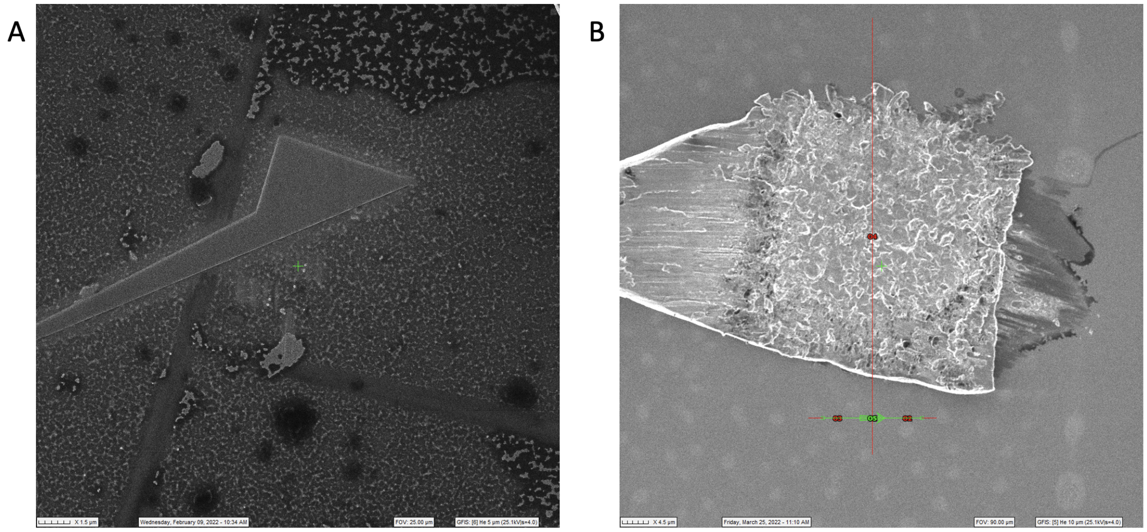

Figure 5.6: Helium microscope images. Left: ion induced Carbon deposit on gold speckled YBCO surface. Right: ultrasonic weld of Aluminum wire bond on Gold surface.

are accelerated through a voltage of 25KV when passing through extractor and accelerator plates. An aperture as small as $5\mu m$ is used to begin to create a tight beam of particles. A series of electromagnetic lenses are used to adjust stigmation, beam wobble, and focus, allowing us to achieve a spot size of 2nm.

As the beam is rastered across the sample secondary electrons are ejected. Regions of sample that are more conductive or contain sharp, more ridged, features will emit more secondary electrons. A nearby detector counts the number of electrons ejected and correlates the counts in time with the position of the beam. From electron counts and beam position, a micrograph is formed that allows us to image surface features with resolution of only a few nano meters.

The left image in figure 5.6 has a field of view of $5\mu m$. It shows a YBCO wafer where the gold has been partially etched with KI leaving behind splotchy gold patches. I deposited the geometric shape in the middle using gallium focused ion beam induced deposition. The right image in figure 5.6 has a field of view of $10\mu m$. It shows a ultrasonically cold welded aluminum-tin wire used to to electrically connect the sample.

Induced Disorder Fabrication of Superconducting Devices

One advantage of using helium atoms is they are chemically inert and do not react with the target material. Additionally, they are light and small and generate very limited sputtering the target compared with other ion microscopy methods.

All materials can be disordered or sputtered with a sufficient fluence of high energy ions. Using helium ion beam to directly write electronic features by induced disorder gives us the ability to create in-plane devices in the nano-meter scale. These devices take up significantly less space than conventional heterostructures produced with traditional lithography techniques.

YBCO has a complex and sensitive structure which makes it an ideal candidate for induced disorder electronic component direct writing. We can adjust the dosage of radiation to create Josephson junctions and resistive regions that allow zero conduction.

Figure 5.7 has fields of view: $A = 4\mu m$, $B = 5\mu m$, $C = 5\mu m$. All images are of YBCO surfaces. In image A I used area doses of $500 ion/nm^2$ to write the monicure 'UCR ONELab'. Recently irradiated areas often appear brighter due to charging of the material or a slight inflation of the material caused by implanted He^+ forming bubbles underneath the YBCO. Image B shows lines of dose $2000 ion/nm$. This dose is typically used to create resistive structures that no current can pass though. Between the rectangular structures is an undamaged 70nm wide region. We can see that the directly written resistive lines are only a few nm thick. Image C is taken while using insitu electronic connections applying a 5V bias across the bridge from top to bottom. There are a series of resistive lines written at 2000ion/nm making two trapezoids that form a narrow constriction. The lighter regions on the portion of the image above the irradiated lines shine brighter due to the bias voltage. The bias voltage raises the energy of the electrons creating lower ejecting energy gap. We can see the bottom half of the image is darker. This is due to the constricted region creating a highly resistive area drastically stepping down the potential on the lower half of the image.

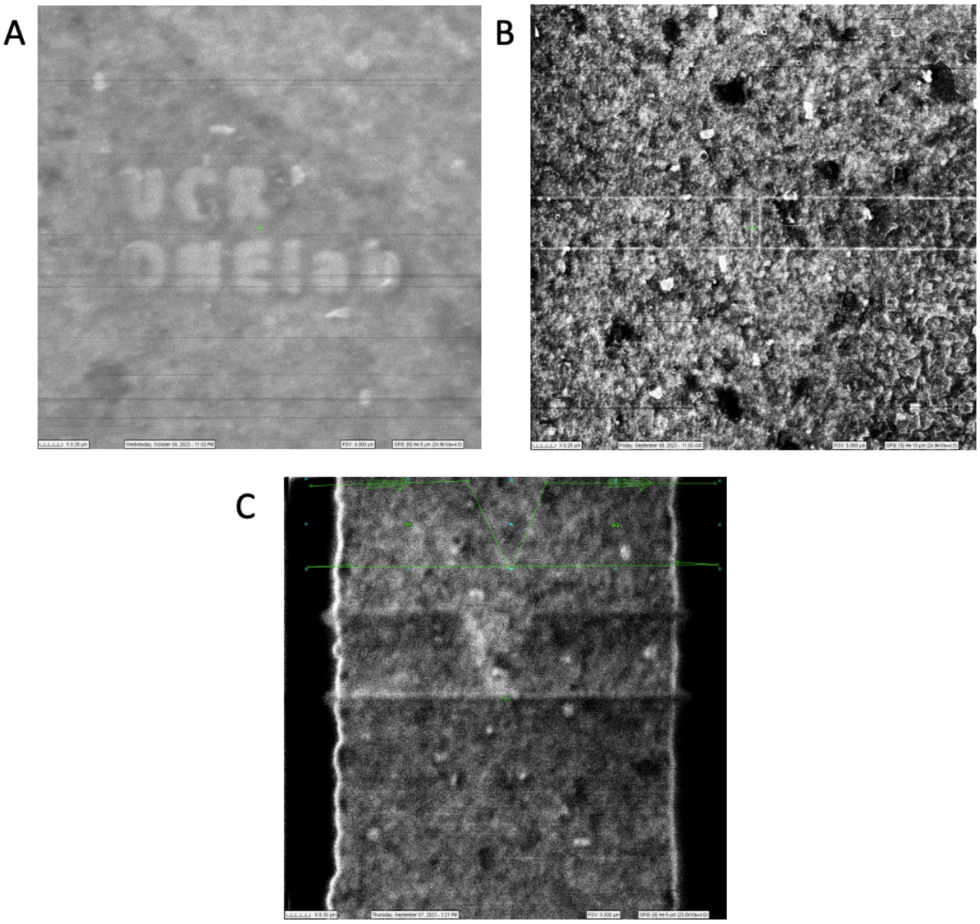

Figure 5.7: Helium microscope images with Irradiated regions.

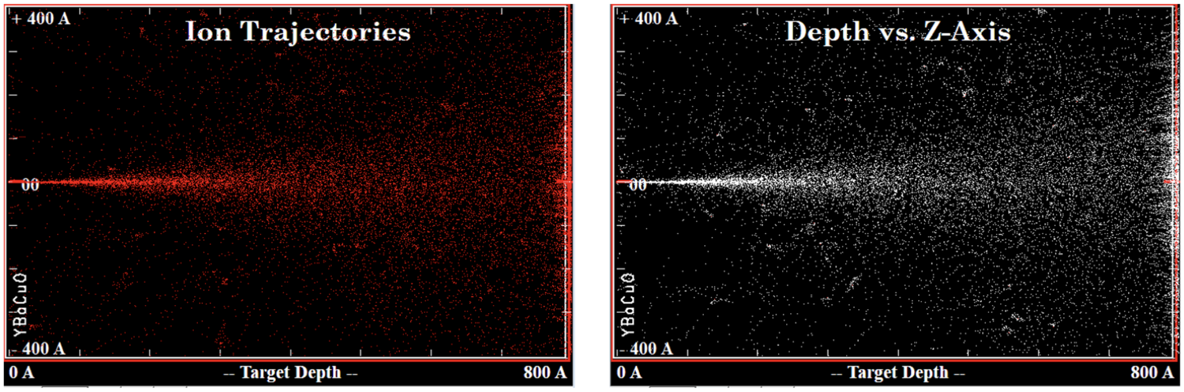

Figure 5.8: TRIM Ion beam simulation of particle trajectory and implantation: He^{+} into YBCO

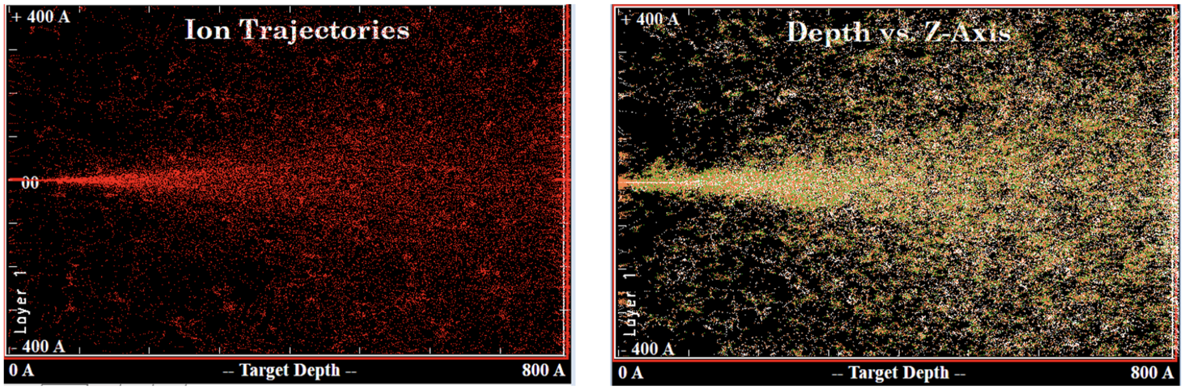

Figure 5.9: TRIM Ion beam simulation of particle trajectory and implantation: He^{+} into Nb

Figure 5.8 and figure 5.9 show TRIM simulations of 25keV heilum ions impacting and implanting throughout a YBCO target in figure 5.8, and Niobium target in figure 5.9. In both figures 1000 ion trajectories and implantations were simulated on a chunk of material 80nm deep. We can see how upon entering the target material the particle trajectories remain in a small region but begins to spread out rapidly the farther the ion enters the material. The ions stay closely together for the first 35nm in YBCO and the first 20nm in Nb. The distance at which the trajectories spread out is smaller for Niobium than

YBCO due to the Nb having tighter packed unit cell, shortening the mean collision time and distance. We see a similar effect in the images titled Depth vs z-axis. This image shows the stopping location for each ion. The majority of the particles in both images implant past 40nm of material. These properties of helium ion bean material interaction restrict us to using superconducting films with thickness less than 50nm in fabricating our devices.

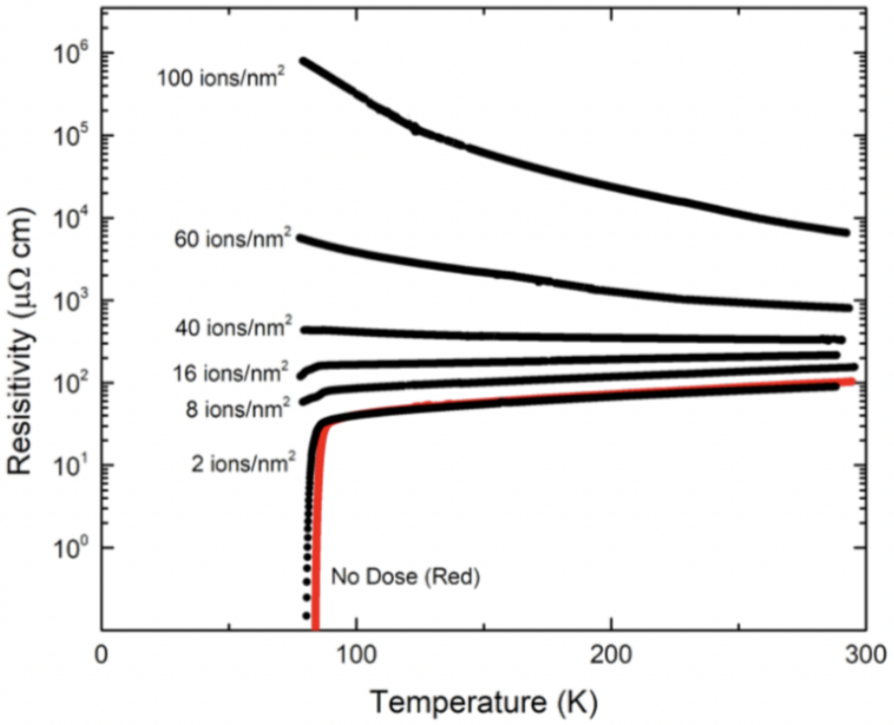

Figure 5.10: Resistivity vs temperature graph of YBCO. Each line is a different dose of 30keV helium ions.

As mentioned earlier, the main parameter in changing the electrical properties of the irradiated films is the dose of ions implanted through the material. Figure 5.10 shows resistance vs temperature curves for YBCO film at a range of ion doses. As the dose increases the resistance changes especial deviating from the non radiated film at low temperatures. The varying doses change materials electrical properties. At low dose radiation we see a reduction in lowered T_C. At a moderate dose we see that the normally superconducting material will weakly conduct below T_C. Under the higher doses the material become increasingly insulating and can have enough impedance to break the circuit.

In summary, Helium ion beam fabrication allows us to determine the geometry of a circuit to the nano meter scale and to create a variety of insulating barriers only a few nano meters thick. The Josephson junctions in this thesis are fabricated by precisely choosing a dose to directly write a disordered thin barrier region. The geometry of the junctions can be modified by writing much higher dose lines around them constricting their size.

Chapter 6

YBCO Superconducting Devices

All YBCO films are subject to minute crystallographic differences in defect concentration and stoichiometry. The devices in this thesis are made of films with thickness between 25nm and 40nm. Before device fabrication it is important to get a baseline of the material transport properties. A precise measurement of resistance vs temperature can give a lot of information that is helpful to our process.

Figure 6.1 is a typical RT measurement of a YBCO film. This is a four-point probe measurement taken across a $4\mu m$ wide bridge. We measure the voltage across a path of applied current using a SR560 pre-amplifier. The output of the voltage pre-amplifier is fed to a lockin-amplifier to integrate and time average and return an output of 'dV: differential voltage'. This signal is then fed into a DAC and to a LabVIEW program which records the data. The current signal is measured using a known resistor in series with the YBCO film. We measure the voltage across the known resistor using a second pre-amplifier and use Ohm's Law, V=IR, to determine the value of current through our circuit. Similarly to

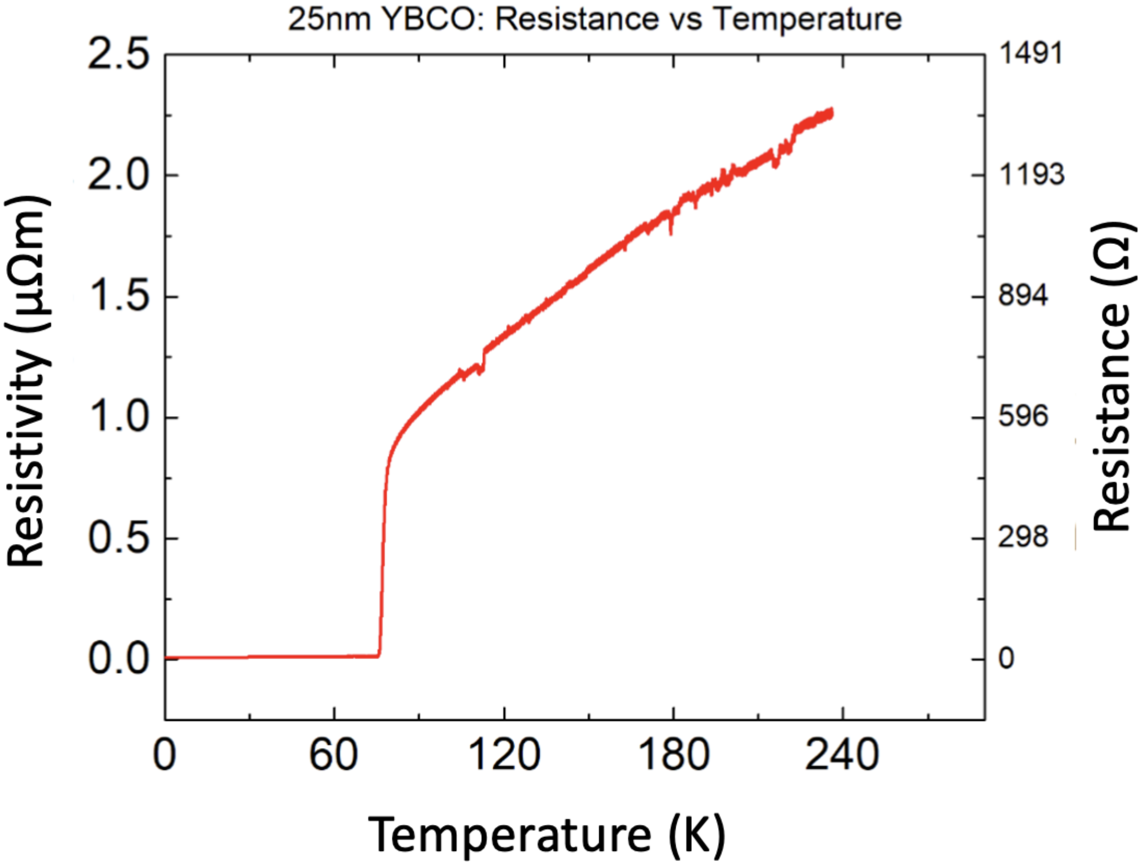

Figure 6.1: Resistivity and Resistance vs temperature graph of 25nm YBCO film.

the voltage measurement, this signal is fed from the pre-amplifier into a lockin-amplifier for time averaging and integration then to a DAC and into the computer for recording of 'dI, differential current'.

It is important to note the relatively high resistivity of the film above T_C. YBCO is a semi-metal with low conductivity above T_C. The resistivity gradually decreases with temperature, indicative of the increased mobility of the charge carriers. The T_C of this film is 83 Kelvin. However, this phase change is not instant in this figure. The temperature range over which the material changes to its superconducting phase is often refereed to as ΔT_C. A larger range of ΔT_C is indicative of a less uniform the film. ΔT_C can also be greatly affected by the rate of change of the temperature, the distance between the temperature measurement and chip as well as the speed and accuracy of the collected data. Other low temperature less complex superconductors have a much smaller ΔT_C. YBCO will often have a ΔT_C of at least 2 Kelvin.

6.1 HeFIB YBCO Josephson Junctions

To make complex electronics using helium focused ion beam fabrication of induced disorder in YBCO films it is important to first calibrate the correct ion dosage needed. There are many device and system constraints when designing a Josephson junction: operating temperature, size, critical current and normal state resistance.

There can be many differences between the junctions written on the same chip with different dose but most Josephson junctions fall into one of two categories SNS or SIS.

SIS stand for superconducting - insulating - superconducting describing the sandwich of material making the junction. SIS junctions typically have small critical current and a large normal state resistance. The R_N will increase as temperature decreases. For SIS junctions the I_C will increase as temperature decreases as well, but will hit a maximum at some temperature. SIS junctions typically operate below 40K. SIS junctions are true tunneling devices that allow us to do in-plane spectroscopy of the material to learn about the superconducting gap and density of states of the material.

SNS stands for superconducting - normal metal - superconducting. SNS type junctions have a much wider operating temperature range from around 5K up to 70K. At lower temperatures the coupling between the two superconducting regions becomes stronger and the excess current through the junction dominates the critical current. Below 15K a 4 micron SNS junction can have critical current as high as a miliamp. In this state most of the critical current is not due to Josephson tunneling and will not follow the Josephson equations and characteristics. Above 70K the coupling is typically too week and there is generally very little non-linearity to the IV curve. SNS junctions often decrease in resistance as temperature goes down.

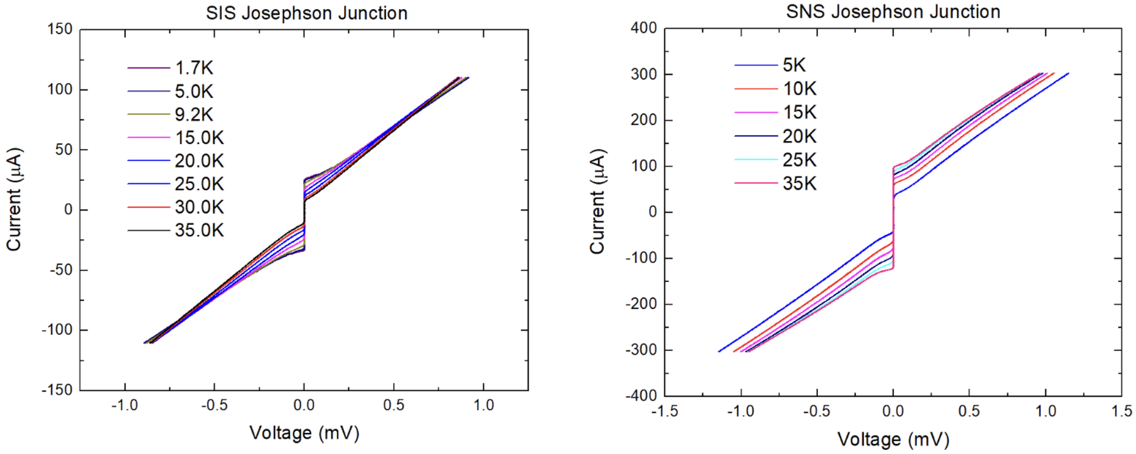

Figure 6.2: IV characteristic of SNS and SIS Josephson junctions written with different does of helium ions

Figure 6.2 shows typical IV curves for SIS and SNS junctions at various temperatures. There are a few key differences between them. First the curves in the SIS junction join up past 0.5mV whereas the curves in the SNS junction do not. The most notable difference between these two sets of curves is how much higher the normal resistance is for SIS compared to SNS and how much lower the critical current is for SIS compared to SNS.

Figure 6.3 shows a differential conductance measurement and an IV curve of the same device. As YBCO is a 'gapless' superconductor there are states, though a drastic drop in density, inside the gap. This measurement was taken at 4.2K. The gap in this measurement is about 30mV which is typical for YBCO in plane junctions at this temperature. The sharp spike in conductance at the center of the figure is due to the critical current of the device.

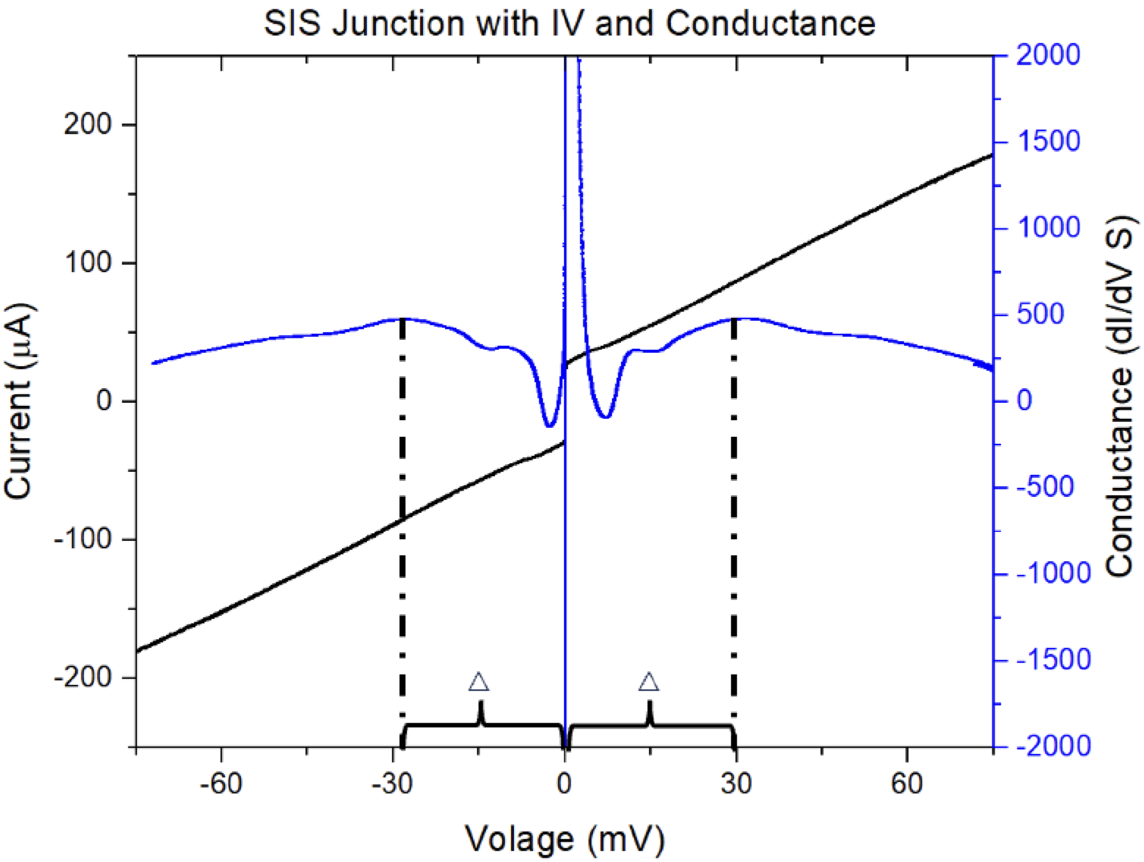

Figure 6.3: IV and conductance characteristics of a YBCO SIS in plane tunnel junction.

6.1.1 Magnetic Field Effects

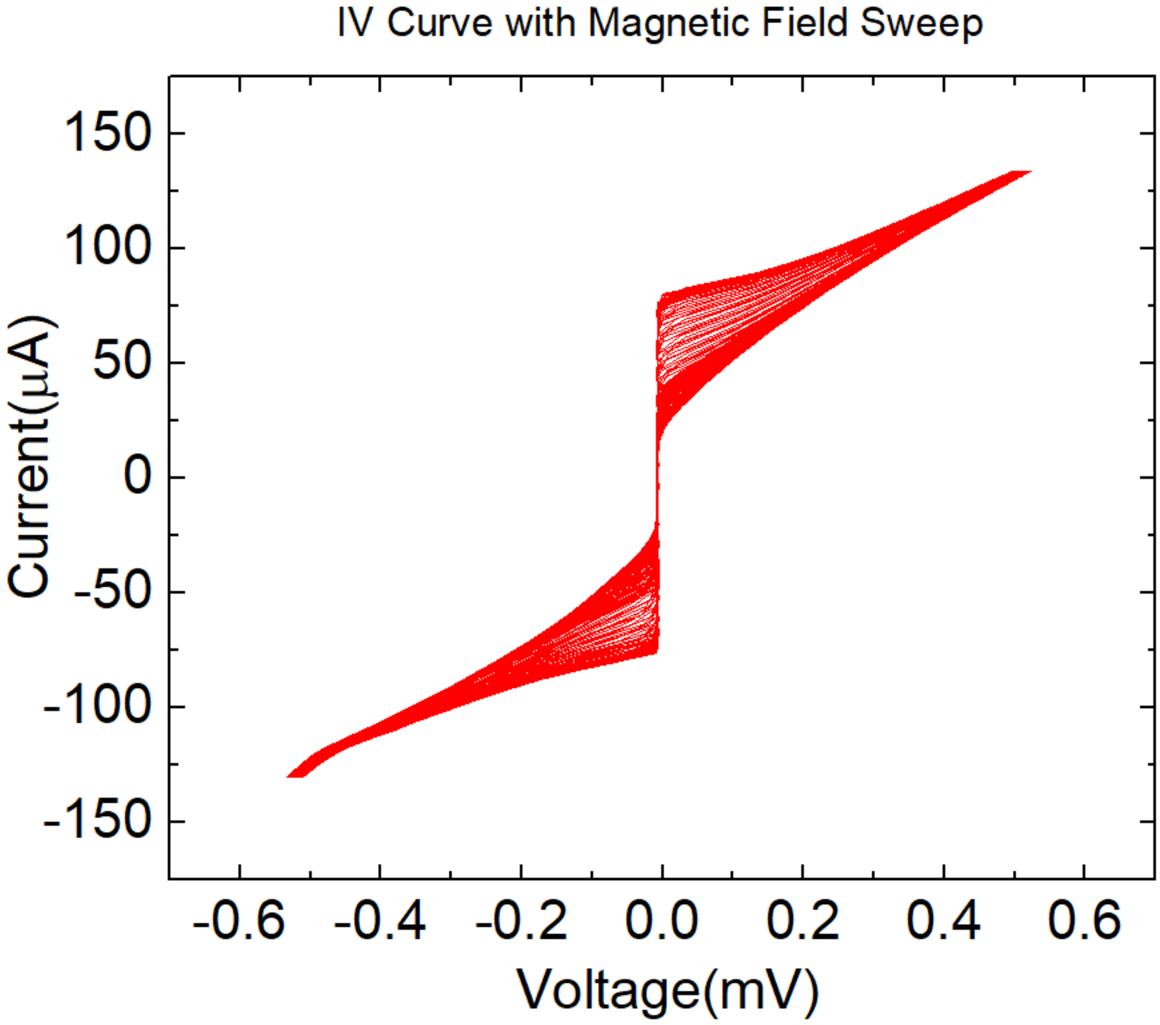

Figure 6.4: Effects of magnetic field of IV curve of YBCO Josephson junction.

Figures 6.4 and 6.5 show the effects of magnetic field on a YBCO in plane junction written with helium ion beam induced disorder. This measurement was done at 10K. Figure 6.4 Shows the IV characteristics of the junction. An external magnetic field applied

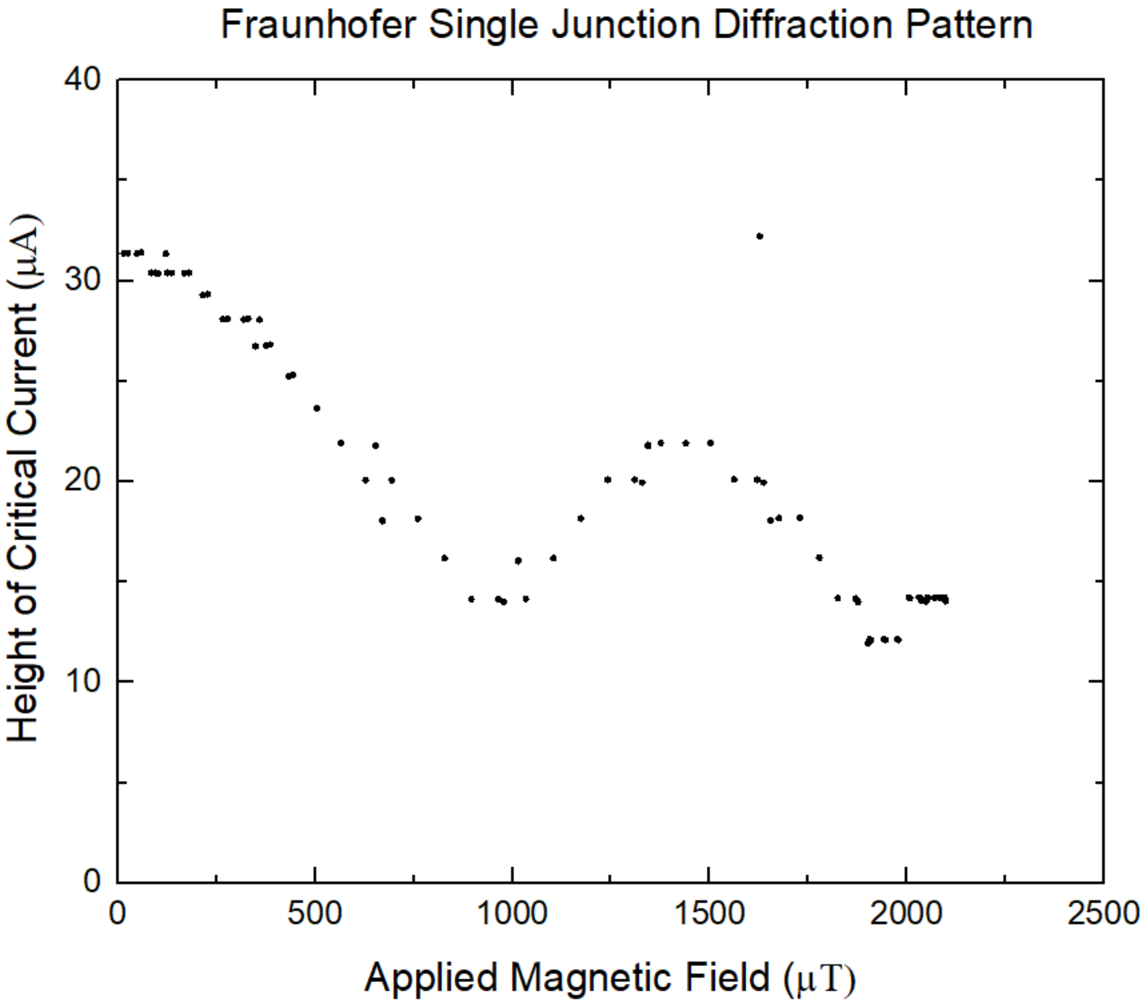

Figure 6.5: Fraunhofer diffraction pattern of I_C vs magnetic field.

perpendicular to the junction is swept from 0 to 2250 micro tesla at a very slow rate while the current is swept at a much faster rate. This allows me to collect a few hundred IV curves each at a different value of magnetic field going through the junction in a single data file. We can see in this figure how the critical current is affected while the normal resistance remains constant. It is also important to see that the critical current never goes to zero. The critical current that remains is due to non-Josephson excess current that is not subject to the effects of the magnetic flux. This measurement illustrates how much excess current flows in a junction at a specific temperature.

Figure 6.5 depicts the Fraunhofer diffraction patter that results from the fluctuation in critical current. The height of the critical current is plotted against applied magnetic field. Here it is clear to see how much critical current remains at the minimums of the oscillations. This is a great way to measure how much of the critical current in the IV is due to non-Josephson charge flow. In this case there is a about 12 micro amps of the total 75 micro amps of critical current that result from non-Josephson charge flow. This junction is 3.2 microns wide and results in the first minimum of the Fraunhofer pattern existing at 900 micro tesla.

6.1.2 AC Effects

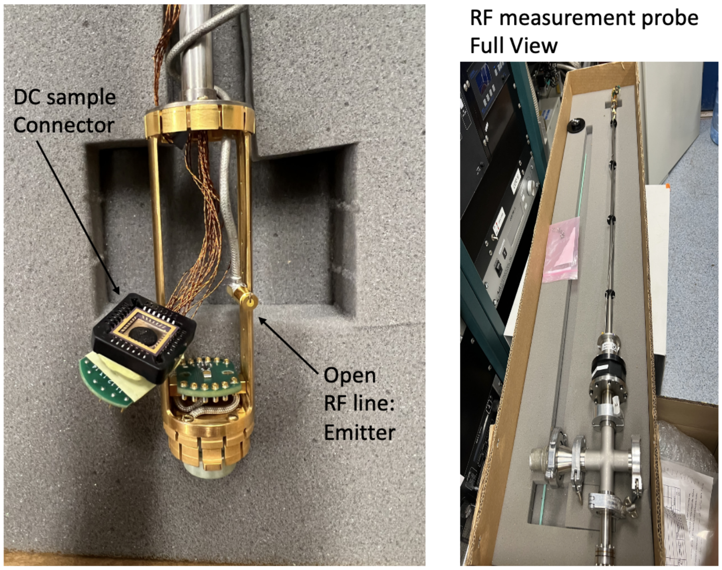

Figure 6.6: Picture of RF probe and probe head.

For the purposes of creating an AC emitter, we modified a probe made by Quantum Design for use in a PPMS pulsed tube cooler. The modified probe contains an RF line that is hooked at the end dangling near the YBCO chip. The high impedance of free space at the end of the line allows this system to perform as a low-cost antenna emitting electromagnetic radiation at a frequency generated by a Hewlett Packard microwave synthesizer. The EM waves couple to the chip and produce an AC bias across the device.

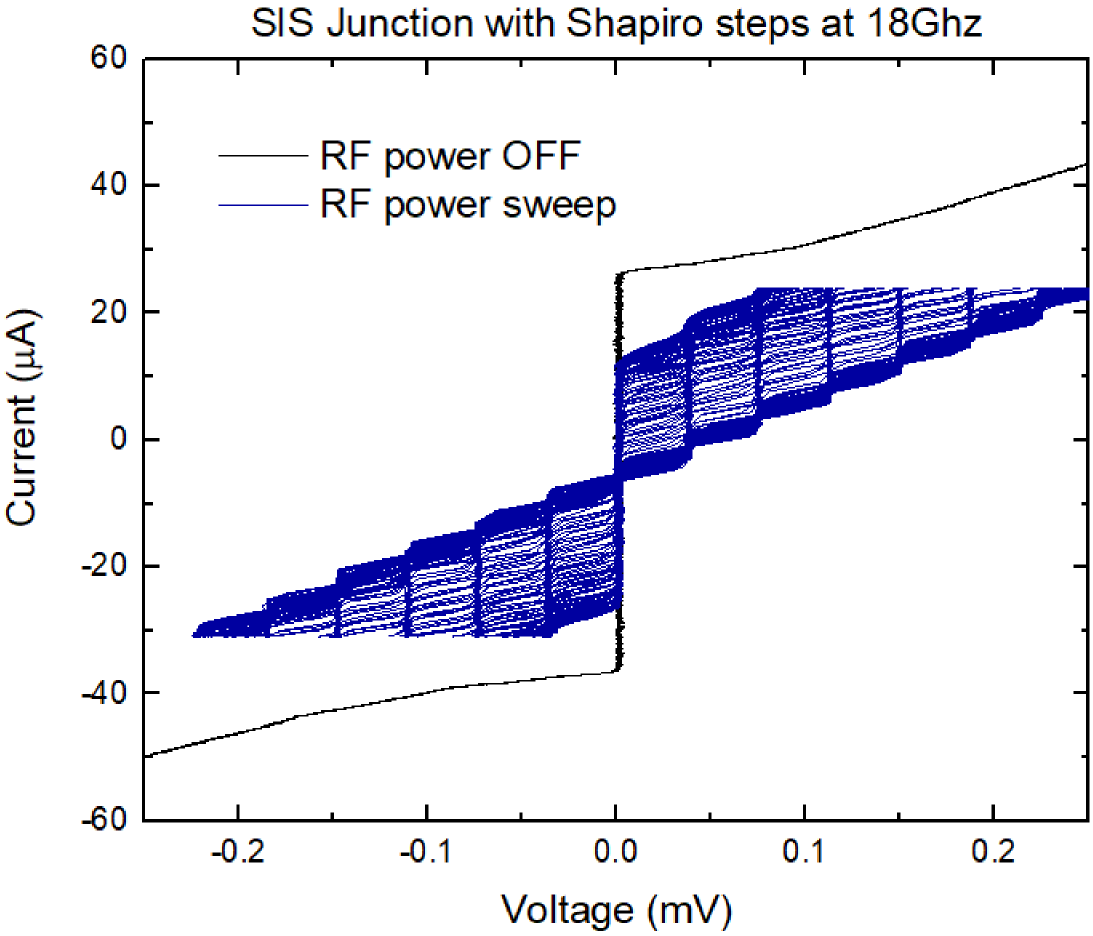

Figure 6.7: Effects of 18Ghz radiation on YBCO Josephson junction.

To take the measurement shown in figure 6.7, I set the microwave synthesizer to 18Ghz and sweep the power of the microwave signal from -1 db to 15db. While the AC power is slowly changed from low to high, the current bias continues to sweep at a faster rate. This allows me to record several IV curves in a single data set showing the effects that a range of power amplitudes have on step height.

As power increases the n=0, central critical current line decrease in height. The constant periodicity of the Shapiro steps is a manifestation of the equation: $V = \frac{nh\omega}{2e}$. The height of the steps follows a Bessel function dependence. At high enough AC power, the energy from the radiation inside the junction suppresses all critical current and all Shapiro steps disappear leaving a a line at the same slope as the normal restive region.

6.2 YBCO Superconducting Quantum Interference Devices

6.2.1 High-TC Superconducting Quantum Interference Device Implemented on a Pulsed Tube Cooler for 1 to 50 K Materials Characterization

Superconducting Quantum Interference Devices (SQUIDs) used as a detector of magnetic flux is a valuable materials and device characterization method. Short range materials characterization techniques like magnetic force microscopy, or spin-polarized scanning tunneling microscopy provide excellent results for local field sensing with high spatial resolution [55][56]. However, SQUID based detectors are complimentary in that they can detect flux and provide long range information and high sensitivity. This enables SQUID based systems to have less stringent sample cleanliness requirements and lowers engineering constraints [57].

Most SQUIDs are fabricated from Nb- Al_2O_x - Nb Josephson junctions because they have excellent electronic properties and are commercially available. Low-T_C SQUID sensors operate at 4 K and require thermal insulation for measurements at higher temperature. Furthermore with the ever increasing costs associated with liquid helium there is a need for SQUID sensors that operate on liquid free cryogen platforms. Using SQUIDs to examine samples at elevated temperatures is very challenging which motivates the use of high temperature superconductors (HTS). Unfortunately, HTS junction development is not as robust as niobium-based sensors. This is because HTS materials are very difficult to grow and Junction fabrication is complicated by the necessity for current to flow through the $a - b$ plane of these materials [58]. As well, traditionally fabricated junctions in HTS films usually yields weak-link style junctions that become strongly coupled at low temperatures and no longer operate. However, it has recently been shown that junctions defined by helium ion irradiation can operate from 80 K to low 4 K temperatures. In this work, we present a High-T_C SQUID probe system, unshielded from external magnetic fields, that can operate from (1 - 50 K) on a mechanical refrigeration system without thermally isolating the sensor from the sample. This allows the sensors to get much closer to the signals of interest for more sensitivity and better spatial resolution.

$YBa_2Cu_3O_{7-\delta}$ (YBCO) is one of the most commonly used high-T_C superconducting materials. Recent advances in the use of a focused helium ion beam (FHIB) to produce Josephson junctions allow us to directly write planar SQUIDs into YBCO films [59]. Josephson junctions fabricated with FHIB can function between 1K to 50K and maintain their insulating characteristics. This allows for the development of SQUIDs that have a larger operating temperature range while maintaining consistent electronic response. Here we describe the design and characterizations of direct-coupled single layer SQUIDs [60][60] designed for magnetic materials and device analysis in the Quantum Design Dyna Cool physical property measurement system (PPMS). The probe, electronics, and optics were custom-built by Quantum Design engineers. It featured a piezo stage and camera for sample alignment. The external electronics consist of a Quantum Design flux locked loop with 1 kHz bandwidth designed for these SQUIDs.

Figure 6.7.A depicts the full chip design with 8 sensors. Figure 6.7.B is an Image of 300 μm diameter sensor. Bright yellow is the gold contact layer on top of the YBCO film. The orange background is the sapphire substrate. Figure 6.7.C is a close up image of the region where the SQUID loop and junctions are defined by Helium ion beam irradiation.

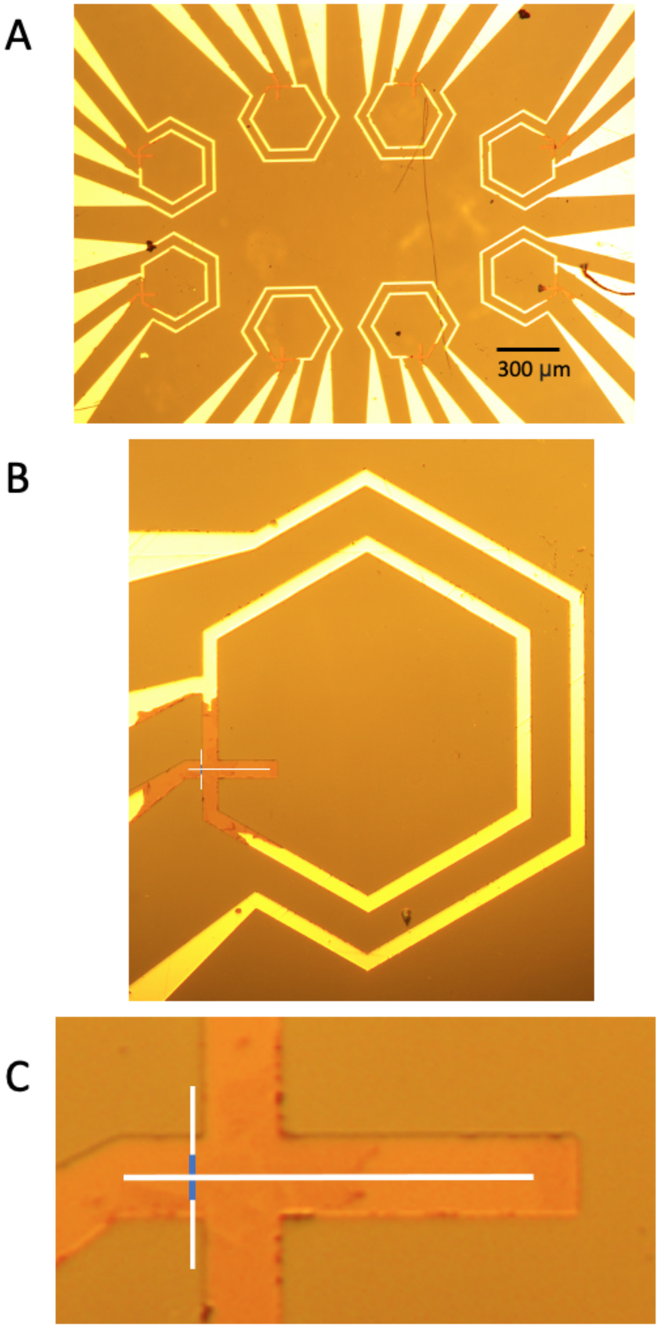

Figure 6.8: A: Full chip design with 8 sensors. B: Zoom to 300 micron field of view showing modulation coil and flux focusing loop directly coupled to the SQUID. C: SQUID loop in white and junctions in blue directly written with HeFIM

Gold is etched away from this region by KI/I etchant so that the ion beam can access the underlying YBCO layer. The white lines represent where the beam was scanned with a relatively high ion dose to convert the material from metallic to insulator (1 × 1018 ion/cm). The blue lines are irradiated with a smaller dose to create the junction barriers (1 × 1016 ion/cm). The horizontal white line is a long insulating nanoslit that forms the SQUID loop. Additional high dose white lines were written on the sides of the junction to shorten the junction to 400 nm to increase the resistance.

The fabrication of these SQUID sensors consists of two processes, photolithography for large scale features and focused helium ion beam material modification for nano scale features and junctions. YBCO thin films with a thickness of 40 nm were grown on cerium oxide buffered sapphire by Ceraco GmBH. A 200 nm thick film of gold was evaporated insitu on top of the YBCO to serve as electrical contacts. Waferes were diced into 5 mm by 5 mm chips, large scale features are defined with photolithography and etched with a broad beam Kaufman argon ion mill. The gold contact on the rectangular finger that enters the hexagon is etched by potassium iodine wet etch. Removing the gold in this region allows the helium ion beam to access the underlying YBCO. Each sensor has a 300 μm pickup loop directly coupled to the SQUID loop to increase sensitivity to magnetic field. The outermost partial hexagonal loop is used as a single turn modulation and feedback coil for the fluxed locked loop electronics.

After the patterning of large features, samples were then irradiated in a Zeiss Orion NanoFab helium ion microscope to create a nanoslit SQUID [62] shown in Figure 7.6.C. The nanoslit SQUID body is 60 μm long by 2 nm wide and is written on the rectangular finger on the side of the hexagon. The line for the SQUID slit was written with a dose of 1×10^{18} ion/cm. This relatively high dose of irradiation sufficiently disorders the material creating a very insulating region that defines the SQUID loop. The Josephson junctions were written just below the edge of the hexagon and trimmed with two large insulators to 400 nm. The junctions were written with a dose of 1×10^{16} ion/cm. This fabrication method allows us to tune the junction geometry to control the junction critical current and normal state resistance. Magnetic flux in the larger hexagonal pickup loop is directly coupled into the SQUID. The high resistance, $R_N = 10.5\Omega$ of junctions help increase coupling by ensuring the coupled circulating current transverses the long direction of the SQUID for strong coupling.

The device was biased near the critical current while an external magnetic field was swept through a large enough range so that 3 - 4 periods of modulation can be seen. The periodicity of 275 nT/Φ_0 corresponds to an effective sensor area of 80 μm^2. We characterized this SQUID at temperatures ranging from 50 K to 4 K in a liquid helium dip probe system. As shown in Figure 6.8, the minimum modulation is 35 μV for the 50 K measurement while the maximum was 495 μV for the 18 K measurement. These large modulation voltages are due to the high device resistance, $R_N = 10.5\Omega$ we achieve by trimming the bridge with an insulating dose shown as white vertical lines in Fig.6.7.C. The voltage amplitude increases with decreasing temperature and reaches a maximum around 18 K. At lower temperature we see a reduction in the modulation voltage which we attribute to an increase in the inductive parameter β_L from the increase in critical current. We observed that the temperature dependence of the critical current initially increased with decreasing temperature but obtained a maximum value at the lowest temperatures, consistent with

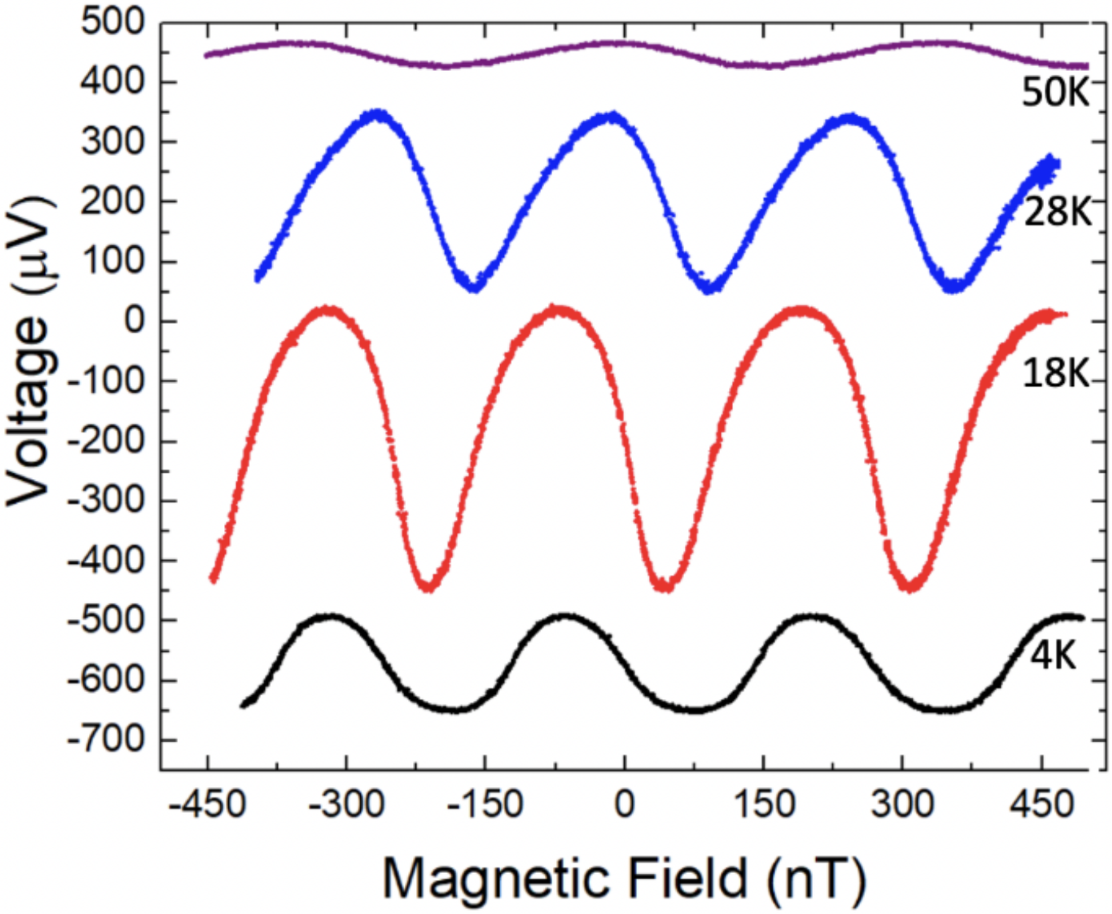

Figure 6.9: SQUID magnetometer magnetic field vs voltage characterization.

insulating barrier junctions previously fabricated by our group.

The physical property measurement system (PPMS) in Figure 6.9.A is used to monitor and control sample and SQUID temperature. It features a low vibration pulsed tube cooler and Quantum Design proprietary control electronics. A custom PPMS probe insert was designed for this work. In the probe, the sample sits on a piezo stage mounted on the probe head that allows the user to control the position of the sample relative to the

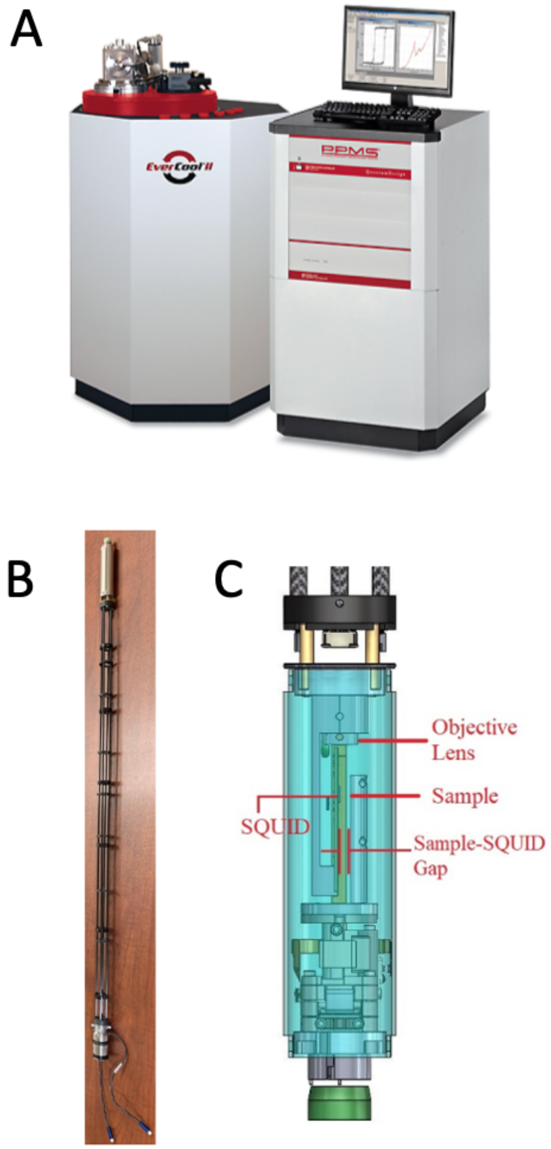

Figure 6.10: A: PPMS pulsed tube cooler. B,C measurement probe and probe head with piezo stage sample mount and squid holder.

sensor, shown in Figure 6.9 B and C. The piezo stage has spatial resolution of one micron in x, y and z directions. The integrated cryogenic camera that enables visual alignment has a resolution of 2 μm. Camera resolution was tested by optically imaging individual lines

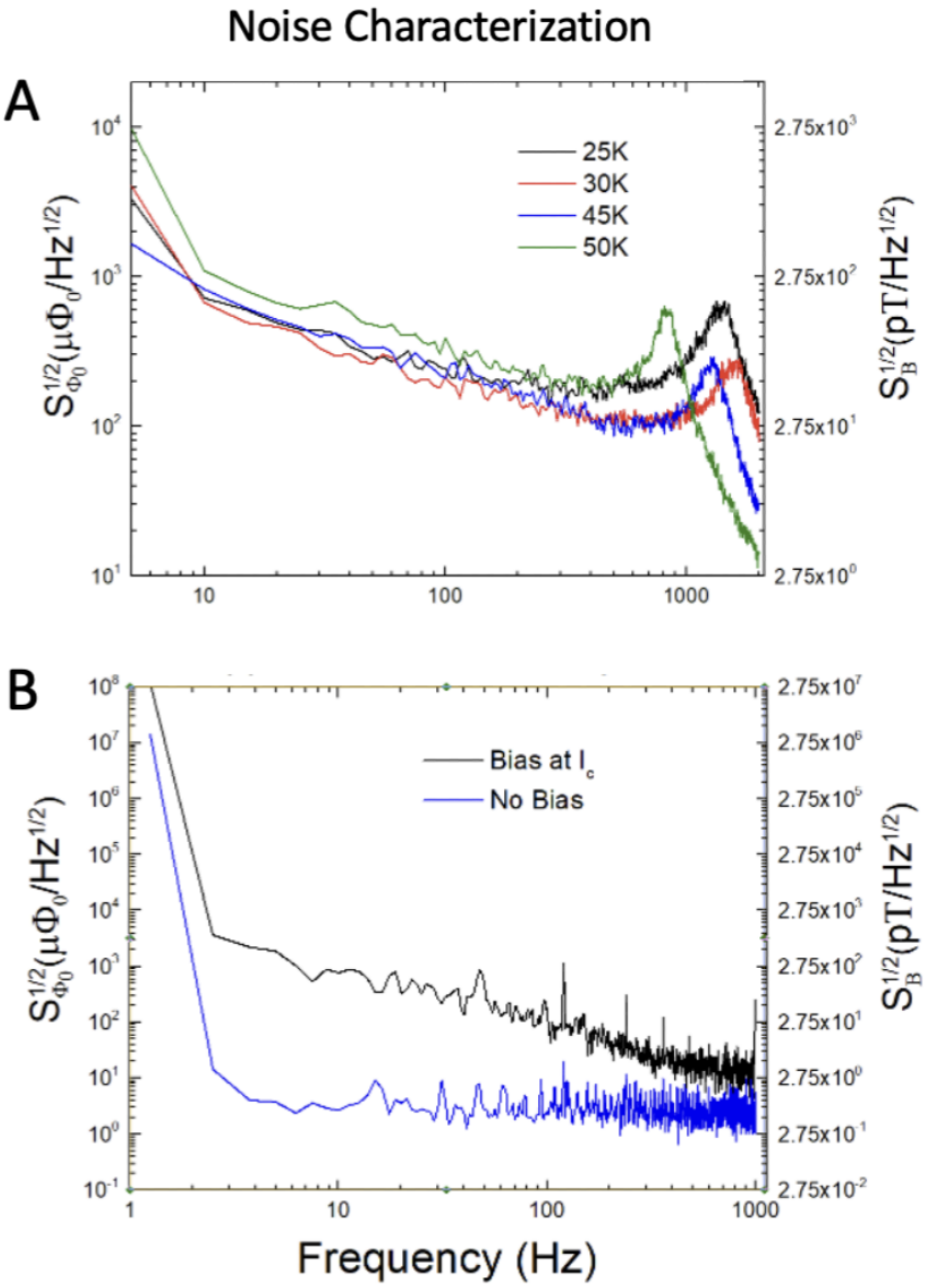

Figure 6.11: Noise spectrum density characterizations in pulsed tube cooler, A, and in liquid dip probe measurement system.

within group 8, element 3 of the 1951 USAF resolution test chart.

Figure 6.10.A is the noise characterization of the SQUID chip operating in the PPMS. Data were taken at temperatures ranging from 50 K to 25 K using a Quantum Design flux locked loop with modulation frequency of 500 kHz and a bandwidth of 1 kHZ. For frequencies between 100 Hz and 1000 Hz, the noise ranges from 25-100 pT/$\sqrt{Hz}$. Above 1000 Hz, filtering causes the increase and decrease of the spectra. This SQUID system has an operating temperature range from 1 to 50 K and the ability to detect changes to magnetic field as low as 25 pT. The sensor is in an environment unshielded from Earths magnetic field and near the pulsed tube cooler electronics which adds to the noise. In fig. 6.10.B we show a noise spectra measurement conducted of a device with the same layout and from the same wafer. This measurement was done by directly measuring the voltage of the SQUID with a spectrum analyzer with dc current bias above and below the critical current. This characterization results in a noise level of 10 pT above 100 Hz which is higher than measurements reported in our previous work. However, we remark that this measurement was performed without magnetic shielding, without a FLL and without bias reversal. Therefore, it can only serve as an upper limit on the intrinsic noise of these SQUIDs.

These results show the development of a novel SQUID system that allows for high resolution magnetic measurements over a wide temperature range. The advanced cryogenic optical piezo positioner allows the SQUID to be in close micrometer proximity which improves detection. Furthermore the sample can be moved with respect to the sensor for in plane resolution or alignment. We believe magnetic shielding for the probe-head and improvement of the flux locked loop with bias reversal will greatly lower the critical current noise for better performance. By scaling down the sensor size using FHIB techniques, this instrument may be able to sense magnetic phase transitions, magnetic vortex formations and other nanoscale magnetic phenomena.

6.2.2 Low Noise Direct Inject SQUID Characterizations

After making a SQUIDS for the purpose of a wide temperature range magnetic sensing applications, I shifted my focus to making a lower noise squid with similar sized pickup loop.

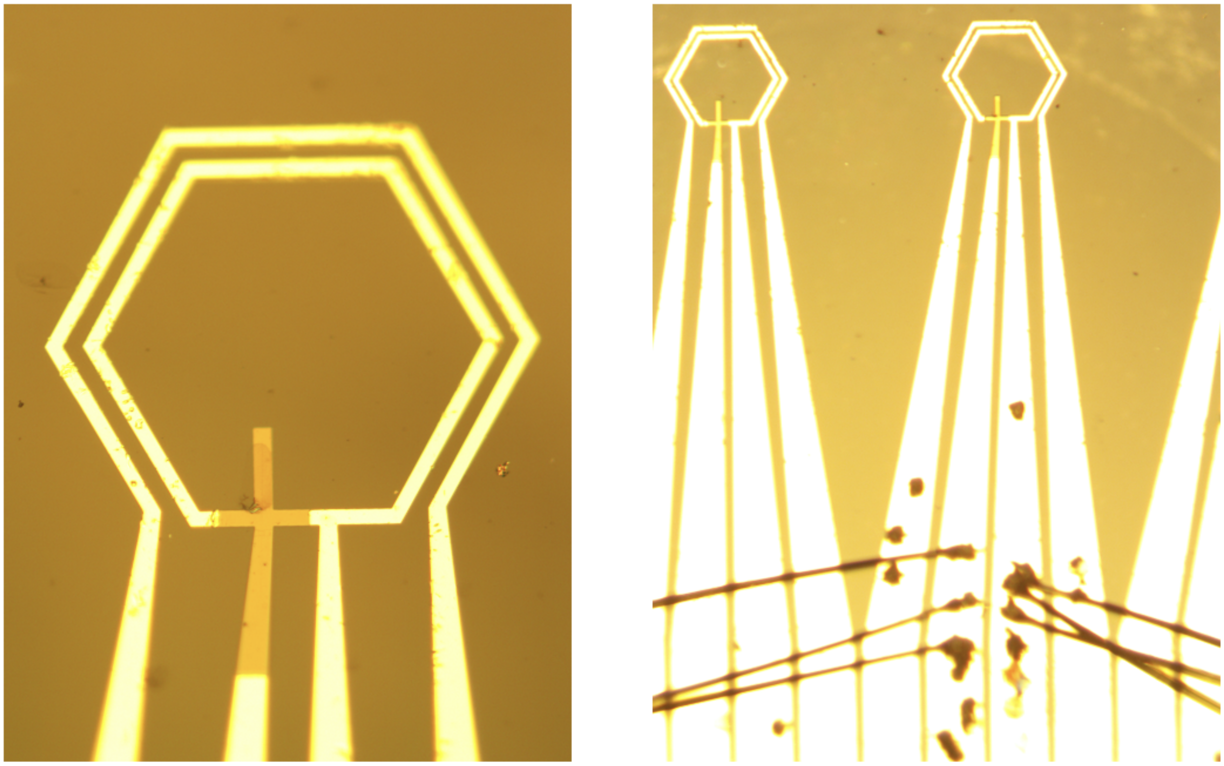

Figure 6.12: Low noise direct inject SQUID and chip design and zoom in on SQUID with flux focusing pickup loop and modulation coil.

Figure 6.13: Close up optical image of focused HeIB directly written SQUID. The faint lines are created by ion beam induced disorder and make up the Josephson Junctions, squid loop and additional lines to shorten the width of the junction.

By making the pick-up loop bigger we can get much lower flux noise but will have a proportional increase to the field noise. A larger pickup loop will make the device more sensitive, but it will also cause it loose spatial resolution. Here I keep the original hexagonal pick-up loop and direct inject squid design. I changed the orientation of the sensors so that all junctions were written along the same axis in the helium ion microscope. I slightly increased the thickness of the pickup loop wires to reduce its inductance but maintain strong coupling between pickup loop current and squid loop current. The outer radius of the pickup loop remained the same. As discussed in the SQUID theory section, the most important contribution to SQUID noise is the value of resistance of the device. Higher resistance will result in a lower noise system. For this lower noise iteration SQUID magnetometer design I aimed to make high resistance SIS Josephson junctions and minimize their width.

These slight adjustments to the large scale lithography features allowed me to optimize the sensitivity of the SQUID at lower temperatures. Previous iteration of this direct inject SQUID had a resistance of 10.3Ω. Figure 6.13 shows an IV characterization with a R_N of 20Ω. The resistance of the SQUID goes by the formula: $\frac{1}{R_N} = \frac{1}{R_{j1}} + \frac{1}{R_{j2}}$, from this I can assume that each junction has an R_N of close to 40Ω. I was able to achieve this high junction resistance by limiting their size to 200 nm and using a relatively high ion fluence to write each junction of 500 ion/nm. This doubling in resistance should make the noise characterization twice as low.

The magnetic field vs voltage characterization of this device is shown in figure 6.13. Voltage modulation of this device is approximately $100\mu V$ and has a period of oscillation of 250nT. These values are similar to the SQUID describe in the previous section at 10K.

Noise characterization of this device is shown in figure 6.14. This measurement was taken in a liquid helium dip prob system. We used two layers of mu-magnetic shielding

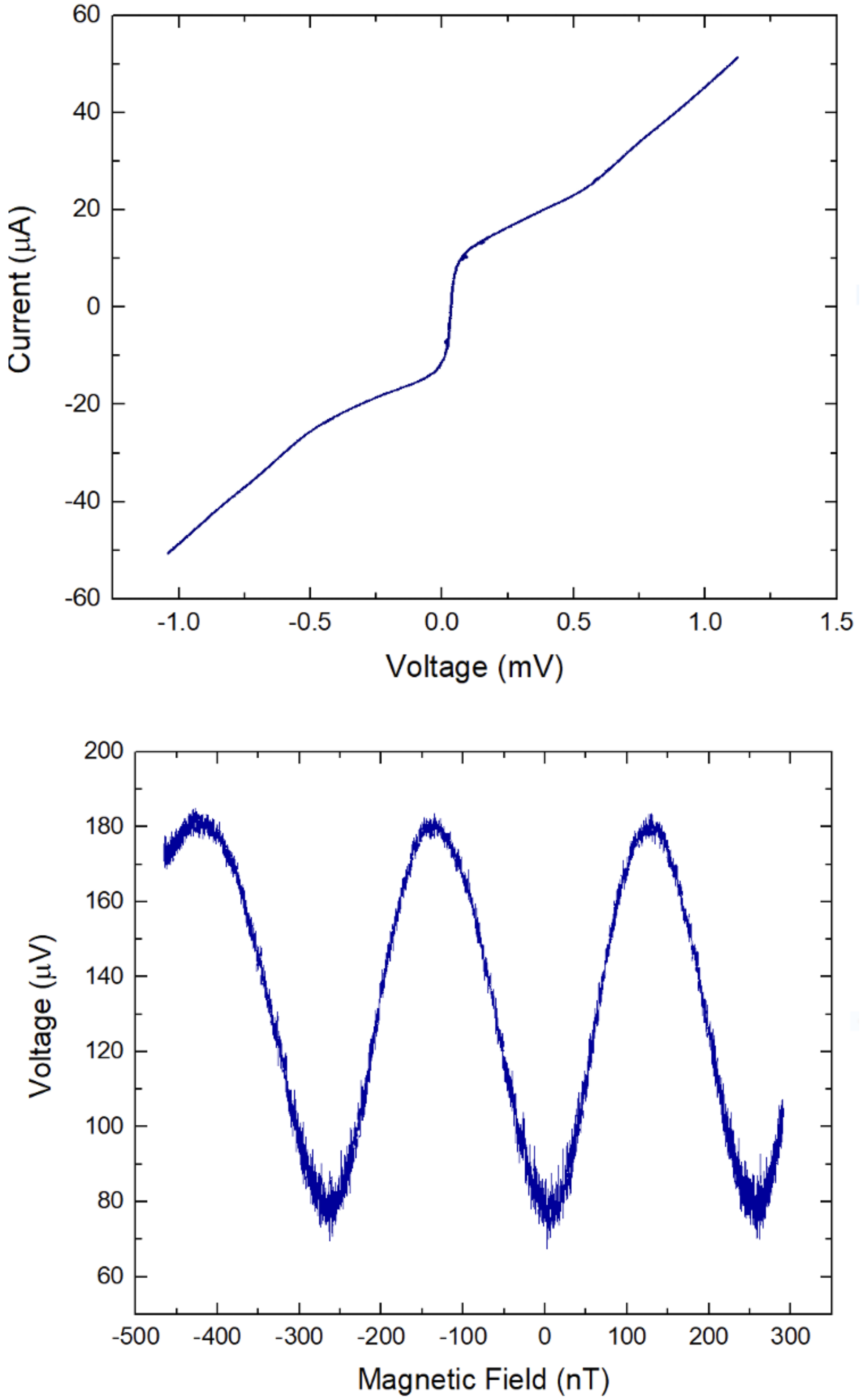

Figure 6.14: IV and VB characterizations of low noise direct inject YBCO SQUID magnetometer measured at 10K.

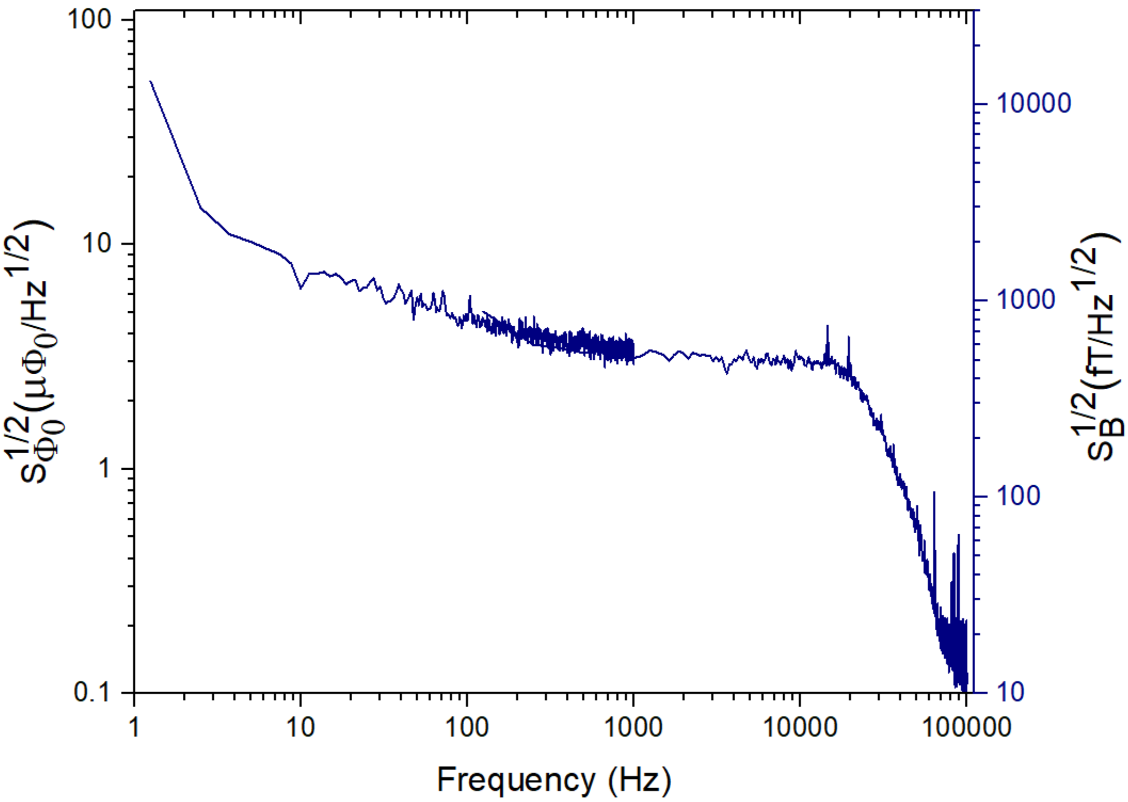

Figure 6.15: Flux and field noise characterizations preformed at 4.2K.

to protect the device from coupling to exterior noise sources. The liquid system is inherently quieter than the pulsed tube cooler system as discussed earlier. I used the on-chip modulation coil to lock the SQUID to flux locked loop exterior electronics. FLL electronics utilize bias reversal in this measurement. This SQUID has very low 1/f noise with a sharp drop to the high femto-tesla regime at 50Hz. This high resistance lower noise SQUID has a field noise level of only $540fT/\sqrt{Hz}$ and flux noise of $2\mu\Phi_0/\sqrt{Hz}$ at 1Khz. Compared with the previous device and measurement, this system has 1000 times less flux noise at 10hz. This measurement demonstrates the lowest noise YBCO SQUID system having a flux focusing loop smaller than $500\mu m$ in diameter.

6.2.3 SQUID Array

In addition to sensitive magnetometer systems, I also fabricated and characterized 2 x 2 SQUID array. This SQUID array was designed to function as part of an RF antenna. The antenna design consists of concentric semicircles starting at $1000\mu m$ in diameter down to $40\mu m$ in diameter. These semicircles are meant to increase coupling at a range of frequencies. Between the semicircles of superconducting wire is a $12\mu m$ wide bridge connecting either side. In the center of the connecting central YBCO bridge I use the focused helium ion beam to irradiate two $4\mu m$ wide squares with a high dose of helium ions: $500 ions/nm^2$. These highly radiated become so disordered that the regions are no longer superconducting and make up the SQUID holes.

Figure 6.15 shows a optical image of the 2x2 SQUID array. The bright yellow is the gold capping layer. Gold in the light brown region was removed by KI etch to revel the YBCO film underneath. The YBCO film used in this device is 35nm thick. Dark grey squares on the center YBCO bridge are a result of a large dose of helium ions. Lower dose Junctions are directly written along the thin dotted blue lines. Each junction is approximately $4\mu m$ wide.

The SQUID array has 3.2Ω of normal state resistance and a critical current of $50\mu Amps$. The IV curve plotted in Figure 6.16 was measured at 40K. A Fraunhofer pattern normally plots critical current vs magnetic field but we can also see the diffraction pattern by plotting voltage vs magnetic field. Previous VB plots are of a much smaller rage in magnetic field and show only the inner SQUID interference oscillations. By applying a

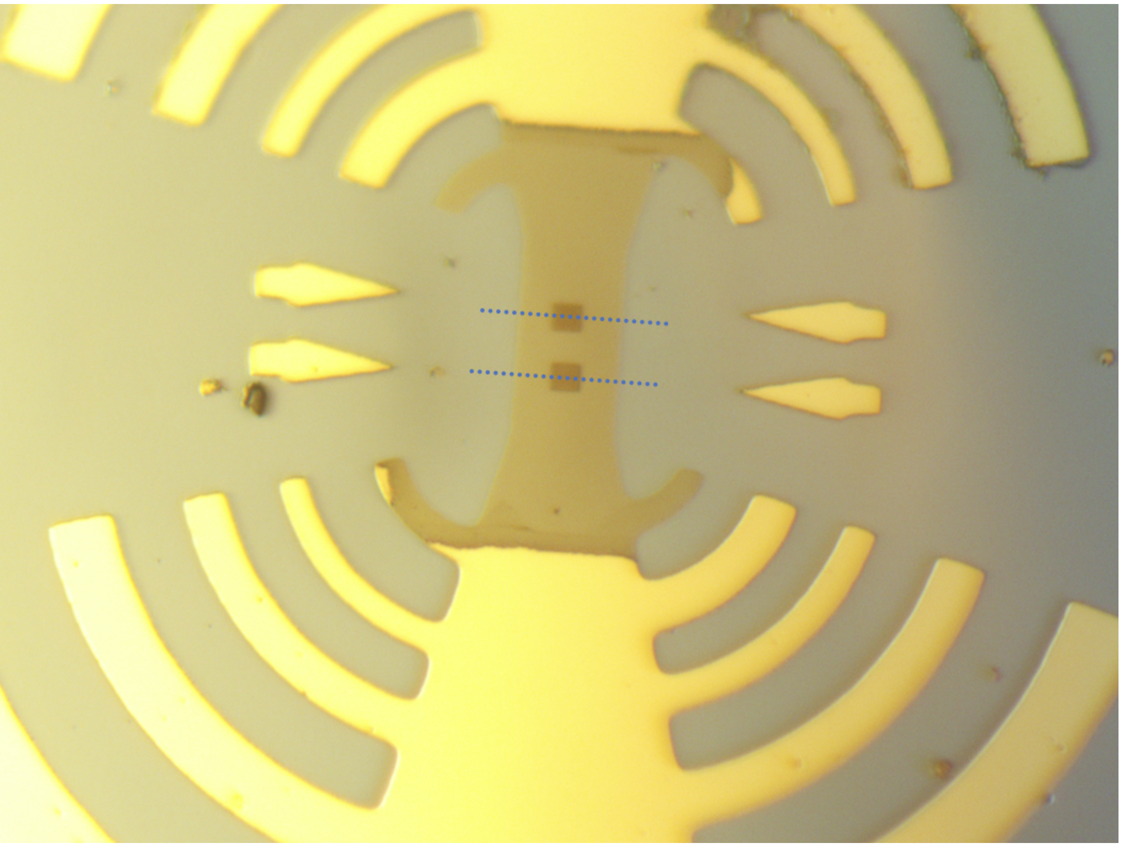

Figure 6.16: Optical image of 2x2 SQUID array set inside a circular antenna.

broad enough magnetic field sweep we can see the smaller SQUID oscillations as well as the larger diffraction pattern. Figure 6.17 shows the interference and diffraction pattern of this 2x2 squid array.

This device has a unique response to the magnetic field sweep in that the periods of the diffraction pattern is different on either side of zero. This device also has different amplitudes of SQUID oscillations on either side of zero. The asymmetry of this measurement is due to the difference in widths of the junctions that comprise the array. The non-superconducting regions making up the SQUID holes are off center of the bridge leading to

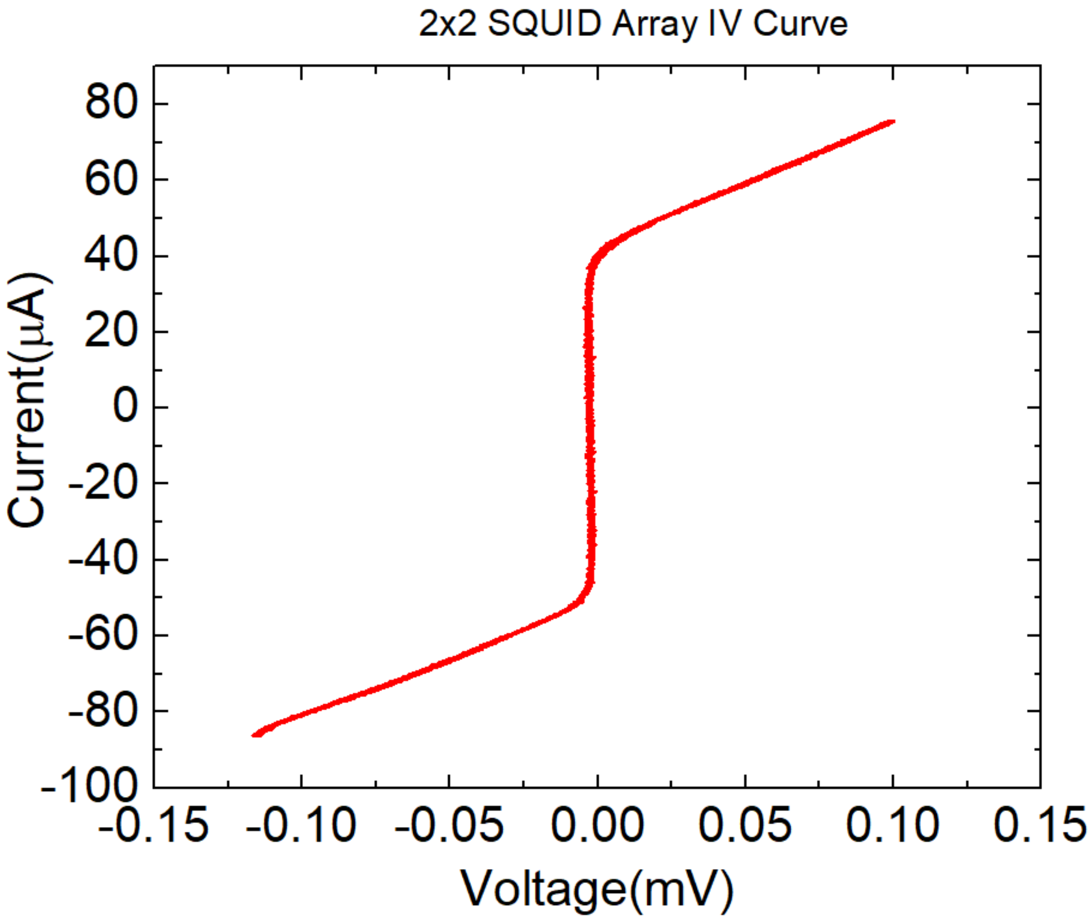

Figure 6.17: Current vs voltage characterization of 2x2 sQUID array

different width junctions on either side. The overall function of the device is a combination of performance of its individual components which in this case are not congruent.

This device was also characterized in the presence of high frequency EM radiation. Figure 6.18 shows Shapiro steps in the current voltage curve induced by an 18Ghz signal generated through an open RF line near the chip. Figure 6.6 shows a Shapiro step measurement for a single junction. one notable difference between these two AC characterizations is the comparatively non uniformity to the step height and step spacing of the measurement

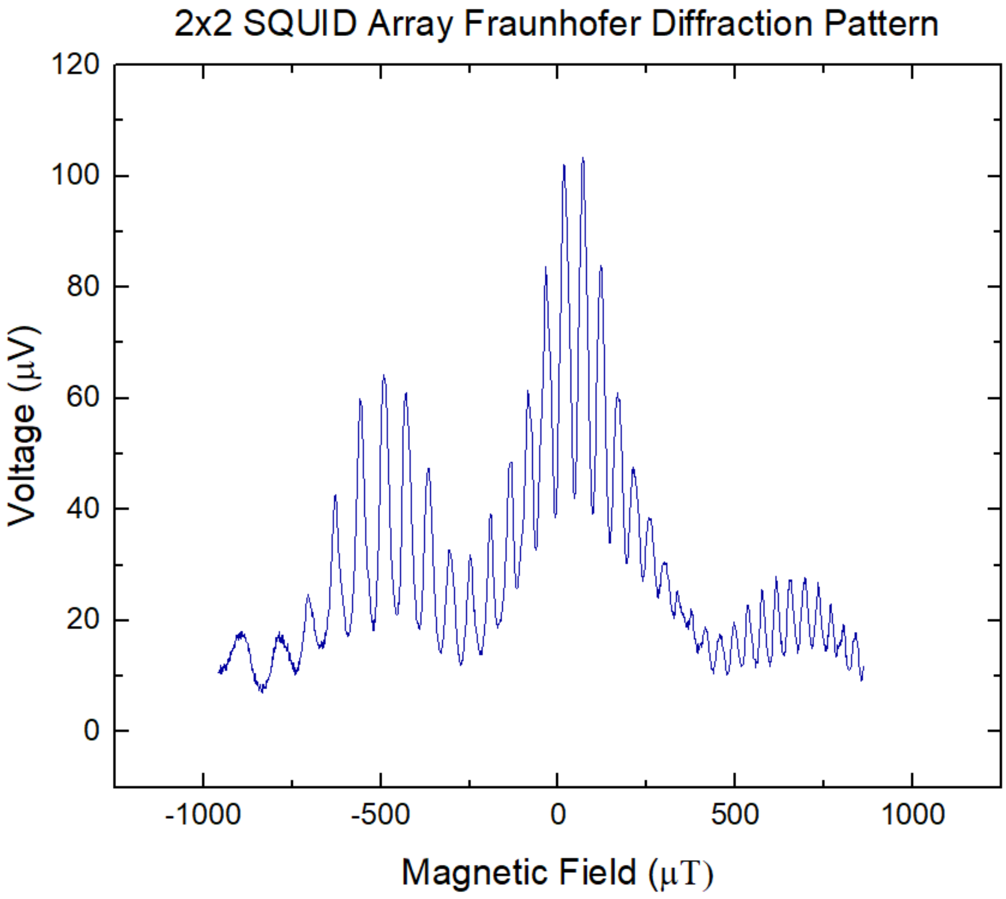

Figure 6.18: Voltage vs magnetic field response of 2x2 SQUID array.

in 2x2 SQUID array. This is again due to the asymmetry of the junctions that comprise it. However, the characterization in figure 6.18 was made at -5db which is a lower power than any of the curves produced in figure 6.6. This indicates that the antenna design is working well to amplify coupling of the applied 18Ghz signal.

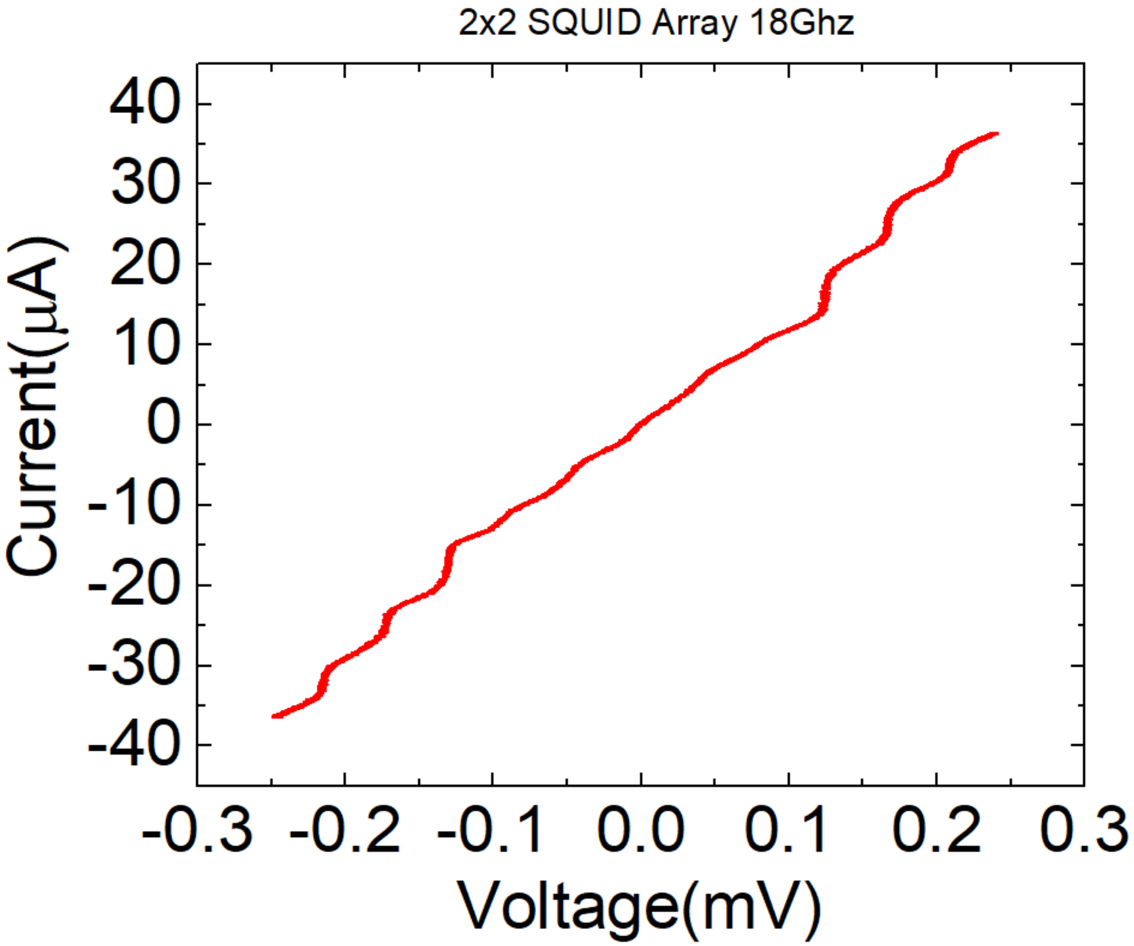

Figure 6.19: Shapiro steps observed in 2x2 SQUID array.

Chapter 7

Niobium Superconducting Devices

The vast majority of industrial and research based superconducting devices are fabricated with niobium. Niobium has a relatively high critical temperature of 9.2K and can be easily grown into thin uniform films with very few defects. Traditionally fabricated Niobium Josephson junctions consist of 4 to 6 layers of materials and must undergo several time consuming lithography processes. In this chapter I will show the capabilities and devices I developed using focused helium ion beam fabrication by milling and induced disorder of Niobium films. This method enables faster time from designing a device to fabrication and testing and allows us to create features as small as 20nm in diameter. These are the first Niobium Josephson junctions made using this technique. Although, this method of fabricating Niobium superconducting devices is unlikely to replace the state of the art lithographic techniques for junction fabrication, HeIM fabricated of Niobium devices can be usefully integrated in existing systems providing many advantages.

7.1 Milling of Niobium with HeIM

Niobium is significantly more conductive and has much fewer grain boundaries compared with YBCO. Niobium films have a very smooth and hard surface making them easy to work with. As discussed earlier, Niobium is less sensitive than YBCO to induced disorder through ion radiation.

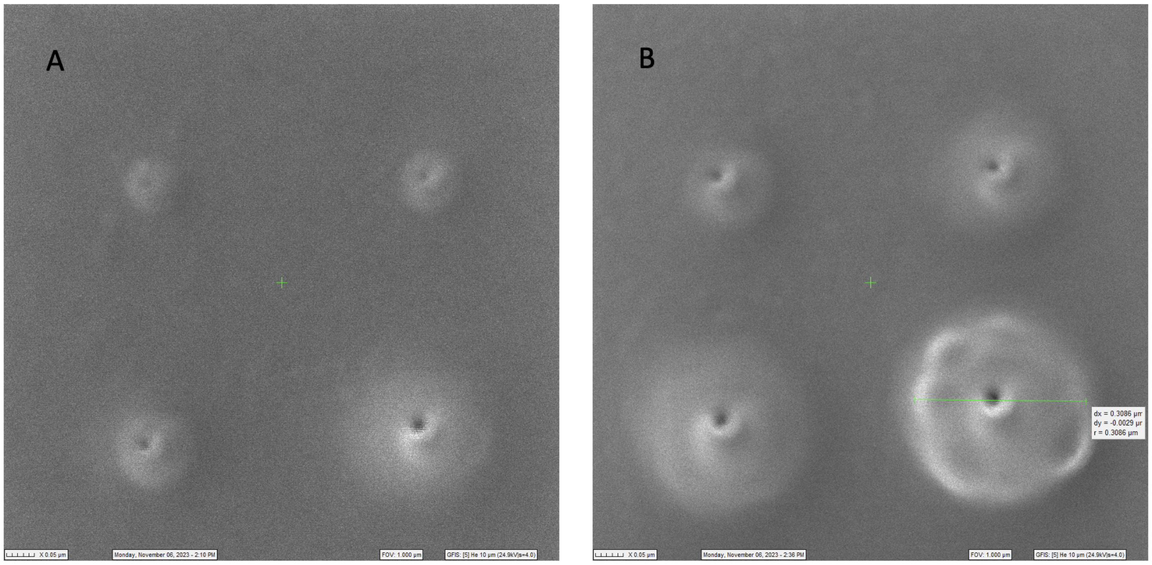

Figure 7.1: HeIM images of holes milled by prolonged Helium ion beam exposure. Both images have field of view of $1\mu m$

Figure 7.1 shows the effects of prolonged exposure of 25kV helium ion beam on Niobium. Figure 7.1.A has doses: $5 \times 10^8 ions$, $1 \times 10^9 ions$, $2 \times 10^9 ions$ and $6 \times 10^9 ions$. Figure 7.1.B has doses: $2 \times 10^9 ions$, $5 \times 10^9 ions$, $9 \times 10^9 ions$ and $1.2 \times 10^1 0ions$. By increasing the current and letting the Helium ion bean remain in one location I can mill and sputter the Niobium film. This niobium film is 35nm thick with a Si/SiO_2 substrate. As the dosage increases the size of the hole increases reaching a maximum diameter of 70nm.

The light colored area around the milled hole is a result of charging of the material and the sputtering and re-depostion of the Niobium. The hole in the top left of figure 7.1.A is written with a dose of $2 \times 10^9 ions$ resulting in a hole of 20nm in diameter. Drilling holes like this can be use full in creating vias making extremely small connection between layers of material. These hole can also be useful when trying to trap magnetic flux vortexes to make a Niobium film with higher J_C.

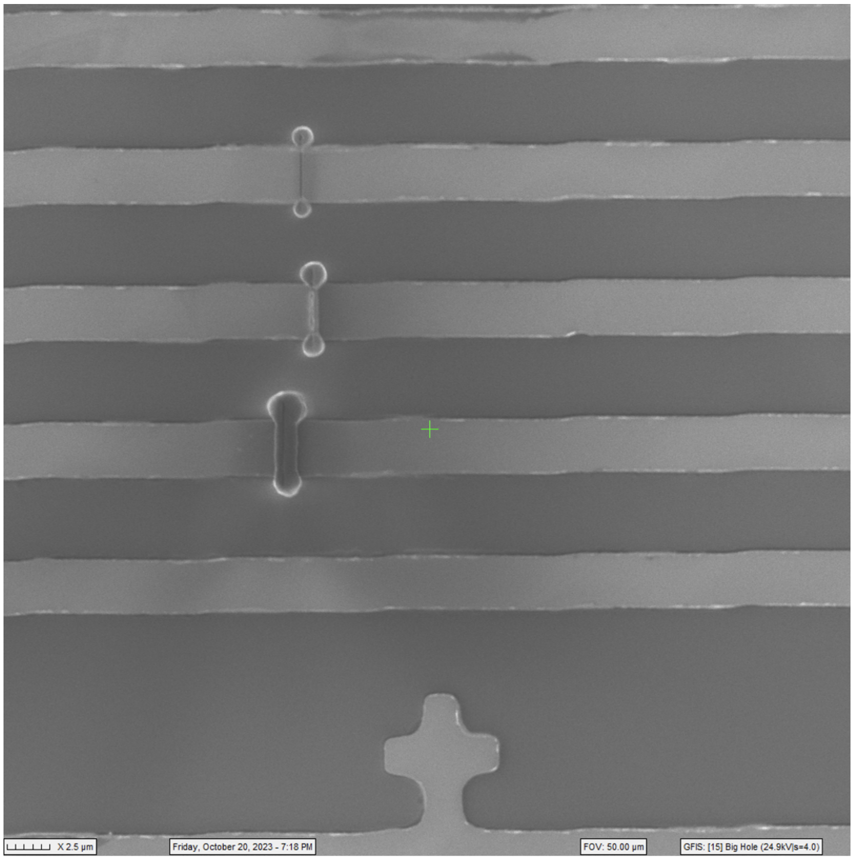

Figure 7.2: HeIM images of high dose lines written with HeIM. Ion radiation causes sputtering the Niobium film breaking the wires and creating an open circuit.

In addition to milling holes in the film I tested the capabilities of this technique for nano-scale direct edit of electrical circuits. The field of view of figure 7.2 is $50\mu m$. The

Darker grey is the Si/SiO_2 substrate while the light grey bars are $3.2\mu m$ wide 35nm thick Niobium wires. From top to bottom the radiated lines in the image are written with doses: $50M\ ion/nm$, $100M\ ion/nm$ and $500M\ ion/nm$. Each line has bright bulbous features on either end of the cut. These bright bulbous features are sputtered and redeposited Niobium landing at either end of the space the beam was rastered across. The top line written with $50M\ ion/nm$ had a $\approx 20\Omega$ of resistance at 1.6K, while the other two lines were found to be open circuits. This demonstrates the ability to cut 35nm deep trenches with a dose of $100M\ ion/nm$. Helium ion microscopy provides the ability to 'gently' image a material without creating any significant disorder or sputtering of material and enables us, with sufficiently high fluence of ions, to make cuts in Niobium films.

7.2 FHeIB Niobium Josephson Junctions

As superconducting integrated circuit designs for quantum computing and digital logic grow in complexity, it is necessary to continue to scale down the size of individual devices while maintaining RF response and access to a large I_c and R_n parameter space. In order to meet the growing challenges of superconducting computing and sensing systems I developed a new technique to fabricate Niobium Josephson junctions using helium ion beam radiation. Using a Helium ion beam to directly write in-plane Josephson junctions on niobium films yields several advantages over traditional techniques and has the potential to complement existing Josephson devices in a wide range of superconducting integrated circuit designs. In this section I will discuss the methods of fabrication as well as the electrical characterizations of this new type of Niobium Josephson junction.

The use of Ion beam technology to disorder superconducting materials for the fabrication of superconducting devices has been extensively studied over the last decade particularly in complex high T_C materials. However, in niobium films, only weak link Dayum bridge type Josephson junctions have been successfully fabricated. These Dayum bridge junctions are made by milling the superconducting wire in a small region to a width of under 300nm. Our technique of induced disorder using helium ion beam radiation and allows us to create in plane devices as small as 40nm wide and without effecting the chemistry of the film. Using this method of niobium Josephson junction fabrication we can produce Josephson junctions with giant flat Shapiro steps and fine tune I_c and R_n characteristics.

The junctions can be written with radiation fluences ranging from 50 thousand to 15 million ions/nm allowing for variance in I_c and R_n. The landing energy of He^+ beam is 25KeV and the current is varied from 0.3 to 120 pico amps. Each junction ranges in thickness from 40nm to 100nm as the width increases with dose of He^+ radiation. This process has minimal sputtering and no chemical reaction between the implanted helium atoms and the niobium film. Using this process, each junction takes 0.5 to 30 seconds to write depending on dose and beam current. This could be greatly sped up using a broad beam source with higher current and landing energy and precision masking.

Figure 7.3 shows a Helium ion microscope image of 4 Josephson junctions written with a range of doses from 100K ions/nm to 10M ions/nm. The field of view of this image is $80\mu m$. The inset on the bottom left of this figure show the full chip design having dimensions of 5mm x 5mm. This is the same chip design as in figure 7.2. Again we can clearly see how the width of the line increases with the dose it was written at. It is important to note

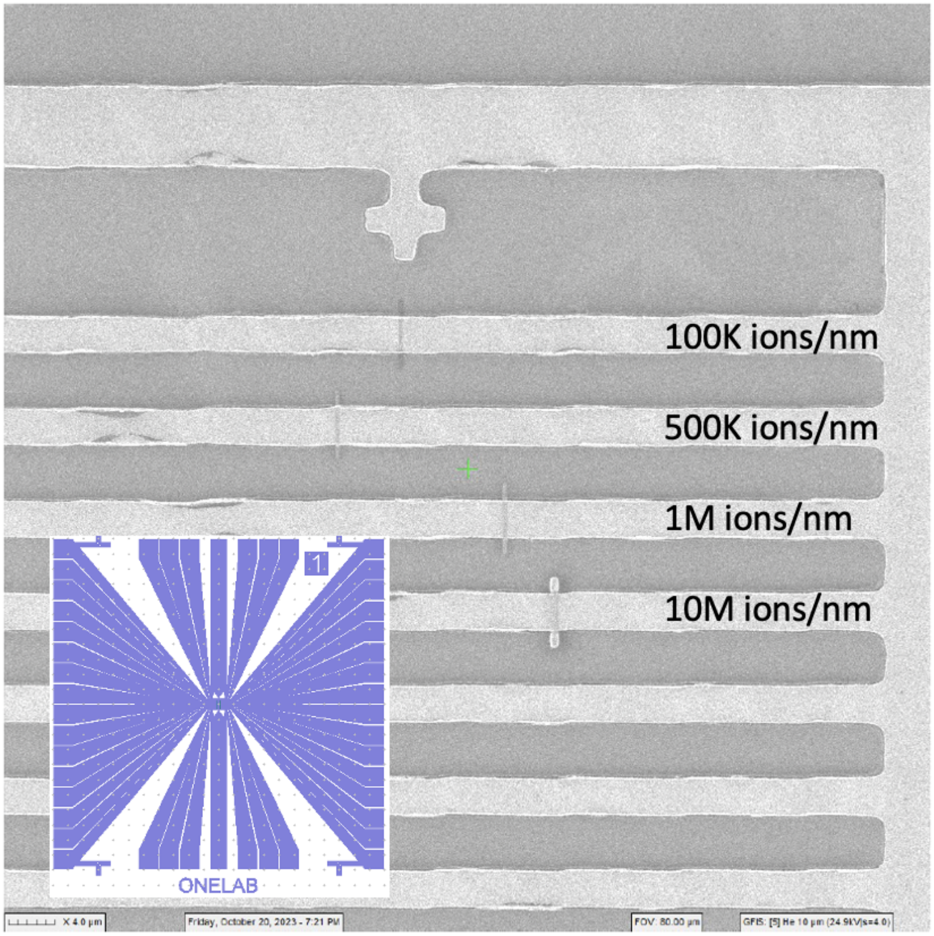

Figure 7.3: HeIM images of Josephson junctions.

that such high doses can take much longer to write than the typical doses used to disorder YBCO. Having long write times can cause issues due to beam and stage drift or beam current fluctuations. The drift of the beam will widen the junction creating a less defined barrier. The current fluctuations are unavoidable but get worse over time as dose and write time are determined by a prior current measurement. To cut down on excessively long write times it is necessary to increase the beam current by using a larger aperture and increasing the Helium gas pressure at the tungsten tip microscope gun. However, using too large of an aperture will result in a much larger spot size and much wider junctions. These junctions were written using a $10 \mu m$ diameter aperture and a current of around 3 picoamps.

7.2.1 Current - Voltage Characterizations

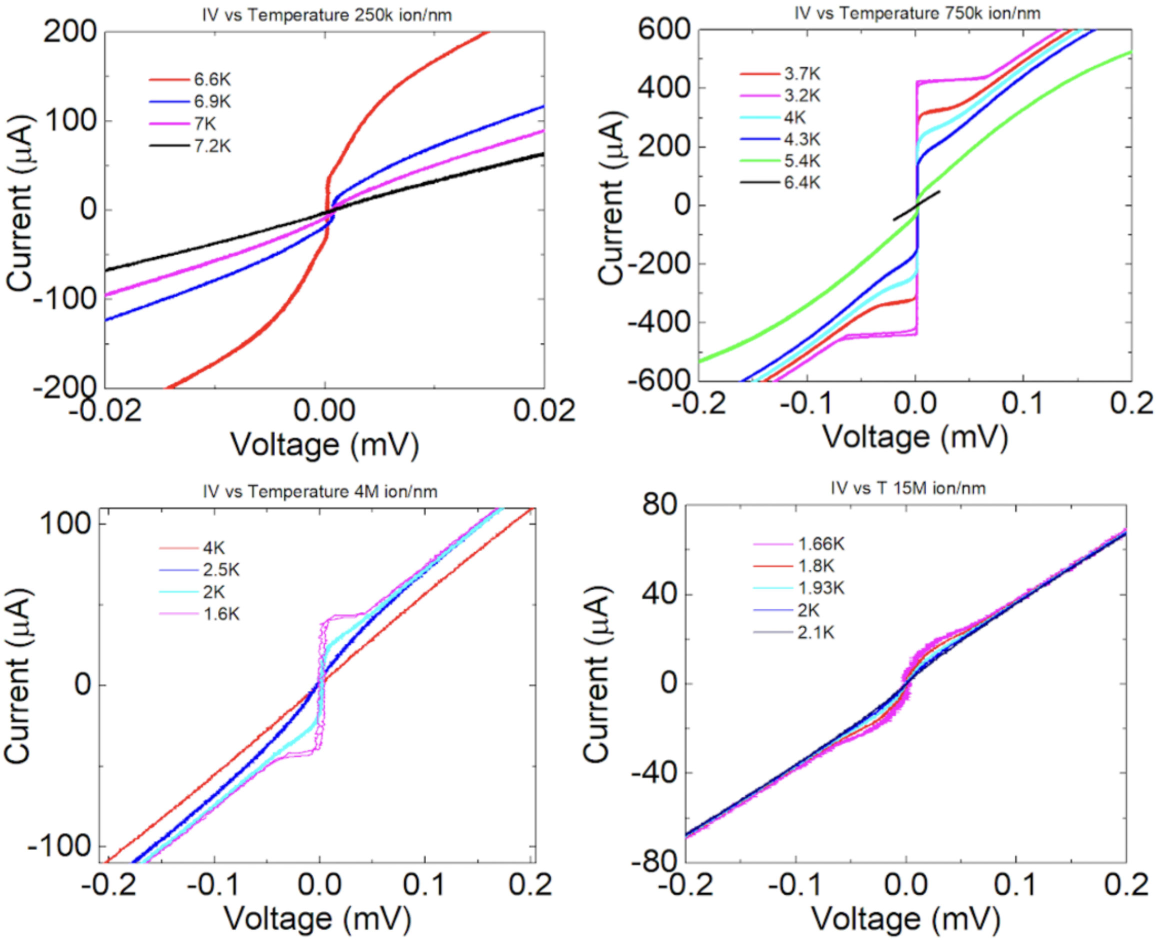

Figure 7.4: IV curves of HeIM fabricated Niobium Josephson junctions. Doses range from 250K ion/nm to 15M ion/nm.

Figure 7.4 shows IV curves at different temperatures for junctions written at 4 ion doses: 250K, 750K, 4M and 15M ions/nm. The dose of ion radiation has a drastic effect on the shape and I_C and R_N characteristics of the IV curves. Each of the different doses also has a different ideal operating temperature range. All of devices are SNS type junctions.

The junction written at 250K ion/nm has a resistance of less than 0.1Ω at 6.6K and decreases rapidly with as the temperature drops. As temperature goes down the junction rapidly becomes a weak link as the two superconducting regions become strongly coupled. This leads to a significant increase in critical current through the junction. Most of the supercurrent in this device is due to quasi particle tunneling and not Josephson tunneling.

The junction written at 750 ions/nm has a wide operating temperature range and a normal state resistance of 0.45Ω which does not decrease below 5K. The disorder at this dose is sufficient to create a stronger and a more well-defined barrier resulting in a flat region to the IV indicative of Josephson tunneling and the opening of the superconducting energy gap. The I_C continues to increase as temperature goes down reaching $400\mu A$ at 3.7K. Unlike the IV curved in figure 3.2 where there are zero states between I_C and the turn on voltage, this data show a sparse but continuous flat line of points connecting the peak of the critical current and the start of the ohmic portion of the graph.

The junction written with 4M ions/nm remains restive below T_C until it begins to be nonlinear just above 2K. This device has much lower turn on temperature than the last two and has a significantly smaller operating temperature range and critical current. However, the R_N of this junction is 2.6Ω at 1.6K significantly higher than the previous devices.

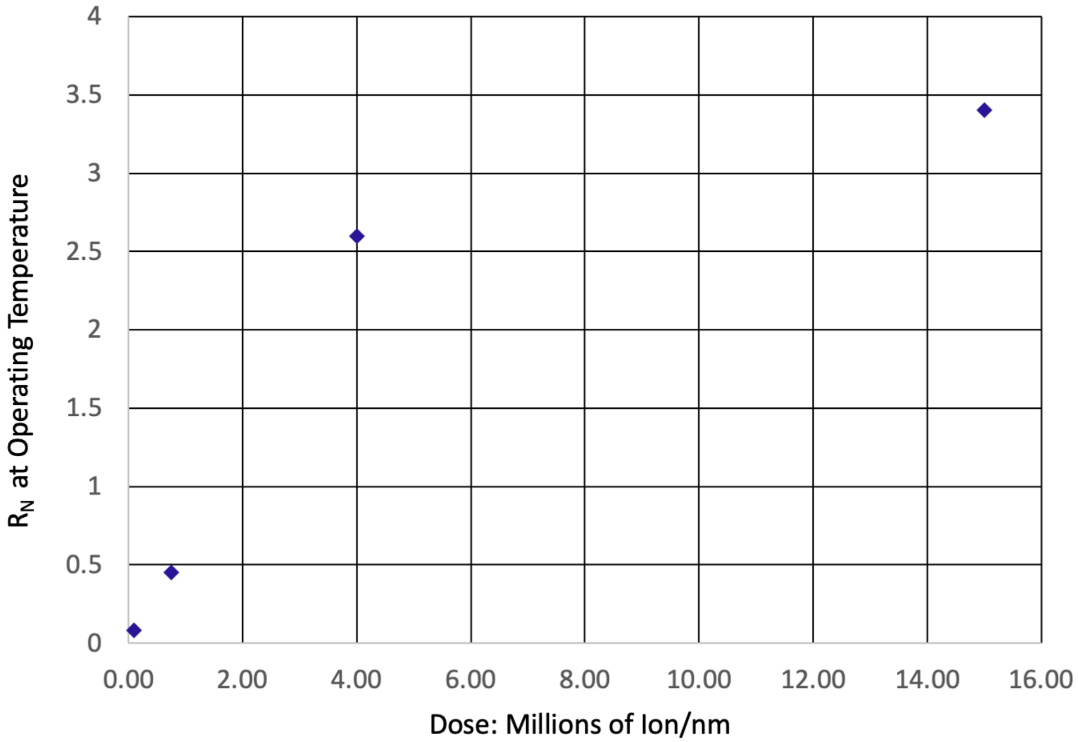

Figure 7.5: Graph showing the effect of the junction dose on R_N .

The junction written with 15M ion/nm begins to have nonlinear characteristics below 1.9K. Our pulsed tube cooler does not get cold enough to characterize this device below 1.6K though already we can tell the normal state resistance is 3.4Ω and is remaining constant. We can expect the critical current to straighten out like the other devices at lower temperatures. The coherence length of Niobium is only 40nm while this junction is more than 100nm thick making the superconducting regions significantly less coupled than the other devices.

Figure 7.5 plots the relation between the dose a junction is written with and its normal state resistance in its operating temperature regime. There is a nearly linear relation between junctions written at 100K ions/nm up to 4M ions/nm. However, we see decrease in the added resistance above 4M ions/nm. This is indicative of a maximum amount of change to electrical structure due to bringing the material closer and closer to being fully amorphous. There is a threshold at which added disorder will not change the resistance of the film. Continuing to increase the dose will only result in milling of the material as demonstrated above.

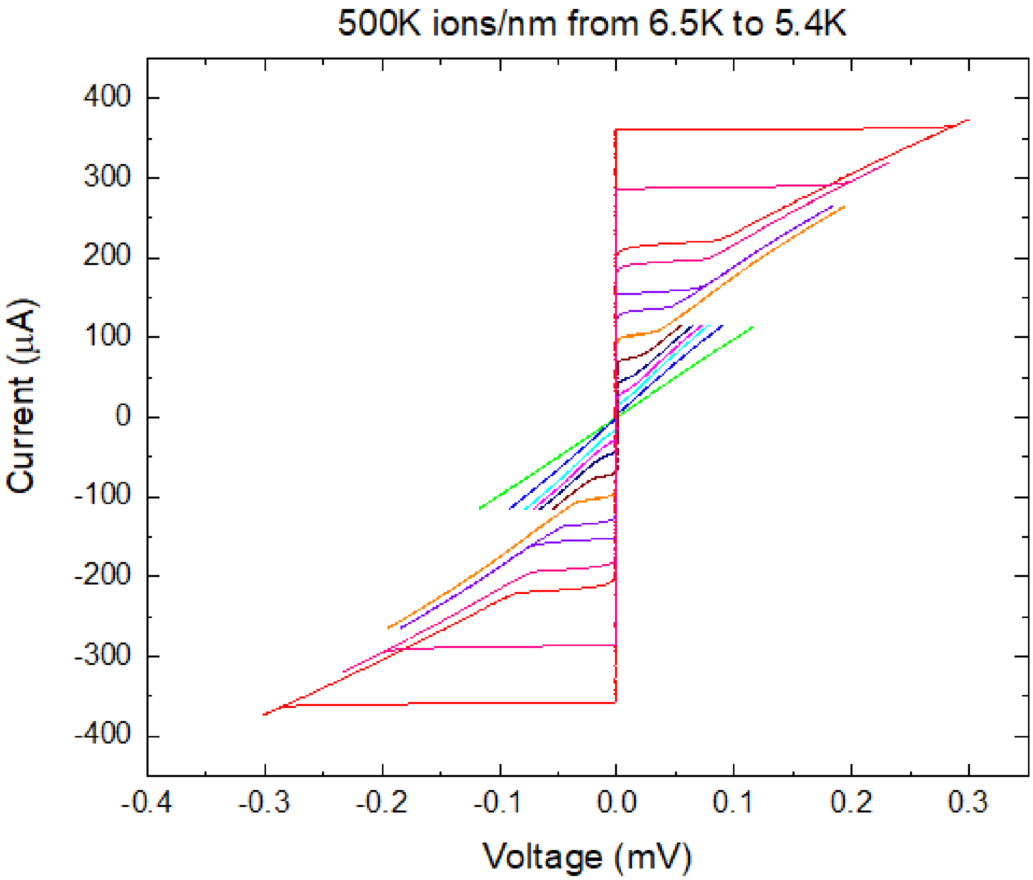

Figure 7.6: Current vs Voltage curves for junction written with dose of 500k ions/nm

Figure 7.6 depicts IV curves measured at temperatures ranging between 6.5K to 5.4K. This junction becomes increasingly hysteric as temperature decreases. The hysteresis is a result of the decrease in the $\mathcal{B}_C$ parameter.

$$\mathcal{B}_C = \frac{2\pi I_C R^2 C}{\Phi_0} \tag{7.1}$$

For values of $\mathcal{B}_C$ much less than 1 the junction is in a strongly damped regime with no hysteresis. For values of $\mathcal{B}_C$ above 1 the hysteresis window begins to open. Unlike the YBCO junctions, these Niobium films have no intrinsic shunt resistance preventing the hysteresis. As the critical current and capacitance rise with decreasing temperature this Niobium junctions becomes weakly damped developing an increasingly large hysteresis window. Without knowing the exact capacitance of the junction we can estimate $\mathcal{B}_C$ for a given IV curve using he formula:

$$\frac{I_L}{I_C} \approx \frac{4}{\pi\sqrt{\mathcal{B}_C}} \tag{7.2}$$

where I_L is the lower state critical current at the start of the hysteresis window and I_C is the upper critical current at the high return to the zero voltage state. From this equation I approximate $\mathcal{B}_C$ to be 4.75 for the lowest temperature IV curve. Plugging value back into equations 7.1 I find the capacitance of this junction to be $\approx 4.2pF$.

7.2.2 Magnetic Field Effects

The most compelling proof demonstrating the existence of a Josephson junction is its response to an external magnetic field. In figure 7.7 the Fraunhofer pattern is plotted

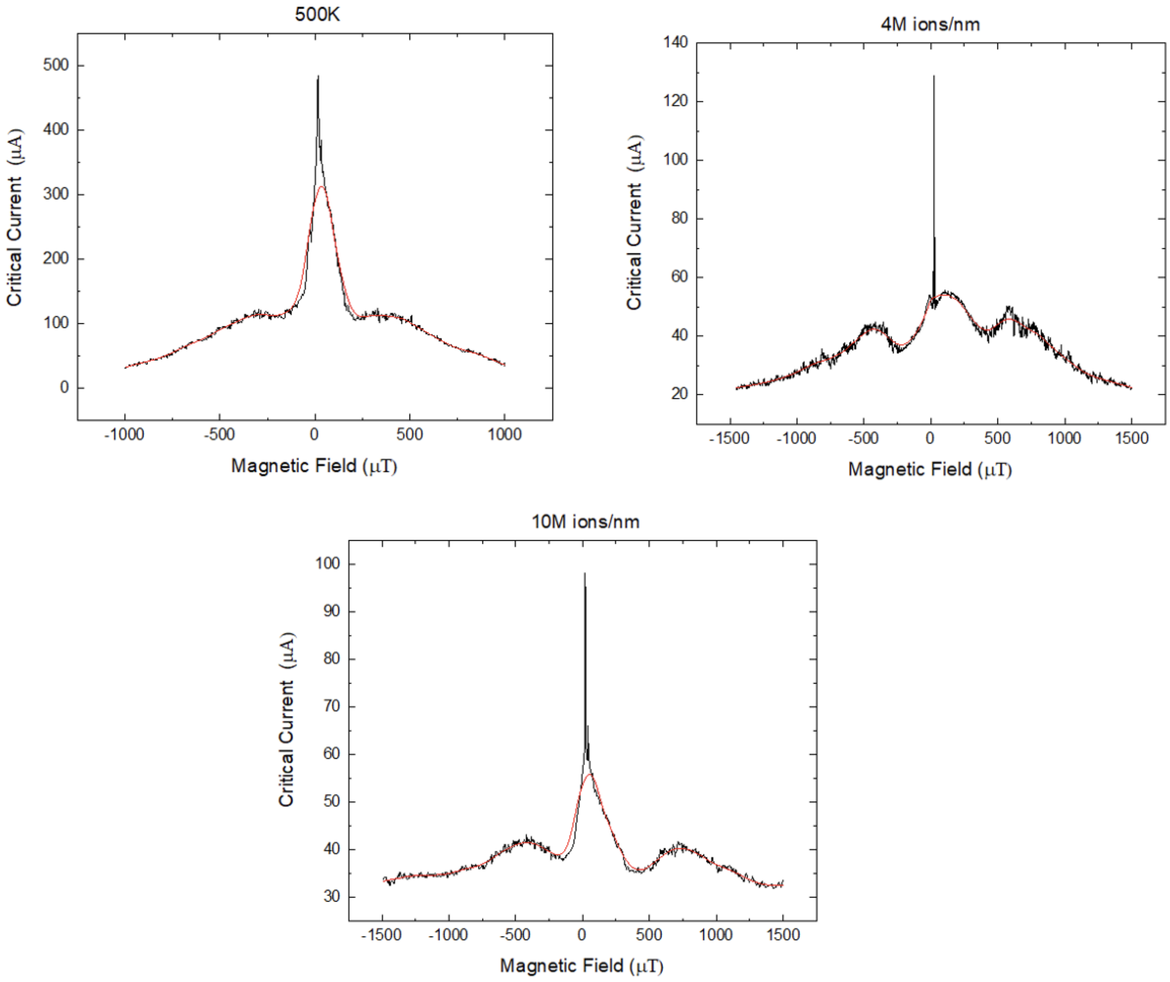

Figure 7.7: Fraunhofer pattern for Niobium junctions of dose 500K, 4M and 10M ions/nm.

for junctions of dose 500K, 4M and 10M ions/nm. As the dose increases the depth of the first minimum in the Fraunhofer pattern grows relative to the maximum critical current. The junction written with 500K ions/nm was measured at 5.6K and has significant excess current demonstrated by the much smaller response to magnetic field. In all the graphs in figure 7.7, as the applied magnetic field increases past $1000\mu T$ we see the critical current fade towards zero. The Fraunhofer pattern dose not 'ring out' like typical Niobium junctions because the walls of the non-superconducting barrier region are not well defied creating a dampening effect to the standing waves in the Josephson cavity. All these graphs are shifted slightly off zero. This is due to the massive inductance of the superconducting magnet used to generate the field.

Rosenthal etal. 1991 derived the formula for the period of magnetic field response in the the Fraunhofer pattern for thin films with planar junctions to be:

$$\Delta B = \frac{1.84\Phi_0}{w^2}. \tag{7.3}$$

These niobium wires that the junctions are written on are $3.1\mu m$ wide. Using equation 7.3 we get a delta approximately $400\mu T$ which is only slightly smaller than the period in the Fraunhofer patterns graphed above. This mismatch is likely due to the penetration depth near the damaged areas decreasing the actual width of junction that the magnetic field will see.

7.2.3 AC Effects

Demonstrating the AC Josephson effects is another common proof of the existence of a Josephson junction. Figure 7.8 shows data for 4 different junctions. written with doses 100K, 500k, 1M and 10M ions/nm. The applied radiation for each of these devices was slightly different. Plotted in each figure are many IV curves each measured at a different power showing the power dependence of the IV curve and height of the Shapiro steps. The steps in all these graphs are perfectly evenly space and exactly follow the equation:

$$V_n = \frac{nhf}{2e} \tag{7.4}$$

where n is the nth Shapiro step and f is the applied AC frequency. Although all these junctions have different critical currents and normal state resistance the frequency at which these steps occur is only dependent on the applied frequency. This show how perfectly these type of junctions can be used as frequency to voltage transducers.

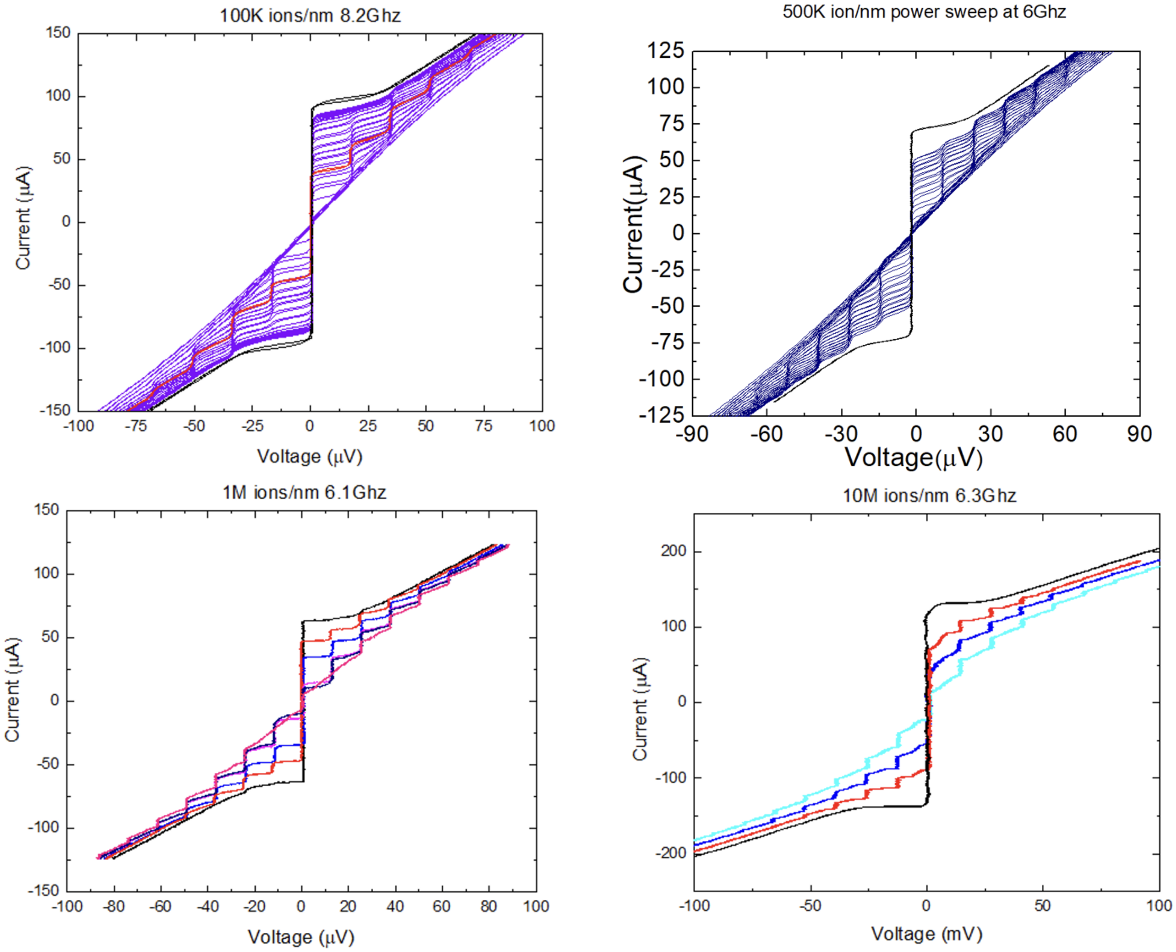

Figure 7.8: Niobium junction Shapiro steps characterization for Nb Josephson junctions written with four different doses.

To further analyze the characteristics of the AC Josephson effect, I precesely measured the relation between applied AC power and the step height. Figure 7.9.A is from the 1M ions/nm junction of figure 7.8 while 7.9.B is from the 500k ions/nm junction of figure 7.8. as AC power is increased the n=0, critical current decreases while the n=1,2,3 steps begin to increase in height. These data show the Bessel function response of step height with microwave power predicted by Shapiro and described in chapter 3.

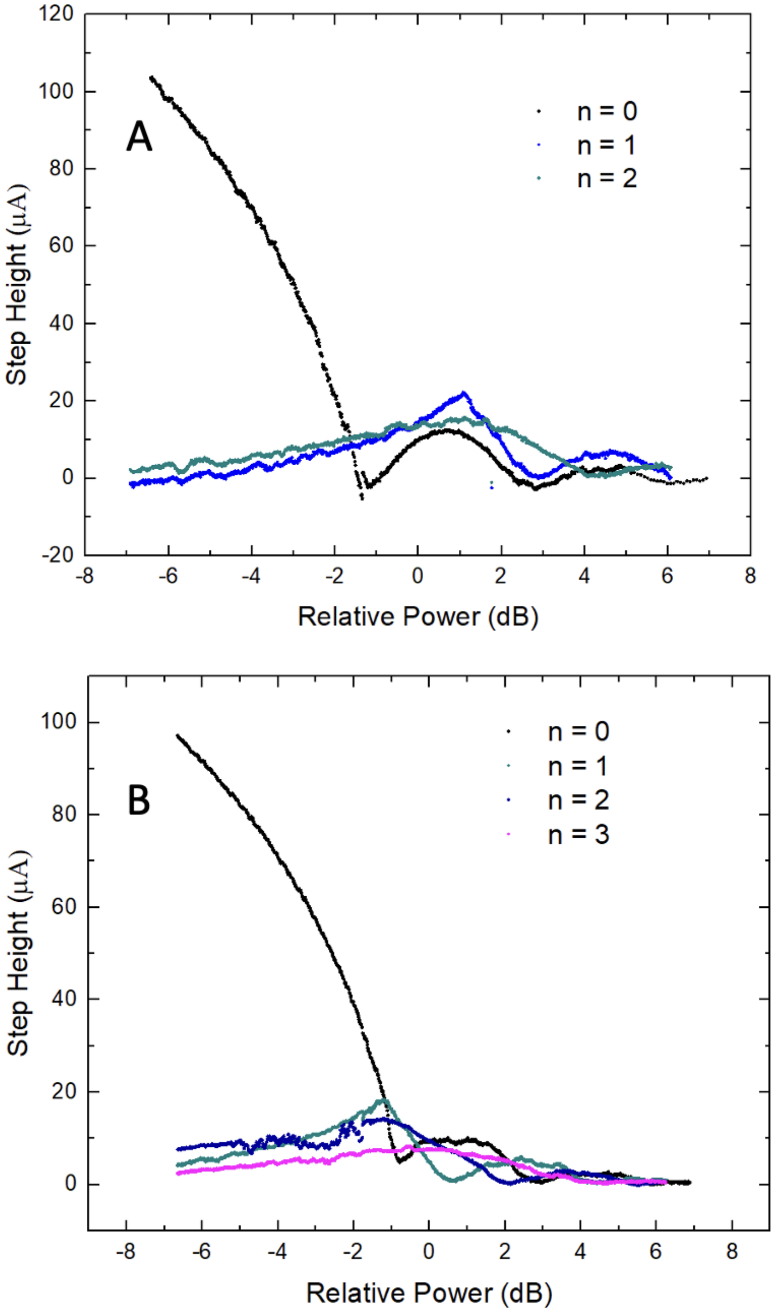

Figure 7.9: Niobium junction AC Power and step height relation.

7.3 Niobium Josephson Arrays

Superconducting electronics often rely on Josephson junction arrays that provide high power nonlinear response at relatively high voltage. Josephson junction and junction arrays' ability to act as frequency to voltage transducers have seen applications in quantum amplifiers, arbitrary Josephson waveform generators, single photon detectors, as well as defining the Voltage standard. These arrays often require hundreds to tens of thousands of junctions to preform as a lumped element with the many junctions that make them having identical characteristics in I_c and R_n. Lumped element arrays can have strong impact as an integrated component in quantum computing and superconducting digital systems.

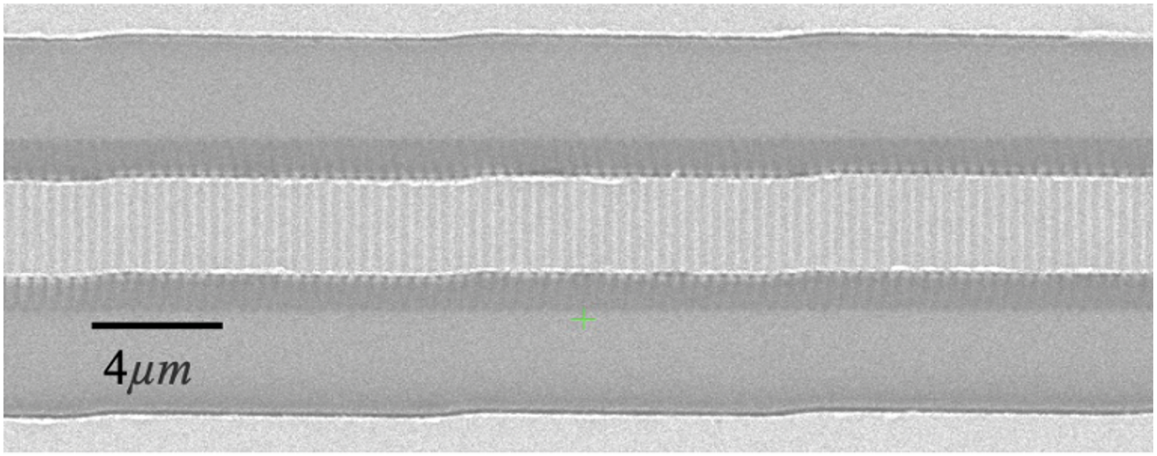

Figure 7.10: Niobium junction Array with 250nm spacing of junctions written with 250k ions/nm dose.

I fabricated and preformed tests on series arrays of Josephson junctions. Figure 7.10 shows a HeIM image of a typical junction array. In this array, junctions are written with a dose of 250k ions/nm and have spacing of 250nm. In order to learn how to best fabricate a well functioning array I characterized arrays written with the same number of junctions but varied the spacing of the junctions.

Resistivity Vs temperature is graphed in figure 7.11 for arrays with 50 junctions in them. The spacing between junctions is varied from 1200nm to 100nm. The top graph is for arrays with junctions written at 100k ions/nm while the bottom graph is for arrays written at 5M ions/nm. In both graphs the temperature range over which the junctions provide some resistance after the surrounding wire has gone superconducting is extended as the array spacing is decreased. As well the starting resistance is larger for arras with close spacing. The closely spaced arrays with junctions only 100nm appart have by far the most resistance however in further testing I found the disorder begins to overlap and the devices written with this close of spacing do not couple well to AC radiation. Junctions written with wider spacing's of 600nm and above had much less added resistance per added Josephson junction showing that spacing's above this will not have ideal coupling between each element.

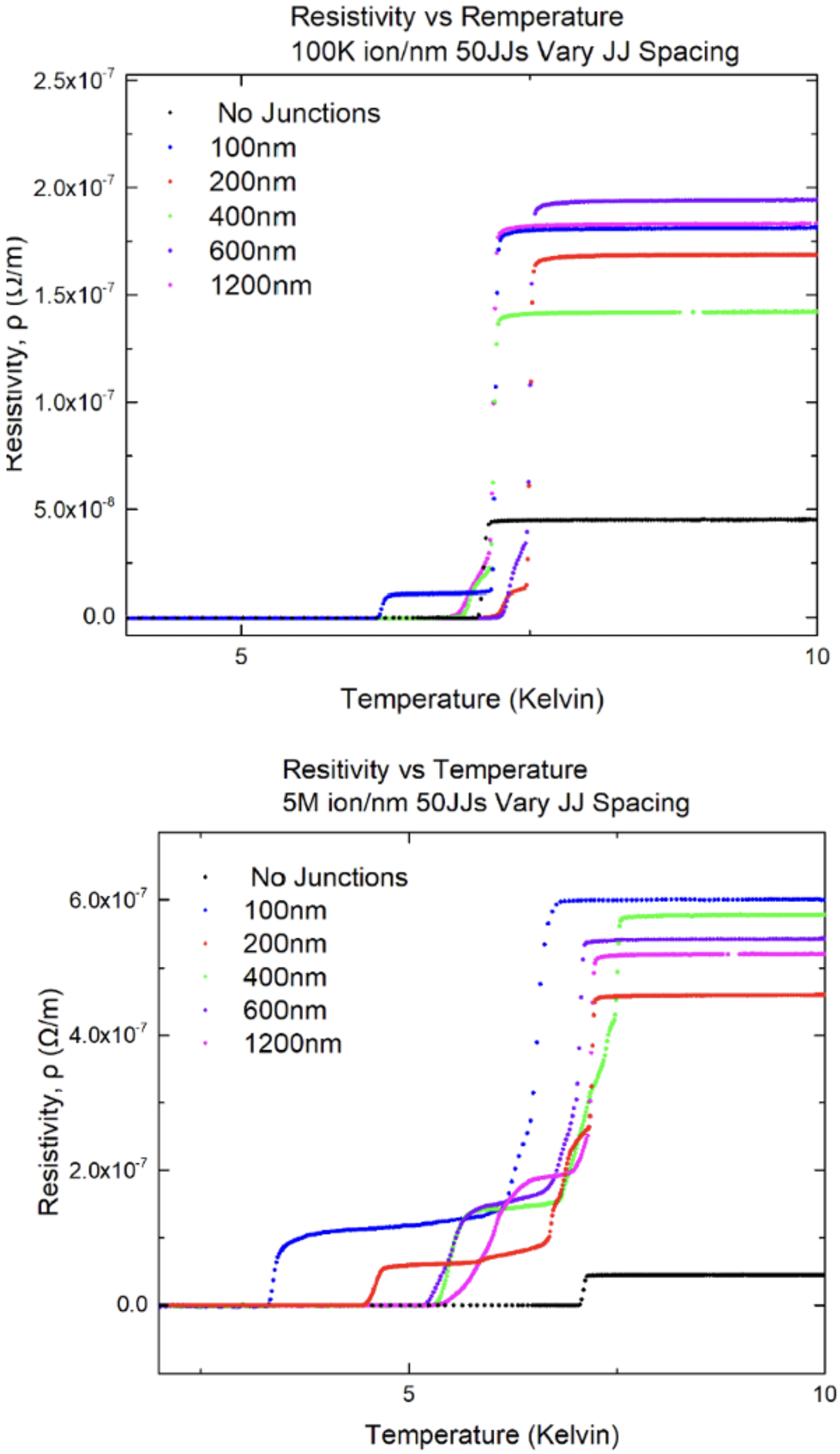

Figure 7.11: Niobium junction Array resistance vs temperature characterization with varied junction spacing.

I next characterized the Josephson arrays by varying the number of junctions that make them up while keeping the spacing constant. I chose 250nm spacing as it allowed for strong response to applied Ghz radiation while adding the junction resistance at a strong consistent rate. This measurement is shown in figure 7.12 as a current vs voltage measurement. Here we see that the I_C of these devices stays the same while the R_N increases as the number of junctions increases.

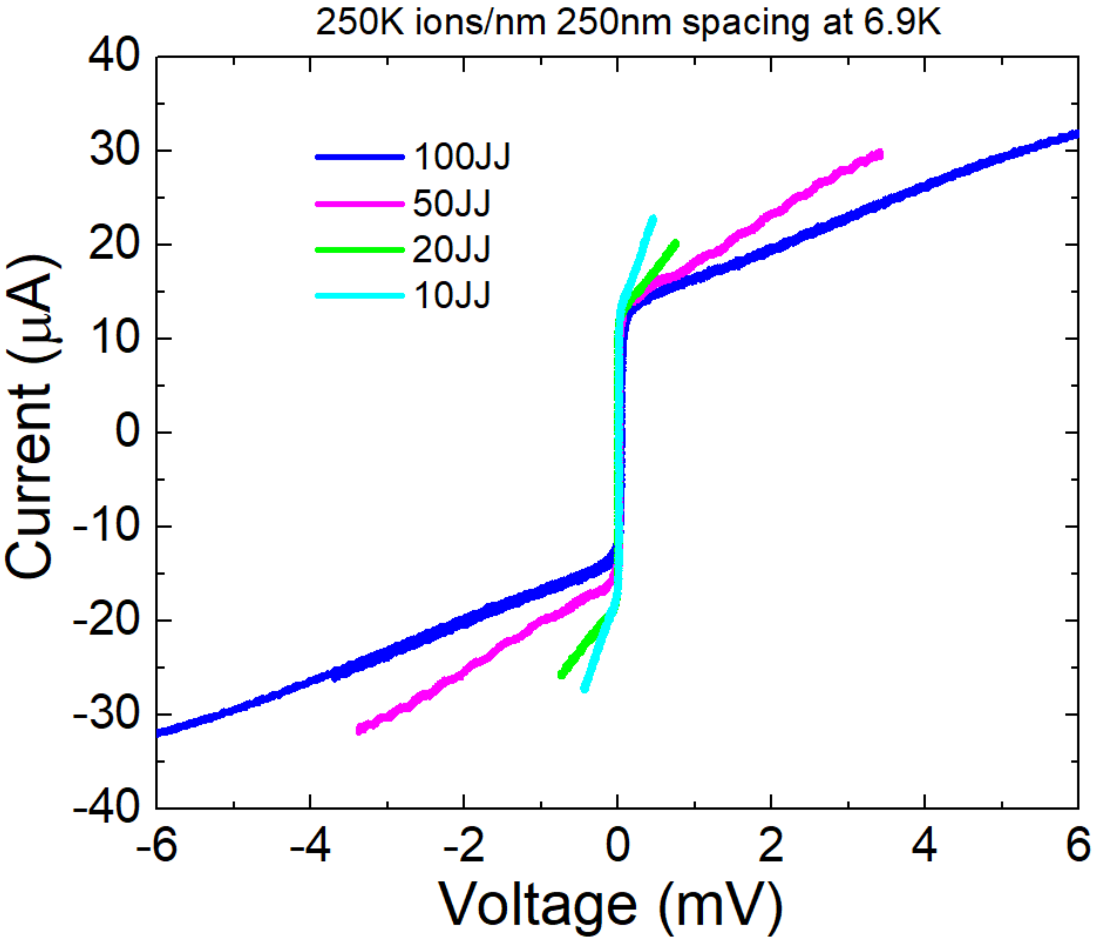

Figure 7.12: Niobium junction Array current vs voltage characterization with varied number of junctions in each array.

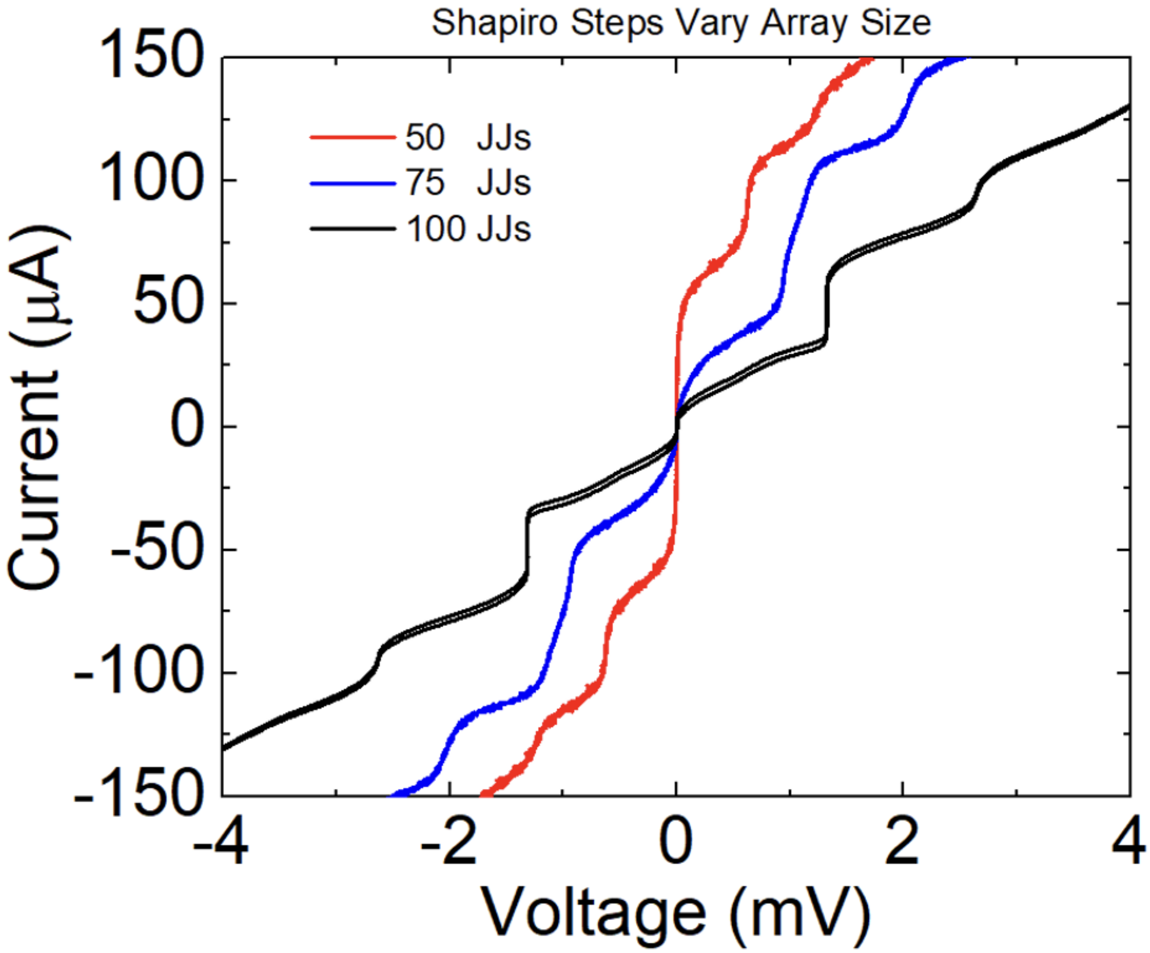

Figure 7.13: Niobium junction Array Shapiro step characterization on arrays with 50, 75 and 100 Junctions junctions.

In order to establish this method of making Niobium Josephson junction arrays as a useful approach to making josephson waveform synthesizers or an approach to a voltage standard device I needed to determine how many junctions it would take for the n=1 Shapiro step to appear at 1 volt. Using information gained in resistance and IV characterizations above I fabricated the junction arrays with a spacing of 250nm and junction dose of 250K ions/nm. Figure 7.13 show three junction arrays of length 50, 75 and 100 Josephson junctions. The 50 and 100 junction arrays are characterized under 6 Ghz while the 75 junction array was characterized with 6.12 Ghz excitation frequency. The n=1 steps occur at 0.63mV, 0.98mV and 1.32mV respectively. A usefully voltage standard or Josephson waveform synthesizer device must have giant flat Shapiro steps. The 75 junction array has a giant Shapiro step of $72\mu A$ but is tilted at half its height. This is likely due to an error in fabrication causing a change in the array spacing or junction attributes part way through helium ion radiation. However, the 100 junction array has a extremely flat Shapiro step of $43\mu A$ which can be increased by optimizing the AC power. This type of Shapiro step is comparable to the state of the art traditional Niobium heterojunction Josephson arrays used for voltage standard devices.

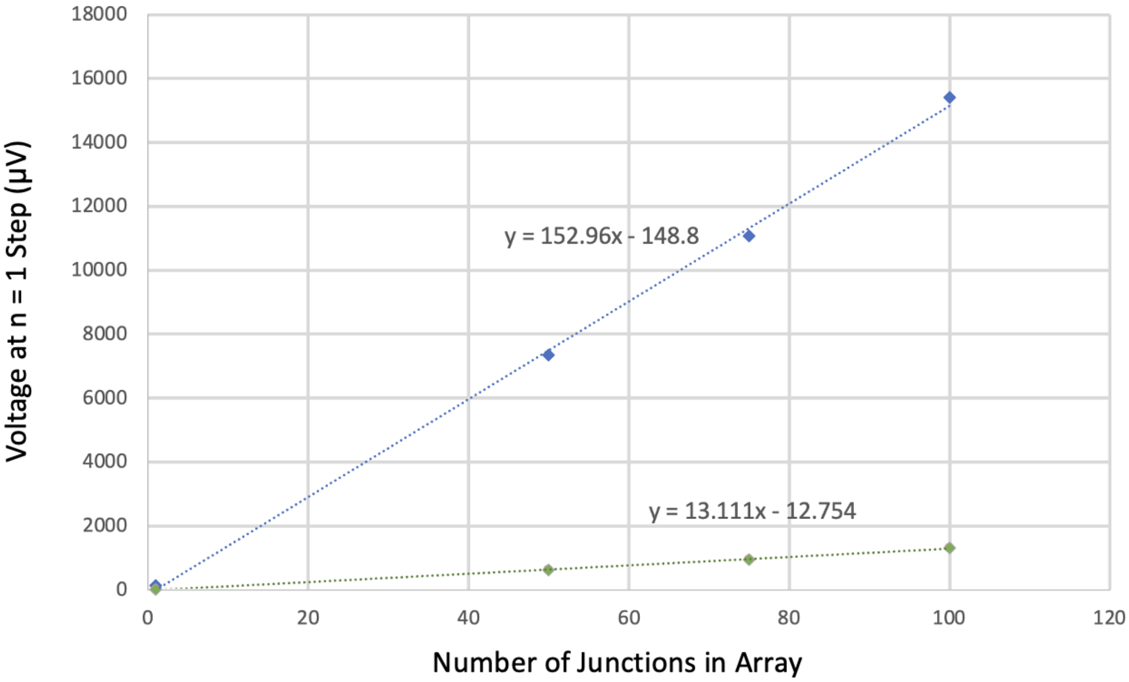

Figure 7.14: Niobium junction Array Shapiro step characterization on arrays with 50, 75 and 100 Junctions junctions. Green points are measured data. Blue points are predicted voltage positions for 70Ghz AC radiation.

I normalized the voltage for a frequency of 6Ghz and 70Ghz and graphed the number of junctions vs voltage at the n=1 step in figure 7.14. I chose to normalize the the device performance to 70Ghz as it is the most common frequency used for voltage standard systems. Figure 7.14 shows predicted n=1 step positions for 70Ghz AC radiation in blue as well as the data measured under 6Ghz radiation in green. These data are nearly linear between the points with a trend line dawn on top showing the linear effect to voltage position with added junctions.

This figure also shows the equation for the trend line accompanying each data set. Using this equations I can estimate the number of junctions needed to have an n=1 Shapiro step at 1 volt. With 70Ghz radiation I found that we would need 6538 junctions. With a spacing of 250nm this array can fit on a strip line with length as small as 1.64mm. State of the art Nibium Josephson arrays that are able to produce an n=1 step at 1 volt will have a similar number of junctions. However, the junctions on these devices are $3 - 5\mu m^2$ in area needing a surface area of several square centimeters.

7.4 FHeIB Niobium SQUID

In a natural progression of this new fabrication technique I next created a SQUID made using Helium ion beam induced disorder of Niobium film. Figure 7.14 show optical images of the design of the full chip. The right side image in figure 7.14 shows a zoomed in photo of the SQUID where faint disordered junction lines can be seen. The wires making up the SQUID are $5\mu m$ across and the cental SQUID hole is $20\mu m$ wide. The junctions on the device are written with a dose of 5M ions/nm. This is the first SQUID fabricated using this method.

Figure 7.15: Optical microscope images of Niobium SQUID design.

Figure 7.15 shows electrical characterizations of this device. The IV curve has a relatively flat region to the left and right of the critical current. This indicates the Josephson junctions have strong tunneling barriers allowing primarily Josephson tunneling evenings.

This device was characterized at 3.2 Kelvin. The critical current is $82\mu A$ and the $R_N = 1.12\Omega$. This indicates an $R_N \approx 2.25\Omega$s for each junction which is typical for this radiation dose. Typical cutting edge heterojunction Niobium SQUIDs have slightly less critical current but R_N between 10Ω and 15Ω. Though the resistance of this device is an order of magnitude less than those devices the junctions in it are much smaller. In future work we can achieve this level of resistance by creating junction arrays on either side of the SQUID loop.

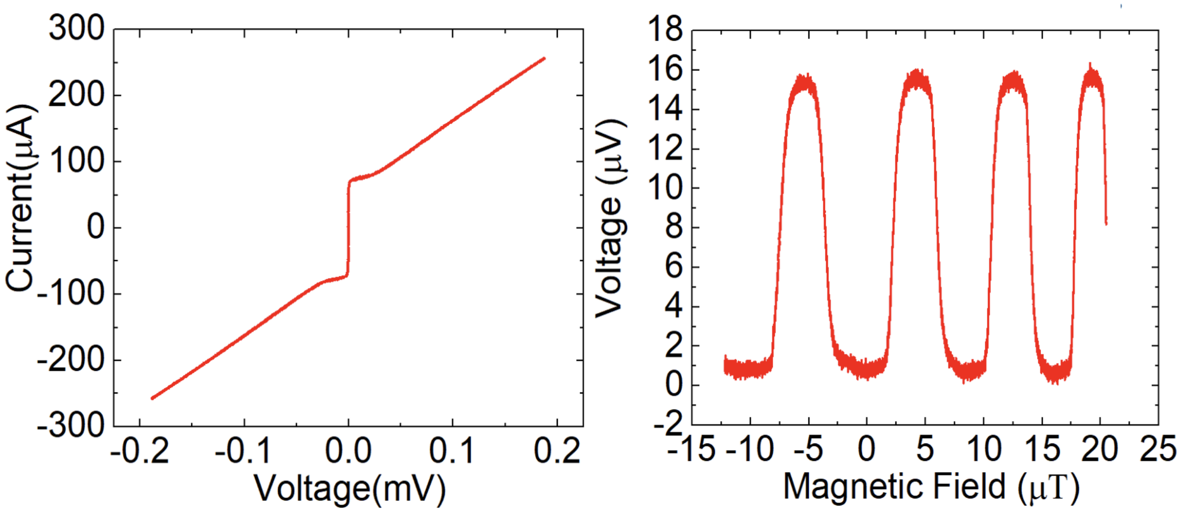

Figure 7.16: Electrical characterizations of HeIB fabricated Niobium SQUID, Left: IV curve Right: BV transfer function.

The magnetic field vs voltage characterization in figure 7.15 dipicts a transfer function with height of $16\mu V$. The maximum ΔV for this device given its I_C and R_N should be: $\Delta V = \frac{2}{3} I_C R_N = 60\mu V$. Here we see the actual ΔV is 26 percent of its maximum. I attribute this mismatch to mismatch in inductance of the squid loop and the junctions. However, at this resistances, the ratio of maximum voltage modulation to maximum theoretical voltage modulation is typical for similar devices.

There are several ways we can utilize and improve this SQUID. It can be used to investigate the kinetic inductance of the material by comparing the transfer functions of several devices with different sized pickup loops. We can improve the system by creating an array of junctions on either side of the loop, with smaller width with higher dose to increase the resistance.

Chapter 8

Conclusions

In this thesis I discussed Josephson junctions and SQUIDs fabricated with focused Helium ion beam. This relatively new approach to designing and constructing superconducting devices and circuits has enabled the creation of many novel devices that can have far reaching effects in the field of superconducting device science and technology.

The early chapters of this thesis were dedicated detailing the theory related to superconductors and superconducting devices needed to grasp this work. I also discussed in detail the effects of ion radiation on superconducting materials as well as the capabilities and constraints with using a focused helium ion microscope to directly write these circuits.

Using YBCO, I carried out many experiments to analyze the Josephson junction capabilities and attributes that I fabricated using FHeIB. These junctions were characterized in a wide rage of temperatures and in the presence of a magnetic field and Ghz frequency electro-magnetic fields. The bulk of my research related to YBCO devices comes from my efforts to make low noise SQUID magnetometers. I showed how the direct inject hexagonal SQUID design was successfully integrated and characterized as part of a commercial pulsed tube cooler magnetic materials characterization platform. I further analyzed the noise sources and designed a lower noise SQUID with similar spacial resolution. This high resistance lower noise SQUID had a field noise of only $540fT/\sqrt{Hz}$ and flux noise of $2\mu\Phi_0/\sqrt{Hz}$ at 1Khz. This work can be expanded by altering the size of the pickup loop and modifying the thickness of the wires to further lower the inductance.

In this thesis I reported a new method for making Niobium superconducting devices with focused helium ion beam radiation. I carried out a variety of experiments on the modification of niobium films with focused Helium ion beam. I demonstrated the ability to mill holes and lines using a sufficiently high dose of ion radiation. I demonstrated the differences in properties between junctions made with a wide range of ion doses. I developed and characterized the first Josephson arrays using this technology. I showed the n=1 Shapiro step for a 100 junction array existing at 1.32mV. The arrays I made demonstrate similar operating capabilities as similar Niobium devices designed for the voltage standard and Josephson waveform synthesizers but take up much lest surface area and are much faster to design and fabricate. I lastly fabricated and tested the first Niobium SQUID made with FHeIB. With broad beam higher energy Helium radiation and precision masking this method of fabrication can be sped up and allow for greater reproduce-ability of junctions and integration with existing superconducting fabrication techniques.

Bibliography

[1] H. K. Onnes, into the properties of substances at low temperatures, which have led, amongst other things, to the preparation of liquid helium," Nobel lecture, vol. 4, 1913.

[2] H. Kamerlingh Onnes, superconductivity of mercury," Comm. Phys. Lab. Univ. Leiden, vol. 122, pp. 122124, 1911.

[3] W. Meissner and R. Ochsenfeld, neuer effekt bei eintritt der supraleitfahigkeit," Naturwissenschaften, vol. 21, no. 44, pp. 787788, 1933.

[4] Kittel, C. (2004). Introduction to solid state physics (8th ed.). John Wiley Sons., 1995

[5] J. Bardeen, L. N. Cooper, and J. R. Schrieffer, of superconductivity," Phys. Rev., vol. 108, no. 5, p. 1175, 1957.

[6] Wilson, Martin N. "Superconducting magnets." (1983).

[7] B. D. Josephson, new effects in superconductive tunnelling," Phys. Lett., vol. 1, no. 7, pp. 251253, 1962.

[8] Ted Van Duzer and Charles W. Turner. Principles of superconductive devices and circuits, (second ed.). Prentice Hall PTR, USA. 1998

[9] Bednorz, J.G., Müller, K.A. Possible highT c superconductivity in the BaLaCuO system. Z. Physik B - Condensed Matter 64, 189–193 (1986)

[10] E. Y. Cho, Focused helium beam irradiated josephson junctions. University of California, San Diego, 2016.

[11] F. London and H. London, electromagnetic equations of the supraconductor," Proceedings of the Royal Society of London. Series A-Mathematical and Physical Sci- ences, vol. 149, no. 866, pp. 7188, 1935.

[12] F. London, : Macroscopic theory of superconductivity, Vol. I.," Science, vol. 113, no. 2938, pp. 447447, 1951.

[13] . L. Ginzburg and L. D. Landau, the theory of superconductivity," in On superconductivity and superfluidity, pp. 113137, Springer, 2009.

[14] M. Tinkham, Introduction to superconductivity. Courier Corporation, 2004.

[15] L. N. Cooper, electron pairs in a degenerate Fermi gas," Physical Review, vol. 104, no. 4, p. 1189, 1956.

[16] Amit Finkler, Yehonathan Segev, Yuri Myasoedov, Michael L. Rappaport, Lior Ne'eman, Denis Vasyukov, Eli Zeldov, Martin E. Huber, Jens Martin, and Amir YacobyNano Letters 2010

[17] J. Clarke and A. I. Braginski, The SQUID handbook, vol. 1. Wiley Online Library, 2004.

[18] J. Clarke and A. I. Braginski, The SQUID handbook. Vol. 2. applications of SQUIDs and SQUID systems, vol. 2. Wiley Online Library, 2006.

[19] R.M Leahy, J.C Mosher, M.E Spencer, M.X Huang, and J.D Lewine. A study of dipole localization accuracy for MEG and EEG using a human skull phantom. Electroencephalography and Clinical Neurophysiology, 107(2):159173, 1998.

[20] D Cohen. Magnetoencephalography: evidence of magnetic elds produced by alpharhythm currents. Science (New York, N.Y.), 161(3843):7846, 8 1968.

[21] Kirsten Tolstrup, Bo E. Madsen, Jose A. Ruiz, Stephen D. Greenwood, Judeen Camacho, Robert J. Siegel, H. Caroline Gertzen, Jai-Wun Park, and Peter A. Smars. Non-Invasive Resting Magnetocardiographic Imaging for the Rapid Detection of Ischemia in Subjects Presenting with Chest Pain. Cardiology, 106(4):270276, 11 2006.

[22] N. Oukhanski, R. Stolz, V. Zakosarenko, and H.-G. Meyer. Low-drift broadband directly coupled dc SQUID read-out electronics. Physica C: Superconductivity, 368(1):166170, 2002.

[23] V. K. Kornev, I. I. Soloviev, A. V. Sharaev, N. V. Klenov, and O. A. Mukhanov. Active Electrically Small Antenna Based on Superconducting Quantum Array. IEEE Transactions on Applied Superconductivity, 23(3):18004051800405, 6 2013.

[24] S. Shokhor, B. Nadgorny, M. Gurvitch, V. Semenov, Yu. Polyakov, K. Likharev, S. Y. Hou, and Julia M. Phillips. All-high-Tc superconductor rapid-single- uxquantum circuit operating at 30 K. Applied Physics Letters, 67(19):2869, 11 1995.

[25] PAUL BUNYK, KONSTANTIN LIKHAREV, and DMITRY ZINOVIEV. RSFQ TECHNOLOGY: PHYSICS AND DEVICES. International Journal of High Speed Electronics and Systems, 11(01):257305, 3 2001.

[26] S. P. Benz and C. A. Hamilton. A pulse-driven programmable Josephson voltage standard. Applied Physics Letters, 68(22):3171, 1996.

[27] P. W. Anderson and J. M. Rowell. Probable Observation of the Josephson Superconducting Tunneling Eect. Physical Review Letters, 10(6):230232, 3 1963.

[28] Kjærgaard, M., Schwartz, M. L., Braumüller, J., Krantz, P., Wang, J. I., Gustavsson, S., & Oliver, W. (2020). Superconducting Qubits: current state of play. *Annual Review of Condensed Matter Physics*, *11*(1), 2020

[29] *Rosenthal, P. A., Beasley, M. R., Char, K., Colclough, M. S. & Zaharchuk, G.*

[30] The NIST Reference on Constants, Units, and Uncertainty. NIST. 20 May 2019. Retrieved 2019-05-20.

Flux focusing effects in planar thin-film grain-boundary Josephson junctions.

Appl. Phys. Lett. 59, 3482–3484 (1991).

[31] The Feynman lectures on physics. Reading, Mass. :Addison-Wesley Pub. Co., 1988

[32] S. Shapiro, Phys. Rev. Lett. 11, 80 (1963).

[33] V. Ambegaokar and B. I. Halperin, Phys. Rev. Lett. 22, 1964 .

[34] V.L. Ginzburg and L.D. Landau, Zh. Eksp. Teor. Fiz. 20, 1064 (1950).

[35] Finnegan, T. F.; Denenstein, A.; Langenberg, D. N. (1 August 1971). "ac-Josephson-Effect Determination of A Standard of Electrochemical Potential Based on Macroscopic Quantum Phase Coherence in Superconductors" 1971

[36] Fagaly, R. L. (2006). Superconducting quantum interference device instruments and applications. Review of Scientific Instruments, 77(10). 2006

[37] R. C. Jaklevic, J. Lambe, A. H. Silver, and J. E. Mercereau, Phys. Rev. Lett. 7, 159 (1964).

[38] Cho, E.Y. et al. YBA2CU3O7 superconducting quantum interference devices with metallic to insulating barriers written with a focused helium ion beam, AIP 2015

[39] Randy W. Simon, Michael J. Burns, Mark S. Colclough, Greg Zaharchuk, and Robin Cantor, mr squid, 1996

[40] C H Wu et al, Supercond. Sci. Technol. 19 S246, 2006

[41] Grekhov, I (1999). "Growth mode study of ultrathin HTSC YBCO films on YBaCuNbO buffer". Physica C: Superconductivity. 1999

[42] Housecroft, C. E.; Sharpe, A. G. (2004). Inorganic Chemistry (2nd ed.). Prentice Hall

[43] Pattini, Francesco. (2009). Growth of oxide thin films for energy devices by Pulsed Electron Deposition.

[44] Molodyk, A.; et al. (2021). "Development and large volume production of extremely high current density YBa2Cu3O7 superconducting wires for fusion". Scientific Reports. 11 (1) 2021

[45] Kim, C. J., Hong, G. W. (1999). Defect formation, distribution and size reduction of in melt-processed YBCO superconductors. Superconductor Science and Technology, 1999

[46] A.M. Cucolo et al. (2002) Planar Tunnel junctions on 90 K and 60 K YBCO single crystals: Superconducting and normal state properties, Physica C: Superconductivity. 2002

[47] T. Pereg-Barnea, P. J. Turner, R. Harris, G. K. Mullins, J. S. Bobowski, M. Raudsepp, Ruixing Liang, D. A. Bonn, and W. N. Hardy Phys. Rev. B 69, 184513 – Published 28 May 2004

[48] S. Kamal, Ruixing Liang, A. Hosseini, D. A. Bonn, and W. N. Hardy Phys. Rev. B 58, R8933(R) – Published 1 October 1998

[49] H. LONDON and G. R. CLARKE Rev. Mod. Phys. 36, 320 – Published 1 January 1964

[50] D. K. Finnemore, T. F. Stromberg, and C. A. Swenson Phys. Rev. 149, 231 – Published 9 September 1966

[51] I.I. Soloviev, S.V. Bakurskiy, V.I. Ruzhickiy, N.V. Klenov, M.Yu. Kupriyanov, A.A. Golubov, O.V. Skryabina, and V.S. Stolyarov Phys. Rev. Applied 16, 044060 – Published 29 October 2021

[52] Gregor Hlawacek, Vasilisa Veligura, Raoul van Gastel, Bene Poelsema; Helium ion microscopy. J. Vac. Sci. Technol. B 1 March 2014

[53] S. A. Cybart, Planar Josephson junctions and arrays by electron beam lithography and ion damage. University of California, San Diego, 2005.

[54] E. Y. Cho, Focused helium beam irradiated josephson junctions. University of California, San Diego, 2016.

[55] Koblischka, M. R., amp; Hartmann, U. (2003). Recent advances in magnetic force microscopy. Ultramicroscopy, 97(1-4), 103–112. https://doi.org/10.1016/s0304-3991(03)00034-2

[56] Mukasa K, Sueoka K, Hasegawa H, Tazuke Y and Hayakawa K 1995 Spin-polarized STM and its family Mater. Sci. Eng. B

[57] Claudia D. Tesche and John Clarke, dc SQUID: Noise and Optimization, Journal of Low Temperature Physics, Vol. 29, Nos. 3/4, 1977

[58] Hiroyuki Fujishiro et al, Anisotropic Thermal Diffusivity and Conduc- tivity of YBCO(123) and YBCO(211) Mixed Crystals, 1994 Jpn. J. Appl. Phys. 33 4965

[59] H Li, H Cai, EY Cho, SJ McCoy, YT Wang, JC LeFebvre, YW Zhou, High-transition-temperature nanoscale superconducting quantum interference devices directly written with a focused helium ion beam, Applied Physics Letters 116 (7), 070601

[60] SQUIDs in with applications, IBM T. J. Watson Research Center, P.O. Box 218, Yorktown Heights, NY 10598, U.S.A.

[61] M. Mata, Y. Murayama, S. Kiryu, N. Kasai, S. Kashiwaya, M. Koyanagi, T. Endo and S. Kuriki, Sputtered YBCO bicrystal dc-SQUIDS, IEEE Trans. Magn. 27, 3043 (1991)

[62] EY Cho, H Li, JC LeFebvre, YW Zhou, RC Dynes, SA Cybart, Direct-coupled micromagnetometer with Y-Ba-Cu-O nano-slit SQUID fabricated with a focused helium ion beam, Applied physics letters 113 (16), 162602